Near and Far Field Models of External Fluid Mechanics of Ocean Thermal Energy Conversion (OTEC) Power Plants

by

Mariana Rodríguez Buño

Ingeniera Civil
Universidad de la República, Uruguay, 2007

Submitted to the Department of Civil and Environmental Engineering, in partial fulfillment of the requirements for the degree of

Master of Science in Civil and Environmental Engineering

at the

MASSACHUSETTS INSTITUTE OF TECHNOLOGY

February 2013

Signature of Author...
Department of Civil and Environmental Engineering
January 18, 2013

Certified by...
E. Eric Adams
Lecturer and Senior Research Engineer of Civil and Environmental Engineering
Thesis Supervisor

Accepted by..
Heidi M. Nepf
Chair, Departmental Committee for Graduate Students

Near and Far Field Models of External Fluid Mechanics of Ocean Thermal Energy Conversion (OTEC) Power Plants

by

Mariana Rodríguez Buño

Submitted to the Department of Civil and Environmental Engineering on January 18, 2013,
in partial fulfillment of the requirements for the degree of
Master of Science in Civil and Environmental Engineering

Abstract

The world is facing the challenge of finding new renewable sources of energy – first, in response to fossil fuel reserve depletion, and second, to reduce greenhouse gas emissions. Ocean Thermal Energy Conversion (OTEC) can provide renewable energy by making use of the temperature difference between the surface ocean and deep ocean water in a Rankine cycle. An OTEC plant pumps huge volumes of water from the surface and nearly 1 km depth, and releases it at an intermediate depth. The effects of this enormous flux are crucial to understand since disruption of the ambient temperature stratification can affect the efficiency of the plant itself and of adjacent plants.

This thesis aims to study the external fluid mechanics of offshore OTEC power plants, to assess their environmental impact and to help analyze whether OTEC plants can provide a sustainable source of energy. Although there has been interest in OTEC for several decades, so far primarily physical and analytical models have been developed. In this study numerical models are developed to model OTEC operating plants: integral models for the near and intermediate field and a large-scale ocean general circulation model. Two strategies in modeling OTEC plant discharge are used to analyze plume dynamics: the "Brute Force" approach, in which a circulation model, MITgcm, computes the near, intermediate and far field mixing; and the "Distributed Sources and Sinks" approach, in which the near and intermediate field are represented in the circulation model by sources and sinks of mass computed by integral models.

This study concludes that the Brute Force modeling strategy is highly computationally demanding and sometimes inaccurate. Such simulations are very sensitive to model resolution and may require the use of unrealistic model parameters. The Distributed Sources and Sinks approach was found to be capable of modeling the plume dynamics accurately. This method can be applied to the study of adjacent OTEC power plant interaction, redistribution of nutrients, and propagation of contaminants.

Thesis Supervisor: E. Eric Adams
Title: Lecturer and Senior Research Engineer of Civil and Environmental Engineering

Acknowledgements

This thesis has been accomplished with the support of many people. I would like to express my deepest thanks to all of them.

First and foremost, I am profoundly grateful to my advisor, Dr. E. Eric Adams, for his guidance, support, and encouragement during this process. I am really thankful for his patience, availability, valuable comments and suggestions, and for the interesting discussions on his office blackboard. I would also like to thank my advisor's wife, Pat, for hosting delicious dinners for the research group as well as for hosting fun holiday parties.

I additionally thank Dr. Jason Goodman for his valuable help in the early stages of this research, especially in implementing an OTEC plant into an existing model.

I am deeply grateful too to Dr. Jean-Michel Campin from EAPS department at MIT, for his help and advice in making all the Fortran code modifications I needed and wanted to try for this research.

I want to thank my fellow graduate students at Parsons Laboratory and my research group, Natasha, Ruo and Godine, for being so friendly and helpful. I also thank my very good friends Juan, Greg, Jorge C., María, Bruno, Aura, Francisco, Leon, Jorge E., Andrés, and Ignacio, for the amazing times we shared and for always being there when I needed it.

Support for this thesis was provided, in part, by a grant from Fulbright Commission and in part by a grant from BP/The Gulf of Mexico Research Initiative. I give a sincere thank you to the Civil and Environmental Engineering professors and administrative assistants for their outstanding dedication and support for students.

Lastly, I would like to thank all my family, especially my parents, Graciela and Ricardo, and my brothers, Ramiro and Ricardo, for their unconditional support, love, and encouragement while being away from home. None of this would have been possible without them.

Contents

Chapter 1 - Introduction 16
1.1 Ocean Thermal Energy Conversion Principles of Operation 16
1.2 Thermodynamic Efficiency 18
1.3 Ocean Thermal Energy Resource Available 19
1.4 OTEC History of Development 22
1.5 Prospect for OTEC 24
1.6 Previous Work on OTEC Modeling 25
1.7 Research Objectives 27
1.8 Thesis Outline 28

Chapter 2 - OTEC External Flows 29
2.1 General Characteristics 29
2.2 Warm Water Intake 31
2.3 Cold Water Intake 31
2.4 Discharge 31
2.5 Flow Rates 32
2.6 Ambient Temperature Profile 33
2.7 Exhaust Temperatures 34

Chapter 3 - Modeling Tools 36
3.1 Plume Dynamics Scales 36
3.2 Ambient Stratification 37
3.3 Near Field Model 38
  3.3.1 Ambient Currents 40
  3.3.2 Integral Quantities 41
  3.3.3 Conservation Equations 42
  3.3.4 Turbulent Closure 44
  3.3.5 Solution Method 45
  3.3.6 Zone of Flow Establishment 45

3.3.7 Turbulent Fluctuations Terms 46
3.3.8 Earth Rotation 46
3.3.9 End of Near Field 47
3.3.10 Results 47
3.3.11 Effect of a Coflow Current on Near Field Mixing 48
3.3.12 Effect of a Crossflow Current on Near Field Mixing 50
3.4 Intermediate Field 53
3.4.1 Integral Magnitudes 54
3.4.2 Conservation Equations 55
3.4.3 Buoyant Spreading 56
3.4.4 Solution Method 58
3.4.5 End of Intermediate Field 59
3.4.6 Results 59
3.5 Far Field Model 62
3.5.1 Governing Equations 62
3.5.2 Turbulence Model 64
3.5.3 Spatial Discretization 65
3.5.4 Boundary Conditions 66
3.5.5 Numerical Stability Criteria 66

Chapter 4 - Strategy of Coupling the Models 68
4.1 "Brute Force" Approach 68
4.1.1 Setup 69
4.1.2 Plume Trapping 71
4.1.3 Computational Domain and Model Resolution 73
4.1.4 Numerical Trap Depth 74
4.1.5 Effect of Eddy Viscosity on Trap Depth 75
4.1.6 Effect of Resolution and Eddy Viscosity on Plume Shape 77
4.1.7 Effect of Eddy Diffusion on Plume Trap Depth and Plume Shape 77
4.1.8 Conclusions 78
4.1.9 Application to Real OTEC Scenarios 82

4.1.10 Momentum Implementation in MITgcm Source Code 86
4.1.11 Sensitivity of Trap Depth to Initial Buoyancy.. 86
4.1.12 Temperature of the Source as Function of the Initial Buoyancy................ 87
4.1.13 Full Scale OTEC Simulations... 89
4.2 Distributed Sources and Sinks Approach.. 100
4.2.1 Application to a Single OTEC Plant.. 101
4.2.2 Application to Group of OTEC Power Plants 105

Chapter 5 - Environmental Impact.. 115
5.1 Artificial Nutrient Upwelling... 115
5.2 Upwelling Velocity 118

Chapter 6 - Summary and Conclusions.. 123

References 126

List of Figures

Figure 1.1 - OTEC closed-cycle 17

Figure 1.2 - OTEC open-cycle 17

Figure 1.3 - OTEC hybrid cycle 18

Figure 1.4 - OTEC temperature ladder 19

Figure 1.5 - Vertical temperature distribution of seawater 20

Figure 1.6 - Annual temperature (˚C) at the surface 21

Figure 1.7 - Mean annual temperature difference in ˚C between water depths of 20 m and 1000 m 21

Figure 1.8 - Cold water pipe used in Cuba by Dr. Claude 23

Figure 1.9 - Installation of the cold water pipe in Cuba 23

Figure 1.10 - Ship on which OTEC plant was installed in Brazil 24

Figure 1.11 - A land based OTEC facility at the Keahole Point on the Kona coast of Hawaii 24

Figure 1.12 - World energy consumption by fuel, 1990-2035 in quadrillion BTU 25

Figure 2.1 - Scheme of an OTEC intake flows and discharge plume, causing deformation of the ocean thermal structure 29

Figure 2.2 - OTEC combined discharge general scheme, indicating typical intake temperatures and typical effluent temperature for a 100-MW power plant 30

Figure 2.3 - Different OTEC discharge schemes 32

Figure 2.4 - Typical ocean ambient temperature profile 34

Figure 3.1 - Scheme of OTEC discharge, identifying near, intermediate and far fields 36

Figure 3.2 - Plume centerline trajectory and ambient density minus plume centerline density for a 100-MW OTEC combined exhaust plant in a typical stratified ambient 38

Figure 3.3 - Gaussian profiles of velocity and excess density for a buoyant jet 39

Figure 3.4 - Three-dimensional buoyant jet discharged into ambient flow with global and local coordinate system 40

Figure 3.5 - Jet showing Zone of Flow Establishment and Zone of Established Flow 46

Figure 3.6 - Near field plume characteristics for a 100-MW OTEC plant with combined discharge 48

Figure 3.7 - Effect of coflow current on mixing and plume characteristics at the end of the near field 49

Figure 3.8 - Top view of the centerline plume trajectory for different incidence angles between the background current and the discharge momentum 50

Figure 3.9 - Vertical view of the centerline trajectory for different incidence angles between the background current and the discharge momentum 51

Figure 3.10 - Vertical view of the centerline trajectory for different incidence angles between the background current and the discharge momentum 51

Figure 3.11 - Effect of crossflow angle on the volumetric dilution 52

Figure 3.12 - Effect of crossflow angle on the terminal trapping level 52

Figure 3.13 - Plume collapse effect in the transition from near field to intermediate field 53

Figure 3.14 - Collapsed plume cross-section 54

Figure 3.15 - Intermediate field plume characteristics for a 100-MW OTEC plant with combined discharge 60

Figure 3.16 - Collapsed plume cross-section 61

Figure 3.17 - Top and vertical view of the plume collapse into a layer 61

Figure 3.18 - Applications of MITgcm on different scales 62

Figure 3.19 - Arakawa C-grid 65

Figure 3.20 - Variable grid size mesh used in OTEC simulations... 65

Figure 4.1 - Modeled domain showing the thermal stratification of the fluid and the source location 69

Figure 4.2 - Numerical modeled plume defined by a surface of tracer concentration 0.01.......... 70

Figure 4.3 - Plume trap depth (h_t) definition 72

Figure 4.4 - Vertical view of the plume boundary from which the trap depth can be computed 74

Figure 4.5 - Effect of eddy viscosity on plume trap depth for different model resolutions.......... 75

Figure 4.6 - Effect of eddy diffusion on trap depth, for Q=20 m^3/s, grid size 6 m, and eddy viscosity 10^{-2} m^2/s 78

Figure 4.7 - Plumes for different grid sizes and eddy viscosities (A_h and A_z are the horizontal and vertical eddy viscosity coefficients respectively), for Q=20 m^3/s 80

Figure 4.8 - Plumes for different grid sizes and eddy viscosities (A_h and A_z are the horizontal and vertical eddy viscosity coefficients respectively), for Q=200 m^3/s 81

Figure 4.9 - OTEC plant representation into MITgcm for the combined exhaust discharge 83

Figure 4.10 - Comparison of trap depth computed by the integral model and MITgcm for different OTEC plant sizes (θ is the angle measured from the horizontal) 84

Figure 4.11 - Trap depth (h_t) as a function of the temperature difference between the ambient and effluent (ΔT) 88

Figure 4.12 - Temperature at the source (T) as a function of the initial temperature difference between the ambient and the efluent (ΔT) 88

Figure 4.13 - OTEC effluent plume at three different times (combined exhaust, no rotating earth) 90

Figure 4.14 - OTEC effluent plume at three different times (separated exhaust, no rotating earth).. 92

Figure 4.15 - OTEC effluent plume at three different times (combined exhaust, rotating earth) 94

Figure 4.16 - OTEC effluent plume at three different times (separate exhaust, rotating earth)... 96

Figure 4.17 - OTEC effluent plume at two different times (separate exhaust, geostrophic currents of 0.1 m/s) 98

Figure 4.18 - OTEC effluent plume at two different times (combined exhaust, geostrophic currents of 0.1 m/s) 99

Figure 4.19 - Sources and sinks method schematization 100

Figure 4.20 - Sources and sinks distribution in the mesh grid of the far field model 102

Figure 4.21 - Horizontal slice of the flow at the source level 37 days into OTEC operation 103

Figure 4.22 - Vertical slice of the flow across the distributed sources and sinks 37 days into OTEC operation 103

Figure 4.23 - Horizontal slice of the flow at a sink level 104

Figure 4.24 - OTEC group of plants 105

Figure 4.25 - Top view of OTEC group of plants 106

Figure 4.26 - Sources and sinks distribution in the mesh grid of the far field model for a group of OTEC plants 106

Figure 4.27 - Natural vertical distribution of nutrients 107

Figure 4.28 - OTEC effluent plumes 109

Figure 4.29 - Tracer concentration field (S) shown at four different depths 110

Figure 4.30 - Nutrient concentration at 105 m below the water surface (equilibrium depth of Plume 3) shown at three times 111

Figure 4.31 - Nutrient concentration at 115 m below the water surface (equilibrium depth of Plume 4) shown at three times 112

Figure 4.32 - Nutrient concentration at 125 m below the water surface (equilibrium depth of Plume 2) shown at three times 113

Figure 4.33 - Nutrient concentration at 135 m below the water surface (equilibrium depth of Plume 1) shown at three different times 114

Figure 5.1 - OTEC artificial upwelling effect 116

Figure 5.2 - Nutrient concentration (nitrates and nitrites) 6.6 hours into OTEC operation 116

Figure 5.3 - Nutrient redistribution due to artificial upwelling 117

Figure 5.4 - Schematization of OTEC pumping effect for combined discharge 119

Figure 5.5 - OTEC upwelling effect for a 100-MW plant with combined discharge 119

Figure 5.6 - Schematization of OTEC pumping effect for separate discharge 121

Figure 5.7 - OTEC upwelling effect for a 100-MW plant with separate discharges 122

List of Tables

Table 2.1 - Typical OTEC flow rates 33

Table 2.2 - Typical temperature differences between OTEC exhausts and ocean water 35

Table 4.1 - Trap depth (h_t) and dilution (S_m) for the tested cases 72

Table 4.2 - Computational domain dimensions 74

Table 4.3 - Source lengths used 74

Table 4.4 - Length scales comparison for different OTEC fluxes 85

Table 4.5 - Dilutions 107

Table 4.6 - OTEC discharge characteristics for each plant of the group 108

Chapter 1 - Introduction

1.1 Ocean Thermal Energy Conversion Principles of Operation

In tropical oceans, surface water temperature reaches about 28 ºC and deep-water temperature is about 4.4 ºC, yielding an important thermal gradient of about 23 ºC. Ocean Thermal Energy Conversion (OTEC) is an energy conversion technology that uses this thermal gradient to produce energy, by a closed Rankine cycle in a heat engine to produce mechanical work that generates electricity.

Two OTEC power cycles are illustrated in Figures 1.1 and 1.2. Systems can be either closed-cycle or open-cycle. In the closed-cycle engine (Figure 1.1) warm surface water is drawn into an evaporator where its heat vaporizes a pressurized refrigerant such as ammonia. That gas in turn spins a turbine, producing electrical power. Heat is removed from the low-pressure vapor by pumping cold water through a condenser. The re-liquefied ammonia is pressurized by a feed pump and returned to the evaporator. The cycle can then repeat. Refrigerants such as ammonia or R-134a are used in closed-cycle engines because of the low temperatures involved. Open-cycle engines (Figure 1.2) use vapor from the seawater itself as the working fluid. A significant advantage of the open-cycle process is that the condensate can serve as a freshwater source much less expensively than using reverse osmosis.

Figure 1.3 illustrates a hybrid OTEC cycle. A hybrid cycle involves elements of both closed and open cycle systems. Warm seawater is flash-evaporated; this is an *open cycle* process. That seawater, now in gaseous form, vaporizes the working fluid of a *closed loop*, ammonia. In turn, the vaporized ammonia drives a turbine, generating electricity. The gas then condenses in the heat exchanger, producing desalinated water.

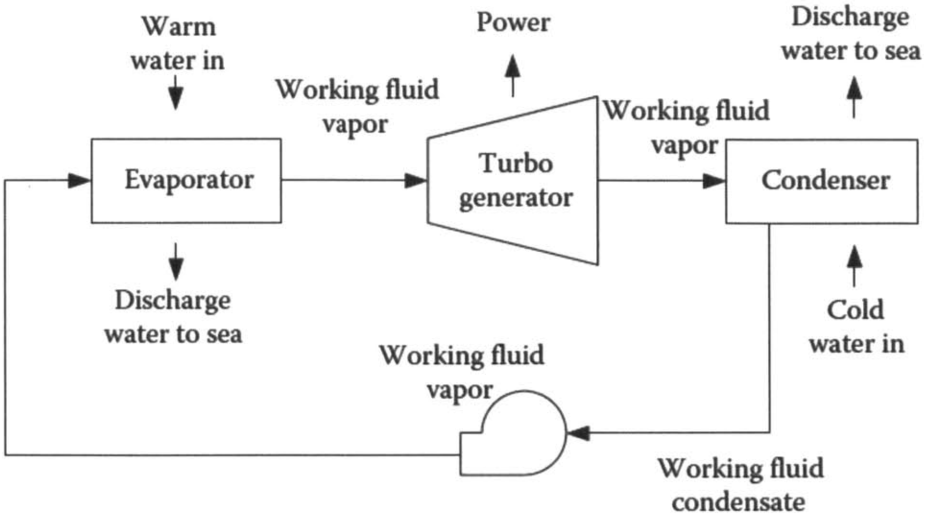

Figure 1.1 - OTEC closed-cycle (Khaligh et al., 2010).

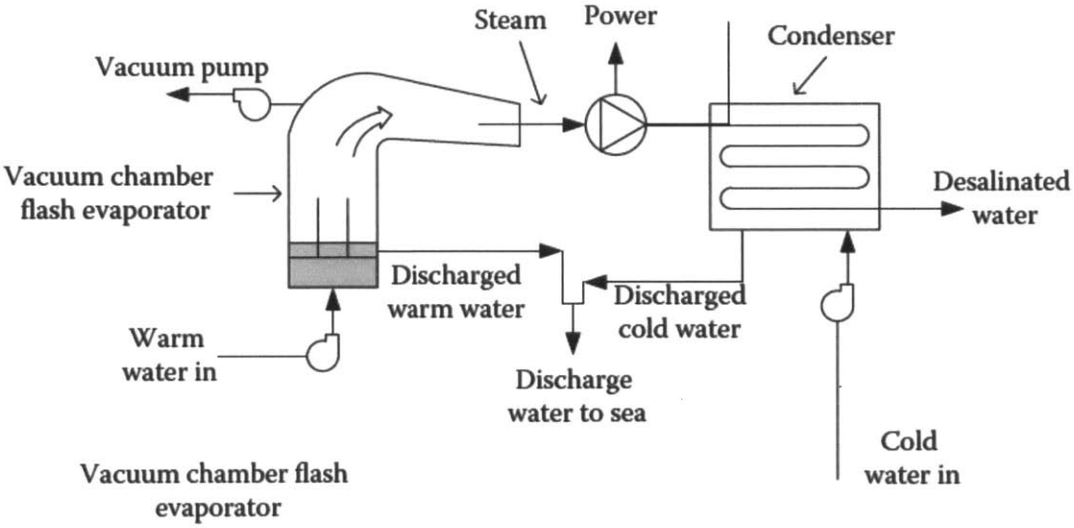

Figure 1.2 - OTEC open-cycle (Khaligh et al., 2010).

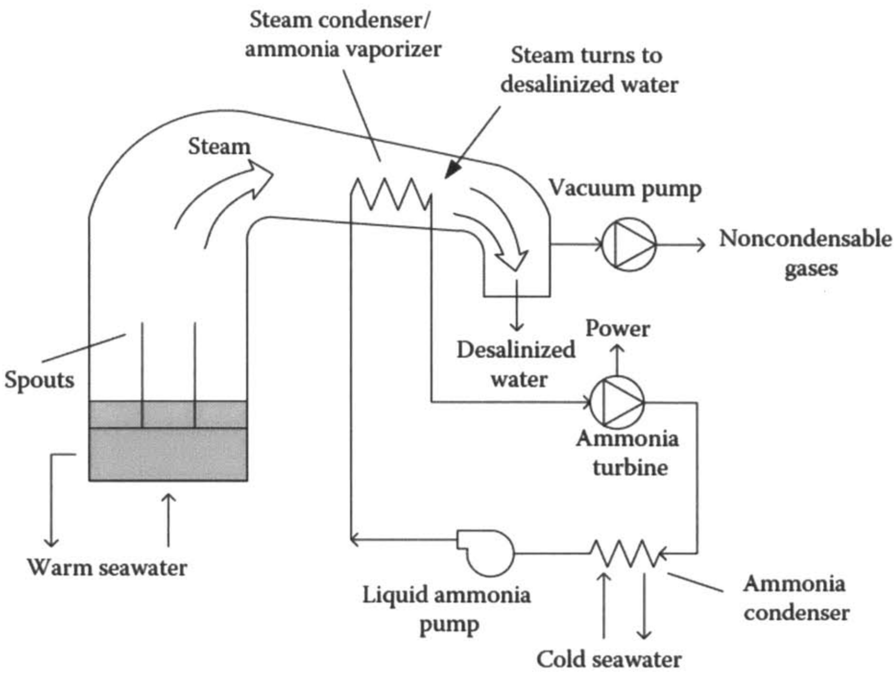

Figure 1.3 - OTEC hybrid cycle (Khaligh et al., 2010).

1.2 Thermodynamic Efficiency

The ideal thermodynamic efficiency of a heat engine operating between a warm water temperature T_w and a cold water temperature T_c is (Carnot efficiency):

$$\eta_{max} = 1 - \frac{T_c}{T_w}$$

where temperature is in degrees Kelvin. The maximum thermal efficiency of an OTEC plant is 7.5 to 8% based on typical temperatures of the surface water and water at 1 km depth for the most favorable locations (Avery and Wu, 1994). However, the real efficiency of a plant is smaller than this theoretical value due in part to the warming of the cold water and the loss of heat of the warm water. Furthermore, the heat exchangers' (evaporator and condenser) efficiency reduces the overall plant efficiency. Figure 1.4 illustrates the OTEC temperature ladder. As a reference, a 20°C seawater temperature difference corresponds to an effective temperature difference across the heat engine of about 10°C (Nihous, 2007). Consequently, the net thermodynamic efficiency of OTEC processes is of the order of 3% (Avery and Wu, 1994). This efficiency is significantly smaller than the 32%-36% for a conventional thermal plant (Vega 1992). In order to exploit the low-grade energy resource, enormous seawater flow rates are required to produce amounts of electricity comparable to conventional power plants.

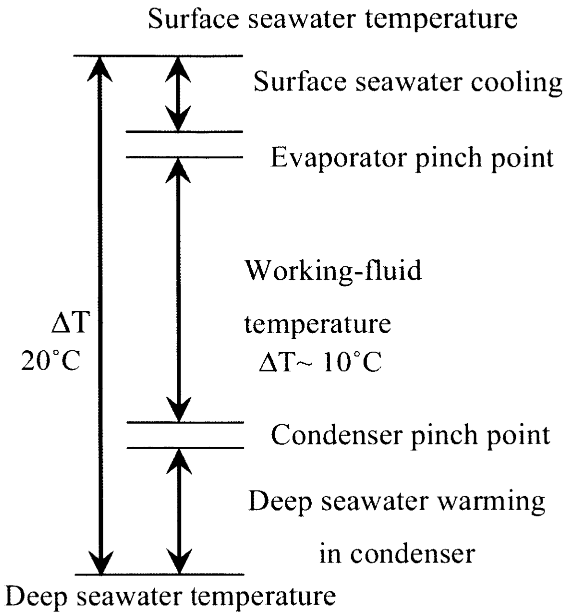

Figure 1.4 - OTEC temperature ladder (adapted from G. Nihous 2007).

1.3 Ocean Thermal Energy Resource Available

A shallow mixed layer at the surface of the ocean (uniform temperature and salinity field), 35 to 100 m thick, absorbs and retains all the energy the ocean receives from the sun. In the tropical oceans (15° north to 15° south latitude) the mixed layer reaches almost 28°C. This temperature remains virtually unchanged day and night, month after month, with the annual average temperature in the mixed layer ranging from an estimated 27 to 29°C across the region.

The temperature beneath the mixed layer, within the thermocline, drops to values of 4.4°C at depths of 800 to 1000 m. Closer to the bottom of the ocean (average ocean depth 2 km), the temperature slightly decreases. This cold water – melted from the Polar Regions – flows along the ocean bottom towards the equator and displaces the lower-density water above.

The stable higher density in the thermocline inhibits the vertical transfer of heat and momentum. Figure 1.5 shows the typical vertical temperature distribution of the ocean for five different locations, a structure that is found across all tropical areas. The temperature difference between the surface and water at a depth of 1 km remains stable throughout the year, except for extremely slight variations due to the seasons and day-to-night changes (Avery and Wu, 1994).

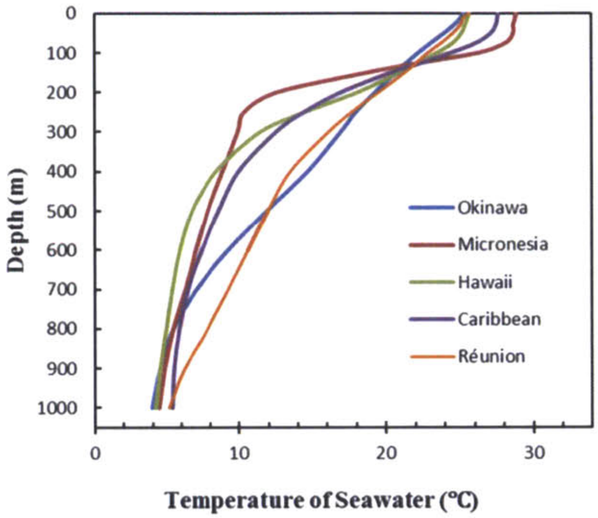

Figure 1.5 - Vertical temperature distribution of seawater (GEC Co., http://www.otec.ws/otec_principle.html).

Figure 1.6 shows the sea surface annual temperature, and Figure 1.7 shows the temperature difference between the sea surface and 1000 m in depth. Favorable locations of OTEC plants, where the temperature difference exceeds 22°C, occupy approximately 60 million km^2 (Avery and Wu, 1994).

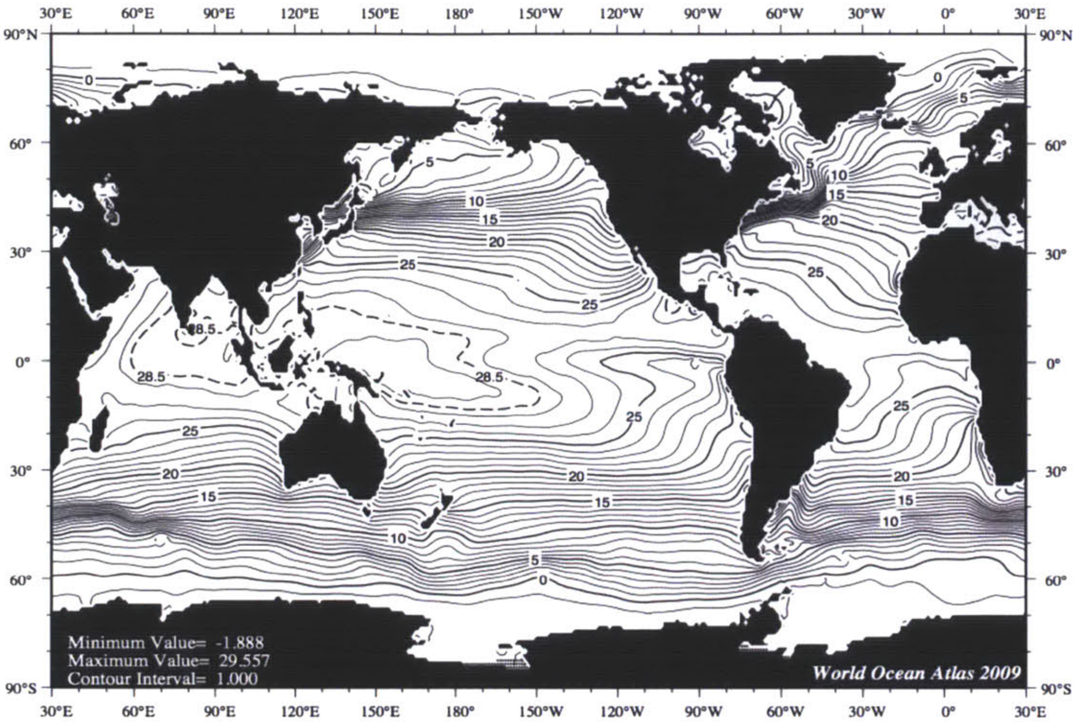

Figure 1.6 - Annual temperature (°C) at the surface (NOAA, World Ocean Atlas 2009).

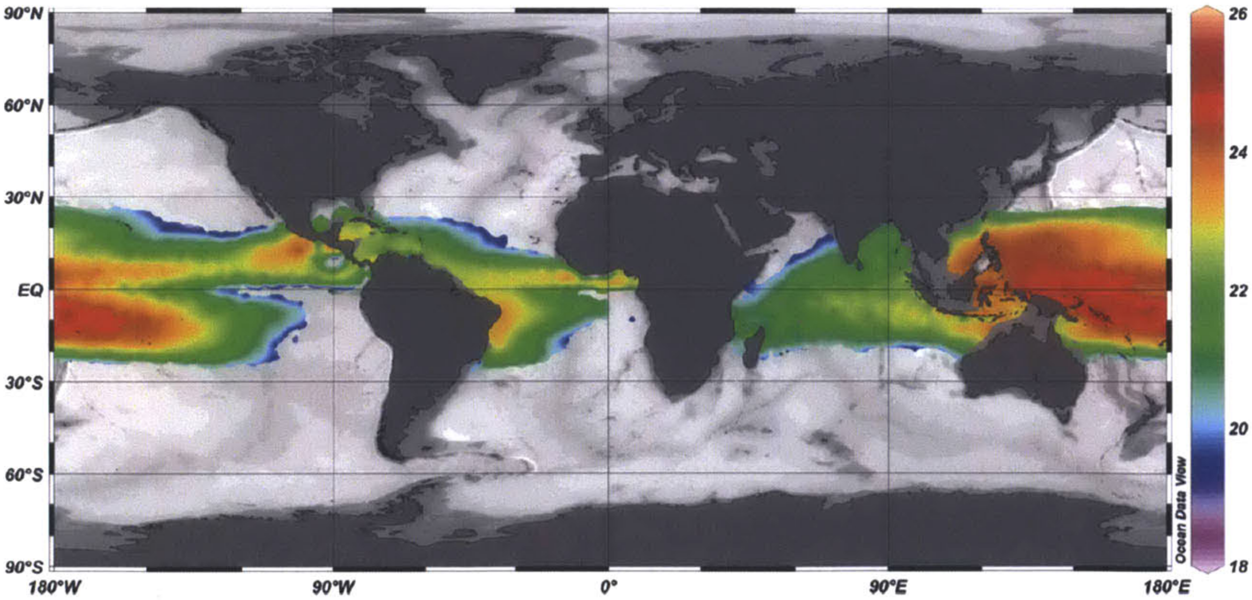

Figure 1.7 - Mean annual temperature difference in °C between water depths of 20 m and 1000 m (Rajagopalan and Nihous 2013, World Ocean Atlas 2005 database).

1.4 OTEC History of Development

The first proposal to harness energy from temperature differences in the ocean was made in 1881 by French physicist Jacques D'Arsonval. Fifty years later, his student George Claude implemented this plan and built the first-ever OTEC plant, in Matanzas Bay, Cuba. Figure 1.8 and 1.9 show pictures of the first OTEC installation. In addition, in 1935 he built another open cycle OTEC plant on the coast of Brazil, shown in Figure 1.10. Although his first plant managed to output 22 KW of electricity, neither plant could produce a net gain in electricity. The plants also failed to survive bad weather conditions. In the following years, OTEC development was slowed by competition with inexpensive hydroelectric power production (US Department of Energy, 1989).

Renewed interest in OTEC plants developed in the 1970s amidst the era's energy shortage (US Department of Energy, 1989). In 1974, Hawaii established the Natural Energy Laboratory (NELHA) to study OTEC technology at Keahole Point on the Kona coast. A picture of this facility is shown in Figure 1.11. In 1979 NELHA built the first system to produce net power, "Mini-OTEC." This was a closed-cycle plant mounted on a converted US Navy barge. It produced 52 KW of gross power and 15 KW of net power (Survey, 2007).

In 1980, the US Department of Energy (DOE) built OTEC-1, a test site for OTEC heat exchangers, on board a converted US Navy tanker. They tested commercial-scale heat exchanger designs and demonstrated that OTEC can operate from slowly moving ships with minor impact on the environment (Survey, 2007).

In 1981, Japan built a 100 KW (gross) closed-cycle shore-based plant in the Republic of Nauru in the Pacific Ocean. It had a net power production of 31.5 KW, exceeding production expectations (Survey, 2007).

In May 1993, an open-cycle OTEC plant at NELHA produced 50 KW of net power (US Department of Energy). In 2001, the National Institute of Ocean Technology (NIOT) in India implemented a 1-MW closed-cycle pilot OTEC plant in the south east coast of India (Kobayashi et al. 2001).

Currently, private corporations have displaced government laboratories as the major contributors to OTEC development. For example, in 2002, SEA Solar designed a 100-MW plant-ship to the US Navy (Sea O2, 2004).

In 2009, Lockheed Martin was awarded $12.5 million from the U.S. Naval Facilities Engineering Command to make progress in the design of an OTEC pilot plant off the coast of Hawaii intended to lead to the later development of large-scale OTEC plants (Lockheed Martin).

In 2011, the Bahamas Electricity Corporation (BEC) and a private company signed a contract to develop two OTEC plants to be implemented in the islands to provide energy. These plants will be the first OTEC plants to be used commercially (Ocean Thermal Energy Corporation, 2013).

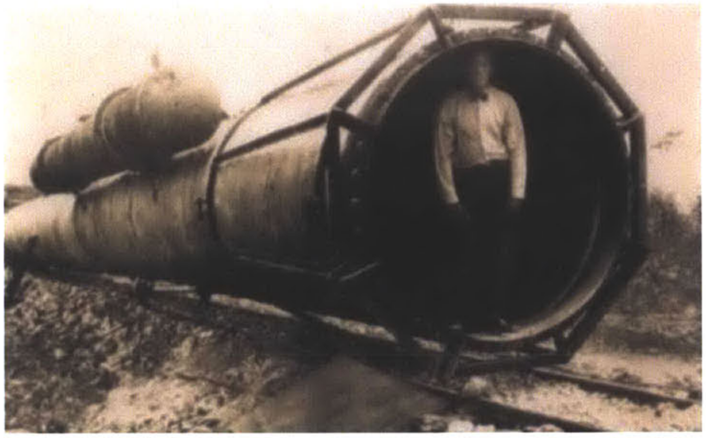

Figure 1.8 - Cold water pipe used in Cuba by Dr. Claude (Offshore Infrastructure Associates, Inc., http://www.offinf.com/history.htm).

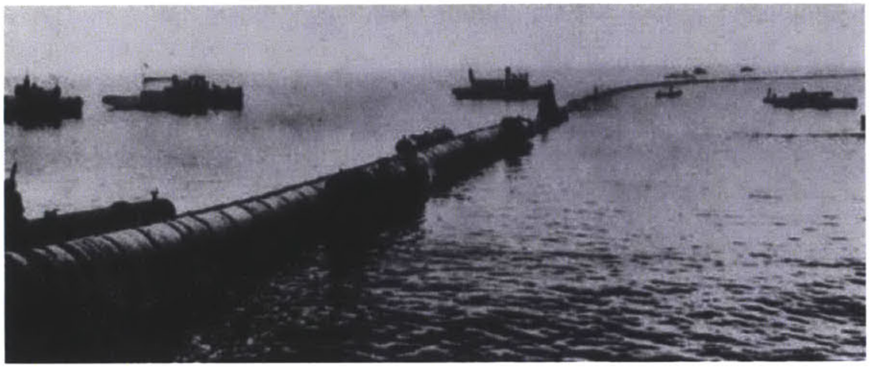

Figure 1.9 - Installation of the cold water pipe in Cuba (Offshore Infrastructure Associates, Inc., http://www.offinf.com/history.htm).

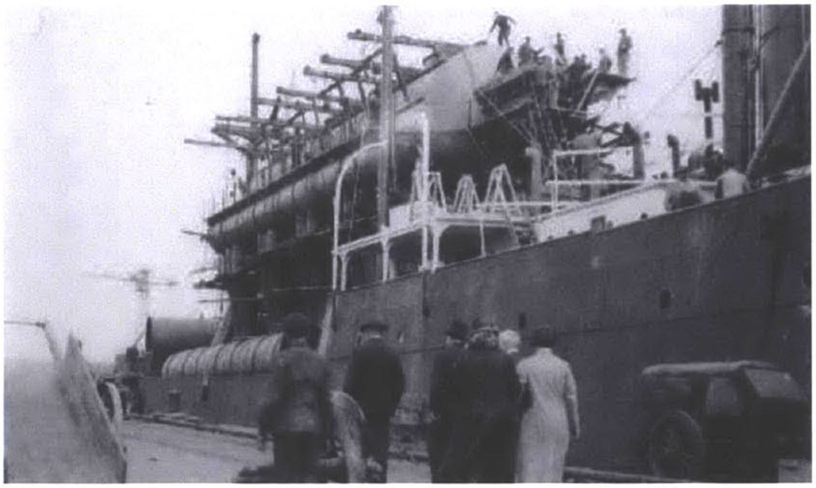

Figure 1.10 - Ship on which OTEC plant was installed in Brazil (Offshore Infrastructure Associates, Inc., http://www.offinf.com/history.htm).

Figure 1.11 - A land based OTEC facility at Keahole Point on the Kona coast of Hawaii (United States Department of Energy).

1.5 Prospect for OTEC

According to the U.S. Energy Information Administration, world energy consumption is estimated to grow by 53% from 2008 to 2035. Figure 1.12 shows the estimated world energy consumption by fuel. During this time, fossil fuel prices are expected to rise, which in addition to environmental concern, leads to a decrease in their total contribution to the world energy market from 34% to 29%. One of the biggest sources of energy projected to replace this gap is from renewable energy. Renewable energy production is expected to rise from 10 % in 2008 to 14% by 2035.

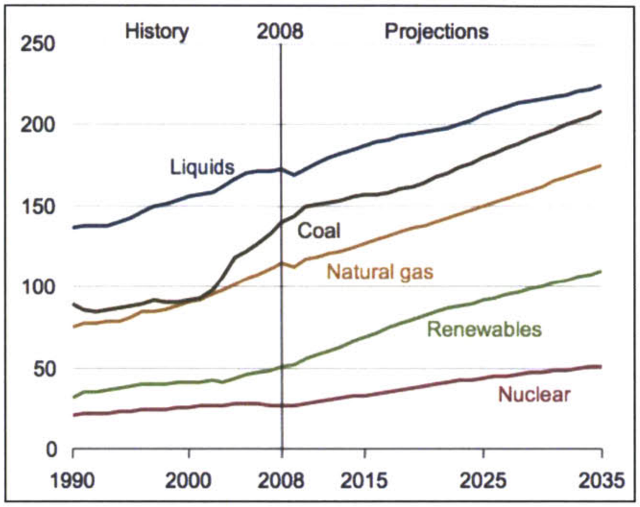

Figure 1.12 - World energy consumption by fuel, 1990-2035 in quadrillion BTU (US Department of Energy/EIA 2011).

OTEC plants are an attractive form of this renewable energy. The favorable locations for OTEC plants (60 million km^2) store the energy equivalent to the heat of 245 billion barrels of oil. As reference, only 0.1% of this amount equals 15 times the current US electricity consumption (US Department of Energy, 2011). Several renewable energy sources such as winds, solar, and ocean waves, are variable in output power. In contrast, OTEC can be considered a base-load technology, which makes it an appealing renewable source of energy.

1.6 Previous Work on OTEC Modeling

In the 1970s many physical models were developed to understand the interaction between the OTEC plant intake and the discharge, and other local environmental impacts. Sundaram et al. (1978) conducted some experiments to identify the variables that affect the effluent recirculation. Adams et al. (1979) performed many experiments analyzing realistic ambient stratification profiles, and realistic ocean currents. They considered different variables: the evaporator intake flow rate, evaporator intake depth below water surface, evaporator and condenser combined discharge depth below water surface, combined discharge flow rate, discharge vertical angle, plant characteristic sizes, background currents, and discharge and ambient densities. They concluded that effluent recirculation from a plant with radial discharge can be reduced by an adequate choice of separation between the plant intake and discharge. This study is limited to the immediate surrounding of the OTEC plant.

Concurrently, some investigators started to model this numerically. Jirka et al. (1977), proposed a theoretical model based on the potential flow hypothesis and a two-dimensional continuity equation, considering the OTEC discharge as a source and assuming uniform background flow, with either a two-layer or linear stratification profile. The proposed flow field is two-dimensional and extremely simplified. Roberts (1977) proposed a simplified two-dimensional numerical model to study the flow near two outflows and a warm inflow of an OTEC plant. Because of the limitations and simplifications of the model, they reached qualitative results rather than quantitative. They concluded that recirculation can be avoided and that it is possible to capture warm water with a temperature very close to the surface temperature by limiting the intake velocity and the separation between the intake and the discharge. Wang (1984) conducted a study of the far field of OTEC discharge at regional scales using a general circulation model but without treating the behavior of the effluent in detail. The plume discharge is represented just by a source of mass and heat into a far field model. The warm and cold water intake are not included in the model. This model was able to predict plume characteristics and velocities for a 40 MW OTEC plant considering both quiescent ambient conditions and background currents.

Over the next 30 years, very little research was conducted on theoretical modeling of OTEC plants. OTEC plants had to compete with wind and solar energies, and due to their complexity and very low efficiency were no longer pursued. Difficulties in plant construction, vulnerability to bad weather conditions (waves, storms), and uncertain profitability slowed its development.

Recently, there has been renewed interest in developing OTEC plants. Even with wind and solar, there is once again a high demand for new renewable energy sources, including OTEC plants. This lead to numerical modeling of OTEC plants to be studied again. A private company in Hawaii involved with Lockheed Martin is pursuing OTEC modeling and experiments to develop this technology for Hawaii.

Rajagopalan and Nihous (2013), for the first time made an estimation of the global OTEC resource using an ocean general circulation model. They assumed a uniform distribution of OTEC plants in the favorable locations (between 15°N and 15°S latitude). Each plant is modeled by sources representing the effluent discharge, and sinks representing the intakes. They studied effects for a time span of 1000 simulated years, using a horizontal 4°x4° grid size. They conclude that the maximum net OTEC power production possible on Earth is 30 TW. However, this study does not use a realistic representation of the OTEC plumes discharge since it does not account for the entrainment process, which requires extremely fine spatial resolution, or a small scale and large scale coupling strategy as presented in this thesis.

1.7 Research Objectives

The objective of this research is to develop numerical models to study the external fluid mechanics associated with OTEC plants operating in the tropical oceans. These models are detailed in the following chapters. The possibility of using a state-of-the-art ocean general circulation model is explored. This study aims to identify interaction of adjacent plants since how closely OTEC plants can operate is still unknown.

This thesis studies:

- Interaction between plumes of adjacent plants
- Redistribution of ocean nutrients

applied to:

- Small and large OTEC power plants
- Both quiescent environment and background currents

1.8 Thesis Outline

This thesis is organized in six chapters. Chapter 1 presents an overview of the general background and principles of Ocean Thermal Energy Conversion. Chapter 2 describes the characteristics of OTEC external flows. The models used to study the external flow of OTEC plants, a near, an intermediate and a far field model, are described in Chapter 3. Typical OTEC discharges as well as the effect of background currents are also studied in this chapter. Chapter 4 explores the strategy of coupling the models by two methods: the *Brute Force* method and the *Distributed Sources and Sinks* method, studying their applicability to OTEC problems. Chapter 5 presents the impact of OTEC plants on induced upwelling velocities and ocean nutrient redistribution. Finally, Chapter 6 summarizes the results and proposes direction for future research.

Chapter 2 - OTEC External Flows

2.1 General Characteristics

An OTEC plant takes in both warm seawater from near the surface and cold water from a depth varying from 800 to 1000 m. An operating OTEC plant represents a combination of sources and sinks of mass (discharges and intakes) operating in the stratified ocean. To exploit the small effective temperature difference of the water at the intakes, an OTEC plant pumps large volumes of water, about 4 m^3/s of deep cold seawater and at least as much surface warm seawater per net megawatt of electrical power. As reference, a 100-MW power plant with 20°C seawater temperature difference, corresponding to an effective temperature difference across the heat engine of 10°C, operating at an efficiency of 3%, requires a cold water intake flow and warm water intake flow of 400 m^3/s each, which is equivalent to eighty times the average Charles River flow. Therefore, the source-sink system is expected to produce significant impact in the ambient temperature structure and ocean currents. A schematization of these effects is shown in Figure 2.1.

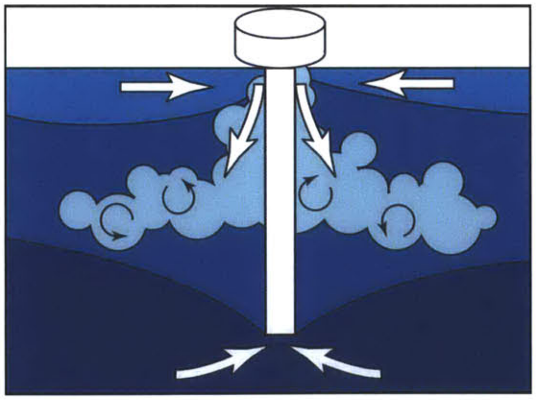

Figure 2.1 - Scheme of an OTEC intake flows and discharge plume, causing deformation of the ocean thermal structure (Dr. Jason Goodman, personal communication 2009).

The external flow generated by an OTEC plant is crucial since the plant interacts with itself by:

- Alteration of the ambient stratification. The discharge jets generate turbulent mixing of the upper warm layers. This may cause a reduction of the mixed layer temperature, or can induce non-selective withdrawal from the upper mixed layer in the warm intake by taking colder water form the upper thermocline.
- Direct or indirect recirculation. Effluent or water entrained by the jet discharge can be recirculated into inflows.

All these processes can cause the degradation of the thermal resource available. The effluent recirculation is affected by the intake design characteristics (distances between water intake and water discharge), the flow rates, the initial effluent buoyancy, the presence of background currents, and the thickness of the mixed layer.

This study aims to determine whether OTEC plant performance can be diminished by potential recirculation of the discharge or alteration of ocean temperature structure. This study analyzes offshore closed cycle OTEC plants. Figure 2.2 presents a schematic of an OTEC plant structure and typical water intake and exhaust temperatures.

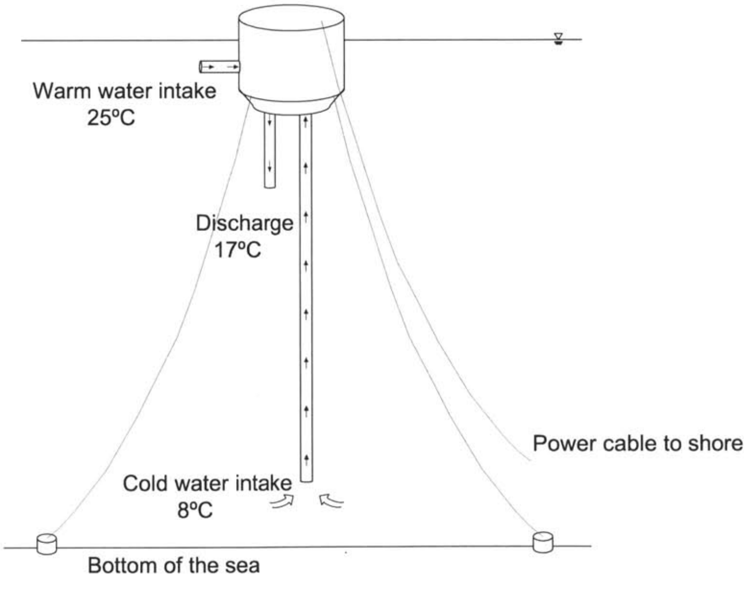

Figure 2.2 - OTEC combined discharge general scheme, indicating typical intake temperatures and typical effluent temperature for a 100-MW power plant.

2.2 Warm Water Intake

The warm intake structure is located near the sea surface. Typical designs for pilot plants consist of an intake at 10 m depth, while for commercial plants (which require larger flow rates), the intake is located at 20 m depth. The intake withdraws water from different levels (depending on the stratification profile, the pumped flow and background currents). The goal is to capture water only from the upper mixed layer where water is the warmest. The temperature difference between cold and warm water intake determines the maximum possible plant energy production. A change in this temperature difference significantly affects the power production. For example, a decrease of 1° C in this temperature difference typically would result in a 15% decrease in net OTEC power production (Nihous, 2010). Warm intake flow rates are in the range of 3-5 m^3/s per MW (Myers et al., 1986).

2.3 Cold Water Intake

Cold water is pumped up though a 750 m to 1-kilometer long pipe. The exact choice of intake depth is a tradeoff between the costs of a longer pipe and more energy needed to pump the water, and the thermal efficiency gained by using colder water in the Rankine cycle. An OTEC plant uses similar cold flow and warm flow rates, 3-5 m^3/s per MW, (Myers et al., 1986). However, in order to reduce the cost of the pumping, the plant operates with smaller cold flow. The cold intake is not expected to interfere with the warm water intake because of the large distance between them. The simulations carried out verify this.

2.4 Discharge

The warm and cold water exhaust can be either combined or mixed, as illustrated in Figure 2.3. In the separate discharge configuration, separate discharge structures for the warm and cold waters are used, while in the mixed discharge configuration the same discharge structure is used for both. The discharge may consist of a single discharge pipe, several discharge pipes or a multiple port diffuser. OTEC discharge design is crucial, since it can affect the operation of the plant itself and the environment. The goal in its design is to avoid effluent recirculation into the warm intake, which may lead to a reduction of the efficiency of the plant.

The temperature of the seawater effluent from an OTEC plant is different from the temperature of the ocean at the released depth. Depending on whether the discharge is combined or separate, the effluent can be positively or negatively buoyant. In the case of a separate cold discharge, considering typical temperatures of the ocean and effluent, the cold effluent is denser than the ambient water. In a combined discharge the resulting density difference with the ambient is smaller. In the separate warm water discharge, the density difference is very small, as just a few degrees Celsius are lost as heat is extracted by the evaporator (Nihous, 2007).

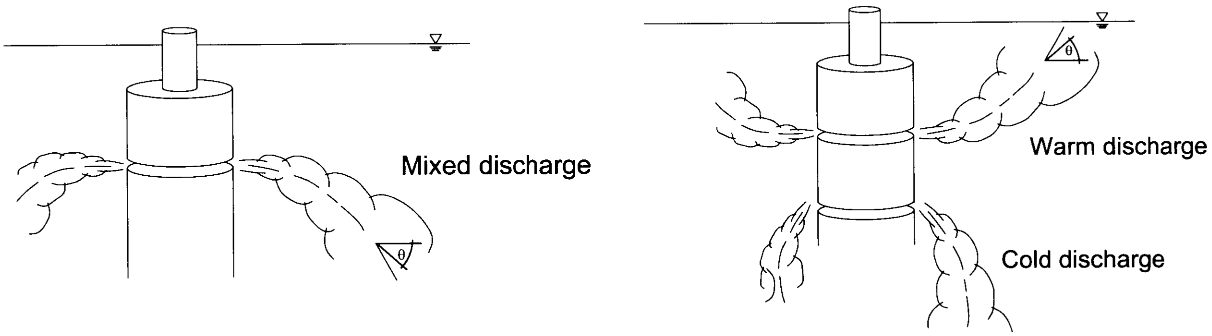

Figure 2.3 - Different OTEC discharge schemes (adapted from Fry and Adams, 1983).

Once the effluent is discharged into the ambient, its dynamics are controlled by the discharge momentum, background currents, and by its initial buoyancy. The discharged plume sinks or rises depending on its density. While it sinks, or rises, it mixes with ambient water reducing the density difference respect to the ambient, until reaching a depth where the average density of the diluted effluent equals the ambient ocean.

2.5 Flow Rates

There are three degrees of freedom to operate a given OTEC system:

1. cold seawater flow rate
2. warm seawater flow rate

3. working fluid flow rate

The ratio of the cold and warm flow rate is a variable of design. It depends on the thermal resource available and the energetic cost of the seawater and the working fluid pumping. In general designs, this parameter varies from one to two. In this study it is assumed a ratio of the warm water intake over the cold water intake of 1.25.

Table 2.1 shows the typical flow rates for 10 and 100-MW OTEC plant size, assuming a ratio between cold and warm intake of 1.25.

Table 2.1 - Typical OTEC flow rates.

Power	Q_{cold} **(m³/s)**	Q_{warm} **(m³/s)**	Q_{warm}/Q_{cold}	Q_{total} **(m³/s)**
100 MW	320	400	1.25	720
10 MW	32	40	1.25	72

2.6 Ambient Temperature Profile

As described in Section 1.3, the ocean has an upper warm mixed layer above the thermocline region and an almost isothermal region close to the bottom of the ocean. The depth of the mixed layer, the steepness of the thermocline, and the water temperature depend on the particular region of the earth considered. For this analysis we assumed a typical ocean temperature profile with a 50 m mixed layer thickness followed by gradual decrease in temperature with depth as shown in Figure 2.4.

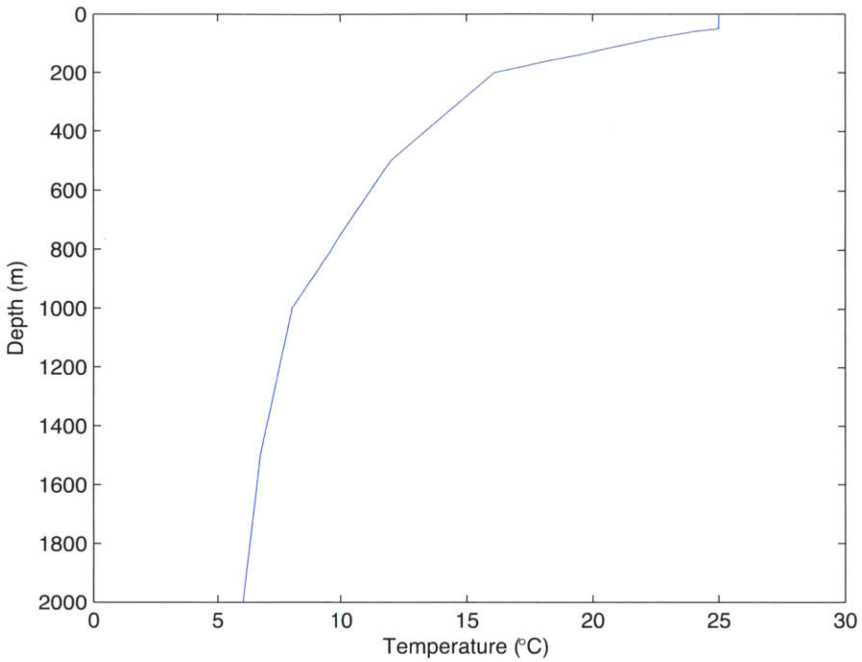

Figure 2.4 - Typical ocean ambient temperature profile (data from Paddock and Ditmars, 1983).

2.7 Exhaust Temperatures

A relevant characteristic of OTEC effluents, which affects the dilution achieved further downstream, is its initial buoyancy. Typical temperature differences between the OTEC effluent and the environment water at the discharge level for a 100-MW power plant are:

- 4.1°C for the combined exhaust (negatively buoyant)
- 12.5°C for the separate cold exhaust (negatively buoyant)
- -0.7°C for the separate warm exhaust (positively buoyant)

Table 2.2 presents the characteristics of the separate and combined discharges. To compute the temperature difference between the effluent and the ambient, ΔT, it is assumed that heat exchange with the evaporator and condensers leads to variations of temperature of 1°C in each separate discharge outflow. For the combined discharge case, the heat lost in the evaporator and the heat gained in the condenser are approximately in balance in the OTEC combined outflow.

Table 2.2 - Typical temperature differences between OTEC exhausts and ocean water.

	Depth (m)	**$T_{ambient}$ (°C)**	**$T_{exhaust}$ (°C)**	**ΔT (°C)**
Warm discharge	70	23.3	24	-0.7
Cold discharge	100	21.5	9	12.5
Combined discharge	100	21.5	17.4	4.1

The initial temperature difference between the effluent and the ambient ocean in a combined discharge is small, 4.1°C, and therefore the effluent plume is not expected to sink much.

Chapter 3 - Modeling Tools

3.1 Plume Dynamics Scales

Different length scales are involved in the study of the OTEC external flow. Figure 3.1 schematizes the near, intermediate and far field of an OTEC discharge. To solve both the millimeter-scale turbulence mixing and the kilometer-scale of regional hydrodynamics involved in the study of OTEC plumes, one single model is not sufficient since computer power is limited.

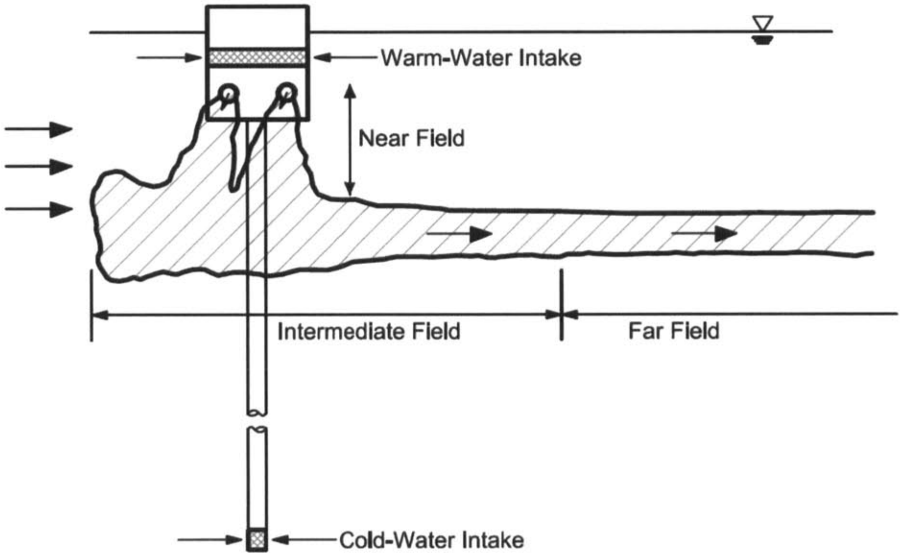

Figure 3.1 - Scheme of OTEC discharge, identifying near, intermediate and far fields (Paddock and Ditmars, 1983).

The plume dynamics scales can be divided into:

1. *Near field*

   Time scales are of order of minutes and length scales are tens to hundreds of meters

2. *Intermediate field*

   It is the region where plume collapses. Time scales are of order of hours.

3. *Far field*

   Ambient currents and the Coriolis force drive the plume dynamics. Turbulent diffusion is the main mechanism of dilution. Time scales are of order of hours and length scales are of order of kilometers.

3.2 Ambient Stratification

The main feature of the OTEC plume dynamics is the stratification of the ambient due to non-uniform vertical temperature profile. Considering a combined discharge, initially, the effluent is denser (colder) than the ambient. The plume entrains fluid from the ambient until reaching a level where it becomes neutrally buoyant respect to the ambient. Due to the vertical momentum gained, the plume overshoots the level of neutral buoyancy. At this point, the plume is still lighter than the ambient, so it rises until reaching the neutrally buoyant depth.

Different depths can be identified over the plume trajectory in a stratified ambient:

1. *Neutral buoyancy level*

   Corresponds to the first elevation where the ambient density coincides with the density of the plume.

2. *Peak depth*

   Corresponds to the maximum depth reached in the trajectory. At this level the vertical velocity vanishes and the vertical acceleration is a maximum.

3. *Trapping depth*

   Corresponds to the elevation where the plume finally gets trapped due to ambient stratification. In this approach, it is defined as the elevation where the plume and ambient density difference vanishes after the plume has reached its peak depth.

   The mathematical model used predicts an infinite number of oscillations in the trajectory around the equilibrium depth after the trajectory reaches its peak. In reality, these oscillations are damped by turbulence and viscosity. Therefore, the mathematical model will not be used beyond the second elevation of neutral buoyancy.

Figure 3.2 shows the centerline trajectory and ambient density minus plume centerline density. In the graph we can identify the first *Neutral buoyancy level*, *Peak depth* and the *Trapping depth*.

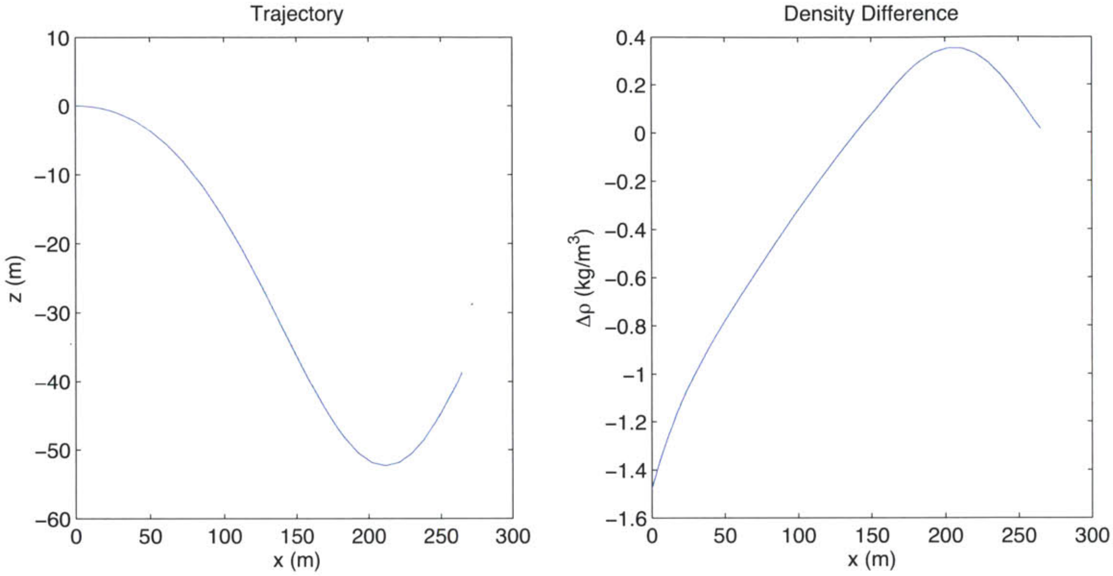

Figure 3.2 - Plume centerline trajectory and ambient density minus plume centerline density for a 100-MW OTEC combined exhaust plant in a typical stratified ambient.

To model the near and intermediate fields, we used analytical models. To model the far field we used a General Circulation Model: MITgcm.

3.3 Near Field Model

In the neighborhood of the OTEC discharge, the jet dynamics can be well resolved by a validated integral model, which predicts the properties of the jet by conservation principles. The flow and the excess density with respect to the ambient are assumed to be self-similar after a zone of flow establishment, with the mean axial velocity and excess density having a Gaussian distribution, as illustrated in Figure 3.3. The mean axial velocity and the excess density with respect to the ambient along the centerline direction are expressed as:

$$u(s,r) = u_c(s)e^{-\left(\frac{r}{b}\right)^2}$$

$$\Delta\rho(s,r) = \Delta\rho_c(s)e^{-\left(\frac{r}{\lambda b}\right)^2}$$

where u_c and $\Delta\rho_c$ are the centerline maximum velocity and excess density defined as $\Delta\rho_c = \rho_a(z) - \rho_c$, ($\rho_a$ is the ambient density), b is the jet radius defined by the location with velocity $e^{-1}u_c, s$ is the local jet coordinate following the centerline, and r is the radial coordinate perpendicular to the centerline. The parameter λ is a dispersion ratio, which accounts for the faster spreading rate of scalar quantities than velocity ($\lambda > 1$).

The conservation equations are integrated over a cylindrical element control volume, yielding a set of ordinary differential equations. The longitudinal turbulent fluxes are neglected in the integral magnitudes. The density difference between the flow and the ambient fluid is assumed to be small, (Boussinesq approximation, $\frac{\Delta\rho}{\rho} << 1$), thus density differences can be neglected in the governing equations except in the terms multiplied by g (gravity constant). The fluid is assumed incompressible.

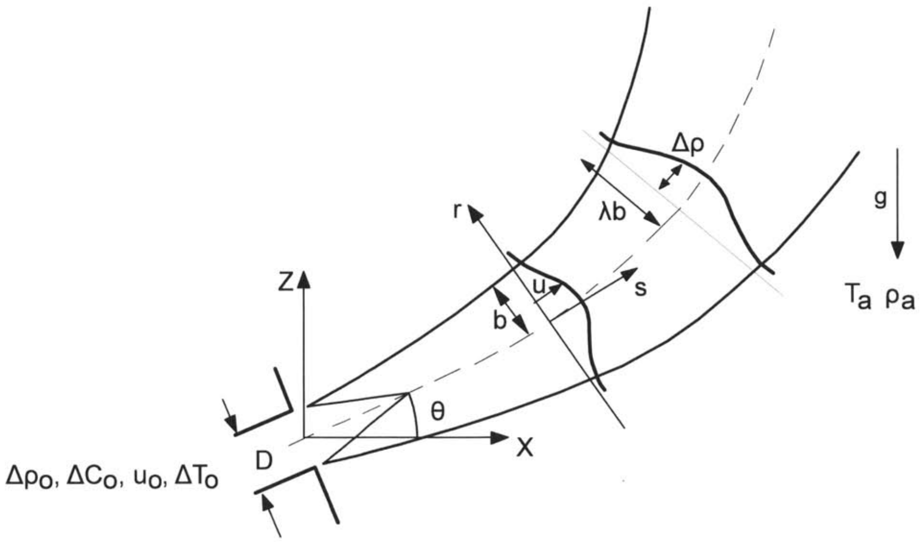

Figure 3.3 - Gaussian profiles of velocity and excess density for a buoyant jet (adapted from lectures by E. Adams, spring 2010).

3.3.1 Ambient Currents

In order to develop a more general near field model, we included background currents. The background flow is assumed to be in the *x* direction. Figure 3.4 sketches a three-dimensional buoyant jet discharge into ambient flow, and presents all the variables involved in the following formulation.

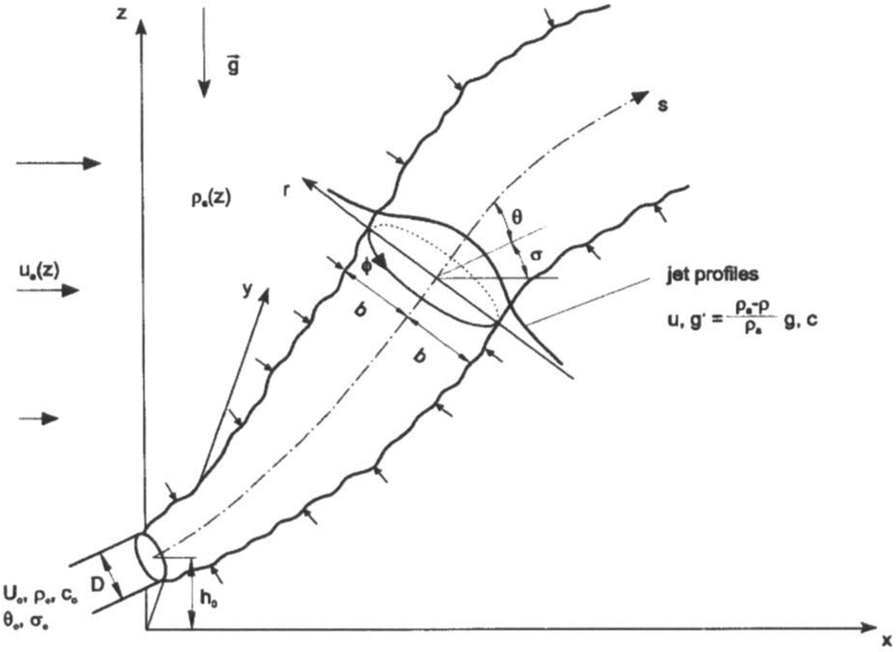

Figure 3.4 - Three-dimensional buoyant jet discharged into ambient flow with global (x,y,z) and local (s,r) coordinate system (Jirka, 2004).

In spherical coordinates, σ and θ, the velocity and density excess can be written as:

$$u(s,r) = u_c(s)e^{-\left(\frac{r}{b}\right)^2} + u_a \cos\sigma \cos\theta$$

$$\Delta\rho(s,r) = \Delta\rho_c(s)e^{-\left(\frac{r}{\lambda b}\right)^2}$$

The velocity profile is assumed to be similar and Gaussian above the component of the ambient velocity $u_a \cos\sigma \cos\theta$.

In the following equations we introduce the buoyancy defined by $g' = \frac{\rho_a(z)-\rho}{\rho_{ref}} g$, where ρ_{ref} is a constant reference density consistent with the Boussinesq approximation. Therefore the buoyancy is defined as $g' = g'_c e^{-\left(\frac{r}{\lambda b}\right)^2}$.

3.3.2 Integral Quantities

Integrating through the cross-section of the jet we can define the following bulk variables (Jirka, 2004):

- Volume flux

$$Q = 2\pi \int_0^{R_j} urdr = \pi b^2 (u_c + 2u_a \cos\theta \cos\sigma)$$

- Axial momentum flux

$$M = 2\pi \int_0^{R_j} u^2 rdr = \frac{1}{2} \pi b^2 (u_c + 2u_a \cos\theta \cos\sigma)^2$$

- Buoyancy flux

$$B = 2\pi \int_0^{R_j} ug'rdr = \pi b^2 \left(u_c \frac{\lambda^2}{1+\lambda^2} + \lambda^2 u_a \cos\theta \cos\sigma\right) g'_c$$

The integration limit of these magnitudes, R_j, is usually taken to be infinity. However, the crossflow contributions in the integrals for the volume flux, Q, and the axial momentum flux, M, do not yield finite magnitudes. Therefore, in these two cases, the integration limit, R_j, is defined as $R_j = \sqrt{2}b$. For the velocity profile stated above, at $R_j = \sqrt{2}b$, the local excess velocity reaches 14% of the centerline value, and the tracer concentration reaches 22% of the centerline value, assuming a typical value for λ of 1.15.

3.3.3 Conservation Equations

The conservation principles for the flux quantities defined in the previous section are applied to a jet element of length *ds* centered on the trajectory, as proposed by Jirka (2004). In the derivation of these equations the pressure deviations from hydrostatic within the jet and the acceleration effects due to jet curvature are neglected as well as the turbulent fluxes relative to the mean fluxes in the momentum and scalar terms.

The conservation principles can be stated as:

1. *Continuity*

$$\frac{dQ}{ds} = E$$

The term E represents the entrainment rate.

2. *Horizontal momentum in the x-direction (along the current direction)*

$$\frac{d(M cos\theta cos\sigma)}{ds} = E u_a + F_D \sqrt{1 - cos^2\theta cos^2\sigma}$$

The term F_D represents the ambient drag force acting on the jet element.

3. *Horizontal momentum in the y-direction (perpendicular to the current direction)*

$$\frac{d(M cos\theta sin\sigma)}{ds} = -F_D \frac{cos^2\theta sin\sigma cos\sigma}{\sqrt{1 - cos^2\theta cos^2\sigma}}$$

4. *Vertical momentum*

$$\frac{d(M sin\theta)}{ds} = \pi\lambda^2 b^2 {g'}_c - F_D \frac{sin\theta cos\theta cos\sigma}{\sqrt{1 - cos^2\theta cos^2\sigma}}$$

5. *Buoyancy in a stratified ambient, being $\rho_a(z)$ the ambient density*

$$\frac{d(B)}{ds} = Q\frac{g}{\rho_{ref}}\frac{d\rho_a}{dz}sin\theta$$

Furthermore, the geometry of the trajectory is defined by:

$$\frac{dx}{ds} = cos\theta cos\sigma$$

$$\frac{dy}{ds} = cos\theta sin\sigma$$

$$\frac{dz}{ds} = sin\theta$$

The local jet variables can be obtained from the integral variables by the following relations:

$$u_c = \frac{2M}{Q} - 2u_a cos\theta cos\sigma$$

$$b = \frac{Q}{\sqrt{2\pi M}}$$

$$g_c{}' = \frac{B}{\pi b^2\left(\frac{u_c\lambda^2}{(1+\lambda^2)} + \lambda^2 u_a cos\theta cos\sigma\right)}$$

The above conservation equations lead to a system of non-linear, coupled, differential equations that allows one to solve for the six unknowns along the jet trajectory: $u_c, \Delta\rho_c, b, x, y,$ and z.

Similarly, a tracer concentration has a Gaussian distribution. We can also keep track of the centerline concentration c_c, by solving an additional conservation equation for the tracer flux. This allows us to compute the tracer distribution within the buoyant jet and the centerline dilution. It is known that the centerline dilution is $\frac{1+\lambda^2}{\lambda^2}$ times the average volumetric dilution.

3.3.4 Turbulent Closure

To solve this system of equations numerically, another closure equation is required. The expression for entrainment, E, and the drag force, F_D, defines the turbulence closure in the integral model.

The entrainment rate, E, accounts for the streamwise and azimuthal shear mechanisms responsible for the ambient fluid entrainment into the turbulent jet. It is defined by:

$$E = 2\pi b u_c\left(\alpha_1 + \alpha_2 \frac{sin\theta}{{F_l}^2} + \alpha_3 \frac{u_a cos\theta cos\sigma}{u_a + u_c}\right) + 2\pi b u_a\sqrt{1 - cos^2\theta cos^2\sigma}\alpha_4|cos\theta cos\sigma|$$

The streamwise entrainment terms, proportional to the centerline velocity u_c, accounts for the effects of:

1. Pure jet, represented by α_1
2. Pure plume, represented by α_2, which depends on the angle θ and is inversely proportional to the square of the local densimetric Froude number $F_l = \frac{u_c}{\sqrt{g'_c b}}$
3. Pure wake, represented by α_3, which is proportional to the wake parameter $\frac{u_a}{u_c+u_a}$

The entrainment velocity is defined at a radial distance b, the e^{-1} width. The azimuthal entrainment is proportional to the ambient velocity component transverse to the jet $u_a\sqrt{1 - cos^2\theta cos^2\sigma}$, with coefficient α_4, and the term $|cos\theta cos\sigma|$ accounts for the angle between the jet axis and the currents.

The following coefficients are used:

$$\alpha_1 = 0.055$$

$$\alpha_2 = 0.6$$

$$\alpha_3 = 0.055$$

$$\alpha_4 = 0.5$$

The jet drag force F_D is defined as a quadratic function:

$$F_D = C_D \frac{2\sqrt{2}b\, u_a{}^2(1 - cos^2\theta cos^2\sigma)}{2}$$

where the term C_D is the drag coefficient, $2\sqrt{2}b$ represents the jet diameter, $u_a\sqrt{1 - cos^2\theta cos^2\sigma}$ represents the transverse velocity component. The drag force is defined in analogy to the flow around a cylinder.

3.3.5 Solution Method

The system of coupled partial differential equations is solved by a fourth-order Runge-Kutta algorithm programmed in MATLAB. Initial conditions have to be specified. The numerical solution is computed from the discharge point until the point of neutral buoyancy, which is considered the end of the near field.

3.3.6 Zone of Flow Establishment

When the jet is first discharged, its velocity and excess density profile are constant in a central zone, called the Potential Core, as shown in Figure 3.5. Outside this region, the velocity and density profiles decay. After a certain distance, the jet exhibits a Gaussian profile. The region within this distance is defined as the Zone of Flow Establishment.

Experiments show that the length of this zone is 6.2 times the discharge diameter for round axisymmetric jets (Lee and Chu, 2003). For OTEC typical discharge sizes, the corresponding lengths are of the order of 100 m, which represent a significant horizontal extent with respect to the horizontal development of the jet itself. To model this zone, we need to assume parameters and simplifications not always verifiable. Therefore proposing a model for this zone would be complex and not necessary accurate.

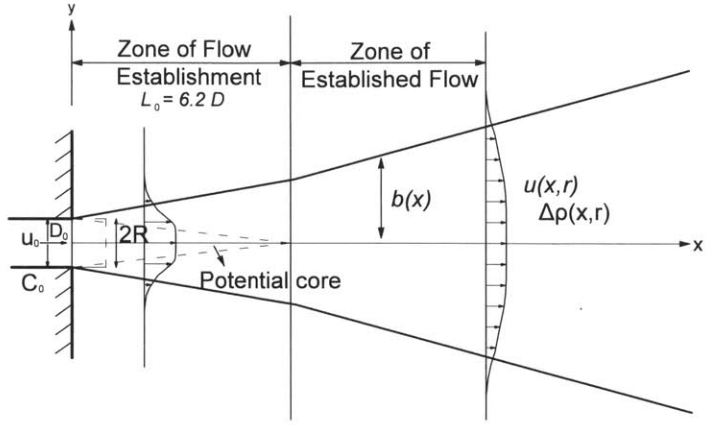

Figure 3.5 - Jet showing Zone of Flow Establishment and Zone of Established Flow (Lee and Chu, 2003).

We assumed Gaussian profiles in the magnitudes, and conservation of mass, momentum and buoyancy from the discharge section to the beginning of the jet development as initial conditions for the numerical solution. We also assumed a discharge velocity of 2 m/s to determine the diameter of the jet discharge.

3.3.7 Turbulent Fluctuations Terms

In this study a first order integral model is used, since second order terms due to turbulent fluctuations in the mass and momentum fluxes are neglected. It is known that neglecting the velocity and mass fluctuations in the cross section integrals introduces an error of about 10% (Wang and Law, 2002), which is considered acceptable.

3.3.8 Earth Rotation

The plumes are released into the open ocean, and are subjected to the Coriolis effect. The horizontal distance at which the plumes reach the neutral buoyant depth are of order of 100 m for the range of volume fluxes involved in OTEC discharges. This distance is significantly smaller than the Rossby Radius of deformation, $L_R = \frac{NH}{f}$, which is about 56 km based on H =500 m, N =4.23x10^{-3} s^{-1} and f =3.7x10^{-3} s^{-1} for a latitude of 15°, where f is the Coriolis parameter defined as $f = 2\omega sin\theta$ (ω is the earth's angular velocity and θ is the latitude), H is the scale height, and N is the stratification frequency of the ambient. For the range of flow rates considered, assuming quiescent background, the time required by the plumes to reach their neutral buoyant level is of the order of a few minutes. This time scale is much smaller than the rotation period of the earth. Given the magnitude of the time and length scales of the near field of OTEC discharge, the earth rotation effect is negligible in the near field plume dynamics.

3.3.9 End of Near Field

The end of the near field is arbitrary since there is no clear limit between the near field and intermediate field. In this study it is defined as the location where the plume reaches for the second time the neutrally buoyant depth. The time required to reach the equilibrium depth is computed by:

$$t = \int_0^{NF} \frac{ds}{u(s)}$$

In the model, the integral term is computed numerically.

3.3.10 Results

In this section we present the near field characteristics of a 100-MW power plant, with warm and cold combined water discharge (400 m^3/s warm water intake and 320 m^3/s cold water intake) located 100 below the water surface. The ambient is assumed to be quiescent and stratified, and the initial discharge is assumed to be horizontal.

Figure 3.6 shows the trajectory described by the center of mass of the cross of the section of the plume, the centerline velocity along the local progressive, the dilution and the plume radius. The discharged fluid is colder than the environment; therefore the effluent sinks until reaching a depth where the density of the plume is equal to the density of the stratified ambient. The centerline describes a plane trajectory that reaches its neutrally buoyant depth 38.6 meters below the discharge depth. The plume overshoots its neutrally depth due to the vertical momentum gained. The centerline velocity decays until reaching values of 0.8 m/s at the end of the near field. The volumetric dilution achieved at the end of the near field is 5.4. The plume radius grows reaching a magnitude of 39.2 m at the end of the near field. The horizontal extent of the plume development is 265.1 m. The time required to reach the equilibrium depth is 3.4 minutes.

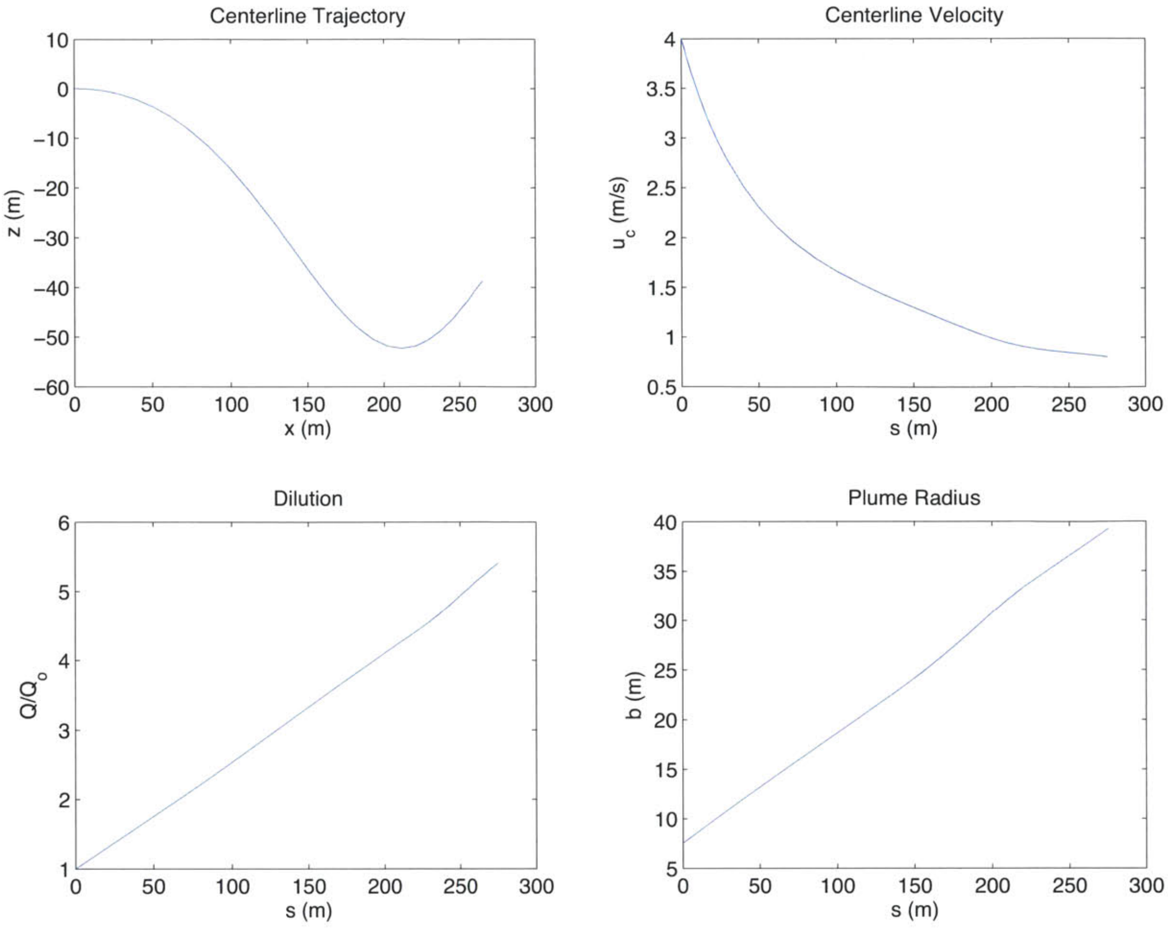

Figure 3.6 - Near field plume characteristics for a 100-MW OTEC plant with combined discharge.

The same OTEC effluent characteristics (warm and cold volume flux, discharge depth) presented in this section are used to analyze the effect of a coflow and a crossflow current in the near field in the following two sections.

3.3.11 Effect of a Coflow Current on Near Field Mixing

Different magnitudes of background current in the same direction as the initial jet momentum are considered to analyze its impact on the near field mixing. Figure 3.7 shows the plume dilution, the equilibrium depth, the time and the horizontal distance to reach the equilibrium depth, the centerline velocity, and the plume radius at the end of the near field as functions of the magnitude of the current.

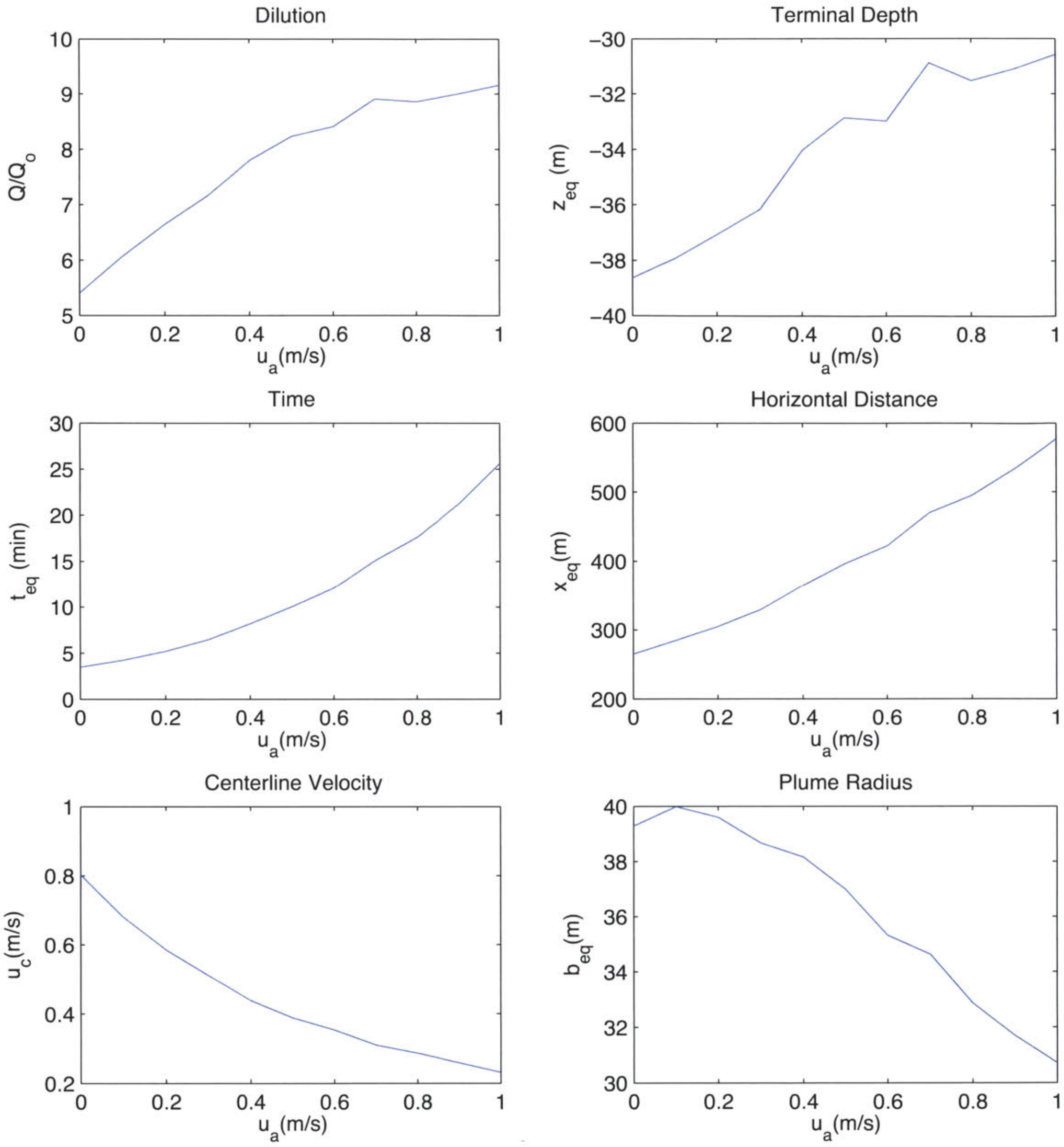

Figure 3.7 - Effect of coflow current on mixing and plume characteristics at the end of the near field.

From the previous results the following conclusions can be drawn. As a general trend, dilution increases as the background current increases. The final trap depth generally decreases due to the enhanced mixing. As expected, the horizontal distance where the plume finds its neutrally buoyant depth increases as the ambient current increases, as does the time required for the plume to reach neutrally buoyant depth. The final centerline excess velocity with respect to the ambient flow decreases as the background current increases. In general, the radius of the plume at the end of the near field decreases with the magnitude of the current.

3.3.12 Effect of a Crossflow Current on Near Field Mixing

Different magnitudes of the angle between the initial jet momentum and the background current, σ, ranging from 0 to 90 degrees, are considered to analyze its impact on the near field mixing. A constant background current along the *x* direction of 0.1 m/s is considered. Figures 3.8-3.10 show top and vertical views of the centerline trajectories for five angles.

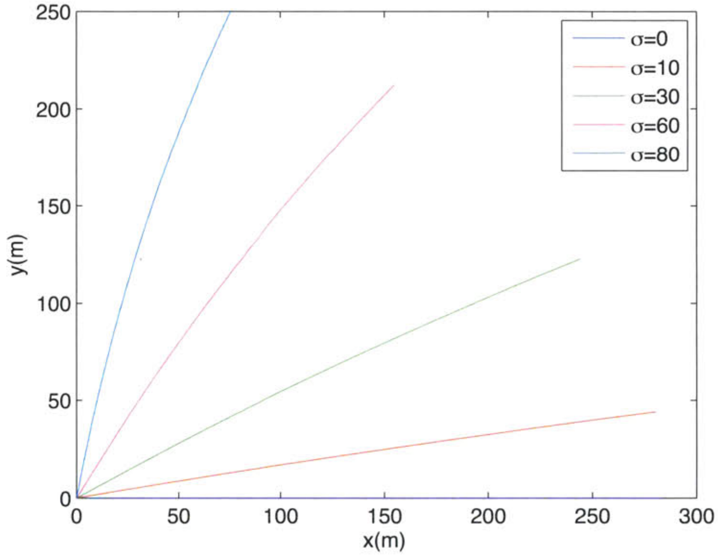

Figure 3.8 - Top view of the centerline plume trajectory for different incidence angles between the background current and the discharge momentum.

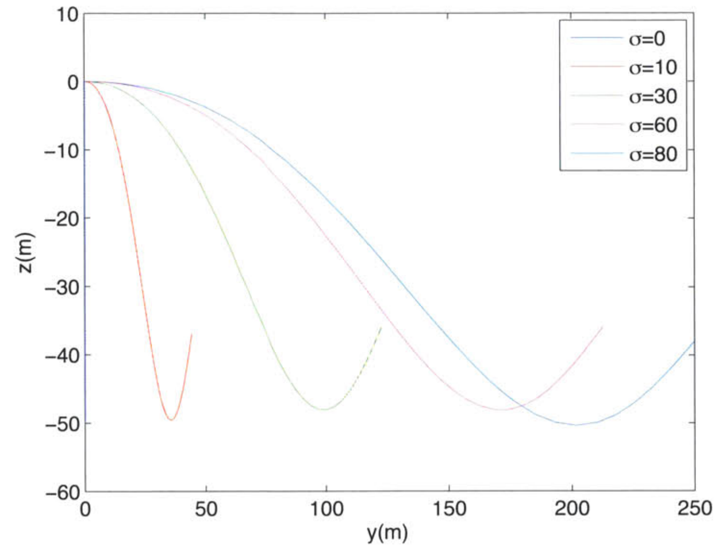

Figure 3.9 - Vertical view of the centerline trajectory for different incidence angles between the background current and the discharge momentum.

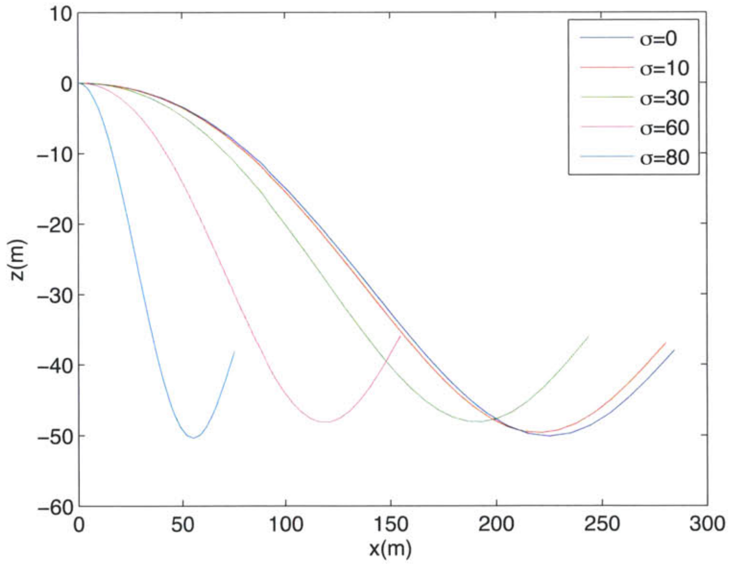

Figure 3.10 - Vertical view of the centerline trajectory for different incidence angles between the background current and the discharge momentum.

Figure 3.11 shows that the relation between the final volumetric dilution at the end of the near field and the angle of incidence of the ambient current is not monotonic. Figure 3.12 shows the same behavior between trap depth and the angle of incidence. However, the effect of the angle is not very large. For an ambient current of 0.1 m/s, dilutions are of order six for all the angles between 0 and 90 degrees, reaching a maximum at an angle of 47 degrees. The minimum dilution is reached for an incident angle of 90 degrees. The final trap depth exhibits a minimum at an angle of 47 degrees. The difference between the minimum and the maximum trap depth for angles between 0 and 90 degrees is only about three meters.

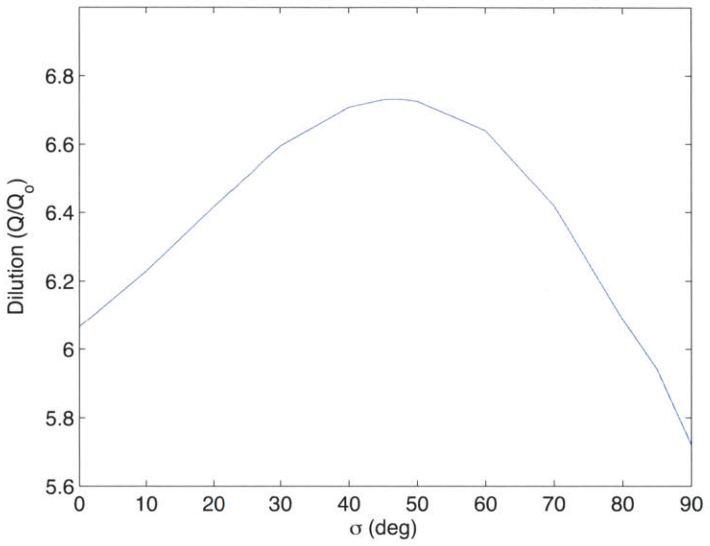

Figure 3.11 - Effect of crossflow angle on the volumetric dilution.

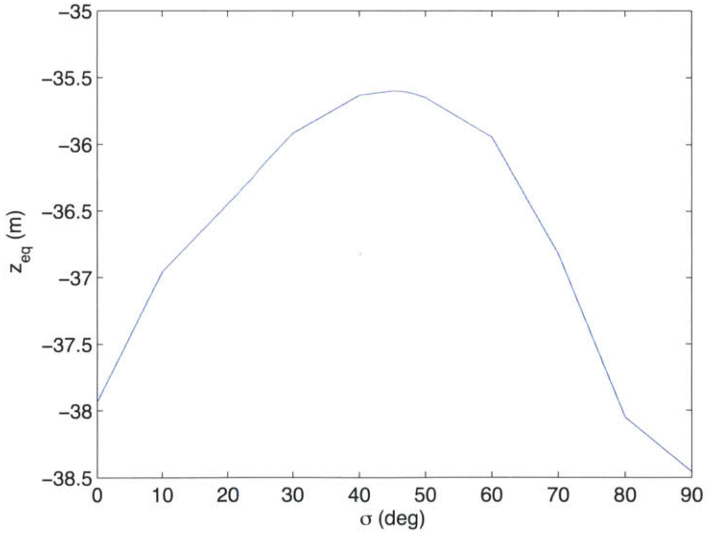

Figure 3.12 - Effect of crossflow angle on the terminal trapping level (measured from the discharge level).

3.4 Intermediate Field

The intermediate field is characterized by the vertical collapse and horizontal spreading of the plume. Figure 3.13 illustrates the plume collapse in the transition between the near and the intermediate field caused by the residual buoyancy forces. A general integral model is modified to account for the phenomenon of plume collapse in the intermediate field. These modifications provide more accurate simulations of OTEC plume behavior. The same considerations about ambient flow, turbulence, and earth rotation effects are made as in the near field model.

The plume reaches its neutrally buoyant depth at the end of the near field. Therefore the plume motion in the intermediate field corresponds to an internal density current. The excess velocity with respect to the ambient flow exhibits a Gaussian profile with different spreading rates in the vertical and horizontal directions due to ambient stratification. The centerline density excess, $\Delta\rho_c$, the buoyancy flux, B, and the jet angle with respect to the horizontal, θ, are zero in the intermediate field. The vertical position of the centerline, z, remains constant.

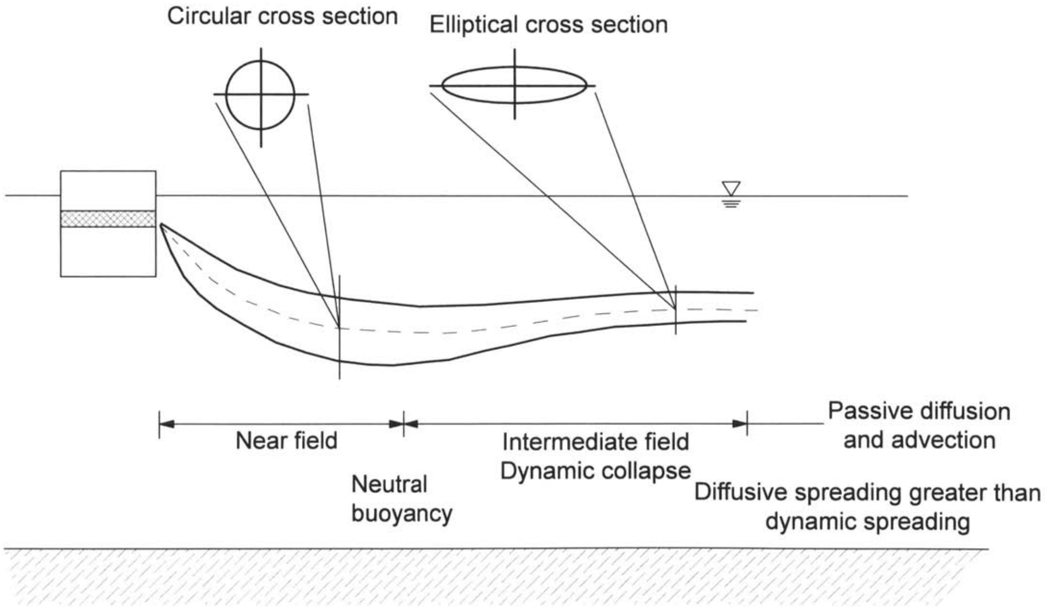

Figure 3.13 - Plume collapse effect in the transition from near field to intermediate field (adapted from Khondaker, 2000).

In addition, in the near field the plant discharges become (nearly) aligned with the ambient current, so for this study the angle between the background current and the jet velocity, σ, is considered to be zero and not included in all the following calculations.

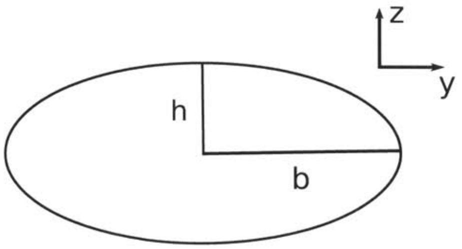

Figure 3.14 - Collapsed plume cross-section.

The velocity can be written in Cartesian coordinates as:

$$u(s, y, z) = u_c(s) e^{-\left(\frac{y}{b}\right)^2} e^{-\left(\frac{z}{h}\right)^2} + u_a$$

where z and y represent the vertical and horizontal coordinate respectively, and h and b represent the characteristic spreading length in vertical and horizontal directions respectively, as shown in Figure 3.14, and u_a represents the background current (assumed to be along the x-axis as in the near field model).

3.4.1 Integral Magnitudes

For the new velocity profile, the integral magnitudes are defined as:

- Volume flux

$$Q = \int_A u dA = \int_{-\infty}^{\infty} \int_{-\infty}^{\infty} \left(u_c e^{-\left(\frac{y}{b}\right)^2} e^{-\left(\frac{z}{h}\right)^2} + u_a \right) dz dx$$

$$Q = \pi b h (u_c + 2u_a)$$

In the definitions of the volume flux, Q, and the momentum flux, M, the background current does not yield bounded contributions. The integration limit on these two cases is defined by an ellipse of horizontal axis $\sqrt{2}b$ and vertical axis $\sqrt{2}h$ instead of infinity.

- Axial momentum flux

$$M = \int_A u^2 dA = \int_{-\infty}^{\infty}\int_{-\infty}^{\infty}\left(u_c e^{-\left(\frac{y}{b}\right)^2} e^{-\left(\frac{z}{h}\right)^2} + u_a\right)^2 dydz$$

$$M = \pi\frac{bh}{2}(u_c + 2u_a)^2$$

3.4.2 Conservation Equations

Analyzing a differential control volume, the fundamental principle of conservation is:

Horizontal momentum

$$\frac{dM}{ds} = Eu_a$$

where E represents the plume entrainment rate defined as:

$$E = 2bu_c\alpha e^{-5R_i} + 2hu_c\alpha$$

and the Richardson number is defined as:

$$R_i = \frac{\Delta\rho}{\rho_{ref}}\frac{gh}{{u_c}^2}$$

The term $\Delta\rho$ in the expression of R_i refers to a characteristic density difference, defined between the center of the layer and the ambient density at the extreme of the layer, and is calculated as:

$$\Delta\rho = \left|\frac{\partial\rho_a}{\partial z}\right| h$$

where $\frac{\partial \rho_a}{\partial z}$ represents the ambient density slope at the centerline of the layer, and ρ_{ref}, in the expression of R_i represents a characteristic density.

The entrainment into the plume is composed of two terms, the vertical and the horizontal, represented by the first and second terms respectively in the entrainment rate definition equation. The coefficient α corresponds to the jet entrainment coefficient determined experimentally in non-stratified ambient to be 0.055 (Jirka, 2004). The vertical entrainment term is reduced by the factor $\mathrm{e}^{-5\mathrm{R_i}}$ (Stolzenbach and Harleman, 1973) due to the stratification effect.

Furthermore, the geometry of the trajectory is defined by

$$\frac{dx}{ds} = 1$$

3.4.3 Buoyant Spreading

To solve the system of equations that govern the intermediate field numerically, another closure equation is required. Here, a spreading hypothesis is used. This approach is based on the experimentally observed relationship for a jet:

$$\frac{dr}{ds} = \epsilon$$

where r is the radius of the jet, s is the local coordinate along the centerline, and ϵ is the spreading rate. In the absence of ambient stratification, the spreading rate coefficient for a pure jet is twice the entrainment coefficient (Lee and Chu, 2003):

$$\frac{dr}{ds} = 2\alpha$$

In a stratified ambient, buoyancy forces induce a vertical thinning of the plume in addition to a horizontal spreading. The jet dynamics in the intermediate field are modeled as the superposition of two effects: the jet entrainment and the buoyant spreading. The plume-spreading process is assumed to behave as a density current, which entrains fluid at the edge of the plume while it spreads laterally at a velocity v_s (Jones et al. 1996). The spreading velocity is derived from a balance of the net pressure forces and the drag force acting on the front:

$$v_s = \sqrt{\frac{1}{6} g \left| \frac{\partial \rho_a}{\partial z} \right| \frac{1}{\rho_{ref}} \frac{1}{C_D} (2h)^2}$$

where C_D is the drag coefficient of the flow, which varies from 0.5 to 2.0 (Doneker and Jirka, 1990), and ρ_{ref} is a characteristic ambient density. This study assumes a value of 1.3 for C_D (Jirka, 2004).

The net spreading is modeled as the superposition of the two effects as follows:

$$\frac{db}{ds} = \frac{db}{ds}_{jet} + \frac{db}{ds}_{strat}$$

where the term $\frac{db}{ds}_{jet}$ represents the jet spreading rate, and the term $\frac{db}{ds}_{strat}$ represents the additional spreading due to collapse in the stratified ambient.

Along a streamline the spreading velocity v_s becomes:

$$v_s = (u_c + u_a) \frac{db}{ds}_{strat}$$

where u_c represents the jet centerline excess velocity and u_a represents the ambient current. Therefore the spreading rate due to the collapse effect can be computed as:

$$\frac{db}{ds}_{strat} = \frac{v_s}{u_c + u_a}$$

The resulting expression of the net horizontal spreading resulting from the fluid entrainment into the jet and the collapse is:

$$\frac{db}{ds} = \frac{db}{ds}_{jet} + \frac{v_s}{u_c + u_a}$$

The vertical spreading is reduced due to the plume collapse effect in such a way as to conserve the same cross section area of the layer during the collapse process.

The net vertical spreading rate is computed as:

$$\frac{dh}{ds} = \frac{dh}{ds}_{jet} - \frac{v_s}{(u_c + u_a)}\frac{h}{b}$$

where:

$$\frac{dh}{ds}_{jet} = 2\alpha$$

$$\frac{db}{ds}_{jet} = 2\alpha e^{-5R_i}$$

The entrainment coefficient α corresponds to a pure jet.

The resulting system of equations that govern the dynamics of the near field is:

$$1)\quad \frac{db}{ds} = 2\alpha e^{-5R_i} + \frac{v_s}{(u_c + u_a)}$$

$$2)\quad \frac{dh}{ds} = 2\alpha - \frac{v_s}{(u_c + u_a)}\frac{h}{b}$$

$$3)\quad \frac{d}{ds}\left(\pi\frac{bh}{2}(u_c + 2u_a)^2\right) = (2bu_c\alpha e^{-5R_i} + 2hu_c\alpha)u_a$$

$$4)\quad \frac{dx}{ds} = 1$$

These non-linear, coupled, differential equations allow one to solve for the four unknowns along the jet trajectory: b, h, u_c and x.

3.4.4 Solution Method

The above-coupled non-linear system of ordinary differential equations is solved using a fourth order Runge-Kutta method implemented in MATLAB. The magnitude of the volume flux, Q, momentum flux, M, and cross section center position, x, all at the end of the near field, are used as initial conditions for the numerical solution of the intermediate field. Additionally, at the beginning of the intermediate field, we assume that the jet width, b, equals the height, h.

The initial local variables can be obtained from the integral magnitudes by the following relations:

$$u_c = \frac{2M}{Q} - 2u_a$$

$$b = \left(\frac{Q}{\pi(u_c + 2u_a)}\right)^{1/2}$$

3.4.5 End of Intermediate Field

The end of the intermediate field is defined as the location where the centerline velocity approaches the ambient velocity. In this study, it was chosen as the location where the center of the jet reaches an excess velocity of 0.19 m/s.

3.4.6 Results

In this section we present the intermediate field characteristics of a 100-MW power plant, with warm and cold combined water discharge (400 m^3/s warm water intake and 320 m^3/s cold water intake) located 100 below the water surface. The ambient is assumed to be quiescent and stratified, and the initial discharge is assumed to be horizontal.

The fluid motion is neutrally buoyant since the plume has reached equilibrium at the end of the near field. The intermediate field has a horizontal extent of 800 m. The plume entrains fluid while it collapses. Figure 3.15 shows the evolution of the volume flux, half the width of the layer, half the vertical height of the layer, and the centerline velocity in the intermediate field. Figure 3.16 shows a cross-section of the velocity distribution at the end of the intermediate field. Figure 3.17 shows a top and a vertical view of the collapsed plume.

The width of the plume monotonically increases with the horizontal distance. However, the height of the plume cross-section decreases initially due to the collapse effect, but after a certain distance, it increases, evidencing that the entrainment surpasses the collapse effect. The final width of the plume is 1276 m. The final height of the plume is similar to the initial value, 80 m. The dilution achieved at the intermediate field is 3.8. The total average dilution achieved in the near and intermediate field is 20.5. The fluid takes 13.6 hours to reach the end of the intermediate field. This time is computed numerically as in the near field model.

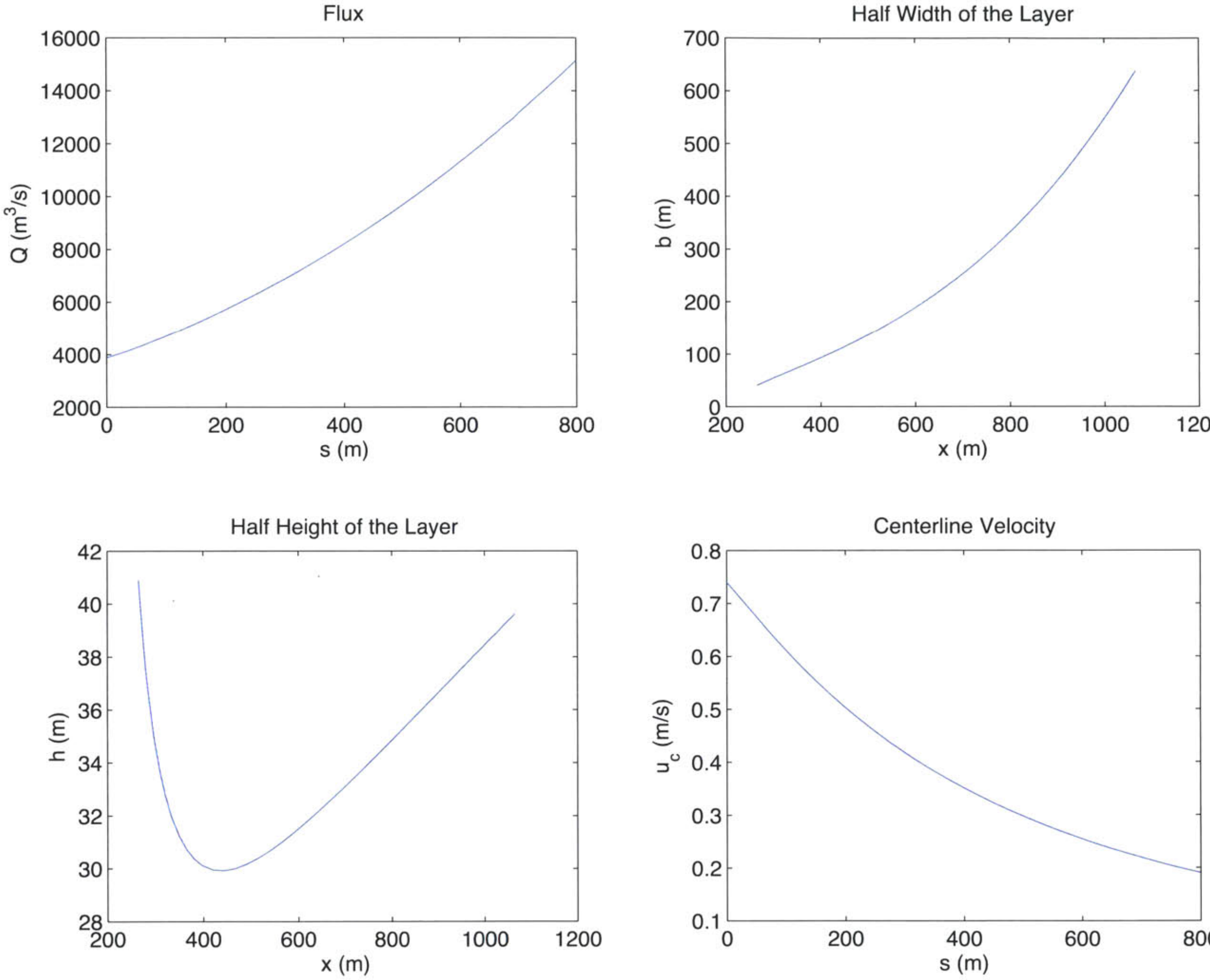

Figure 3.15 - Intermediate field plume characteristics for a 100-MW OTEC plant with combined discharge.

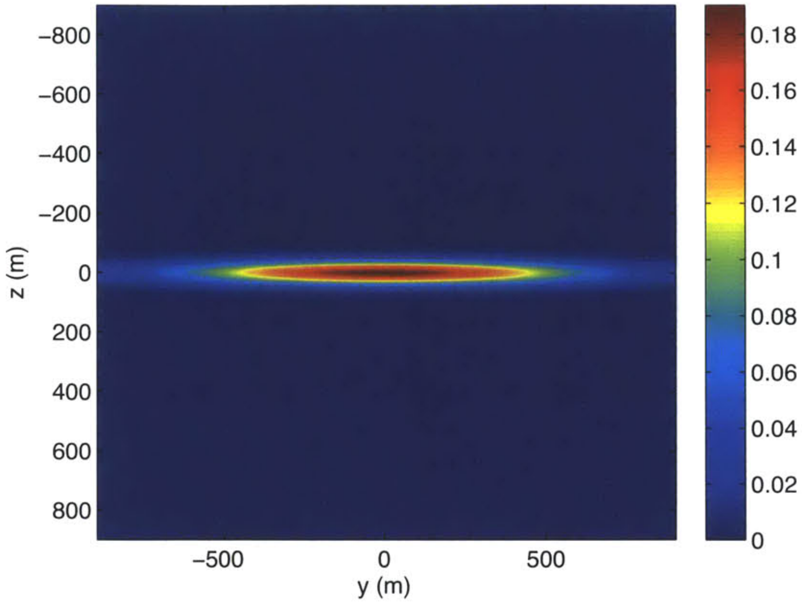

Figure 3.16 - Collapsed plume cross-section. Color scale indicates the velocity distribution in m/s, at the end of the intermediate field.

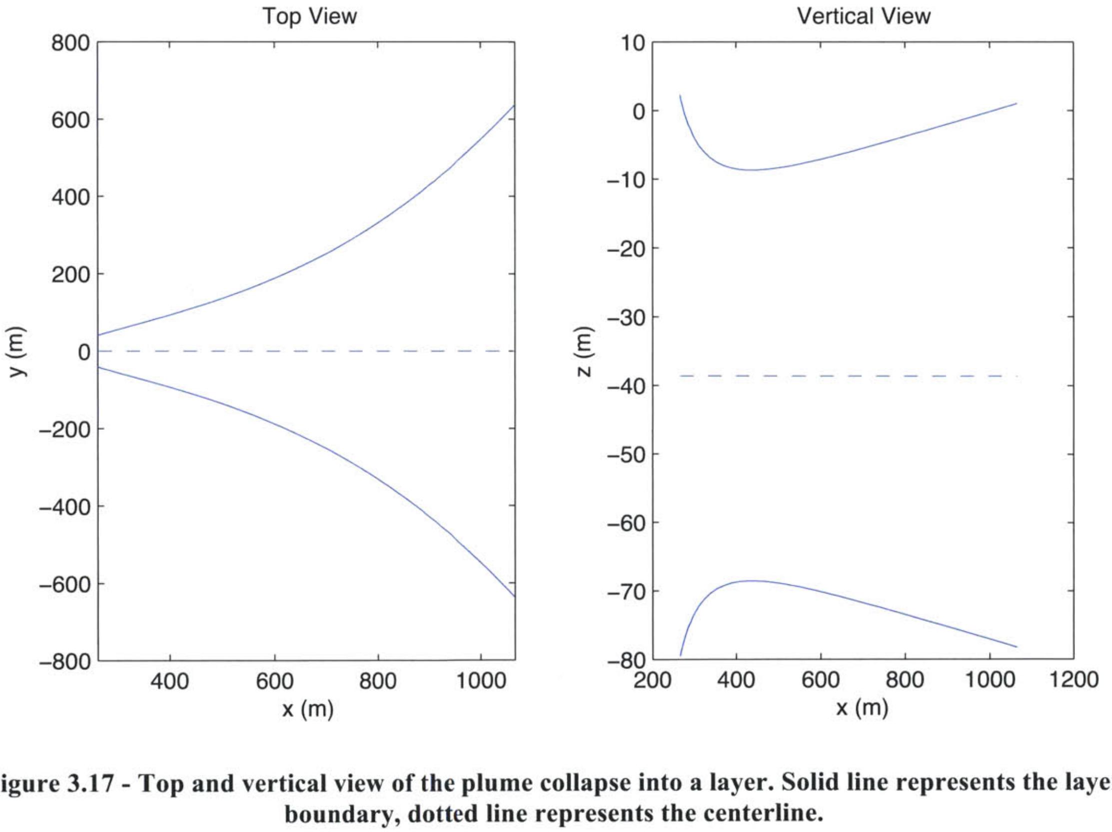

Figure 3.17 - Top and vertical view of the plume collapse into a layer. Solid line represents the layer boundary, dotted line represents the centerline.

3.5 Far Field Model

The simulations are performed using the numerical model MITgcm (MIT General Circulation Model), which has been used for applications in both the atmosphere and the ocean. The model can be used to study both atmospheric and oceanic phenomena with one hydrodynamic kernel (Adcroft et al., 2005), and it has a non-hydrostatic formulation allowing it to be used to study both small-scale and large-scale processes. Figure 3.18 illustrates applications of MITgcm on different scales.

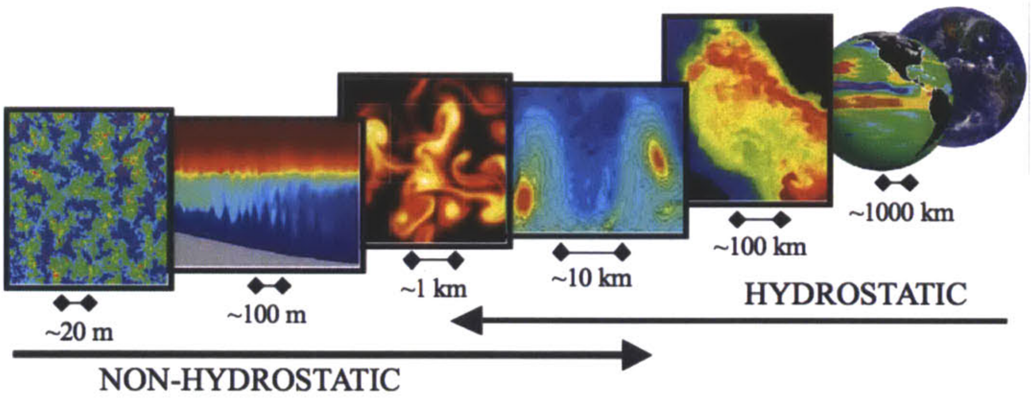

Figure 3.18 - Applications of MITgcm on different scales (Adcroft et al., 2005).

Non-hydrostatic ocean models solve the full incompressible Navier-Stokes equations, which is important to properly model the mixing OTEC plumes.

3.5.1 Governing Equations

The governing equations are:

1. Navier-Stokes equations of motion for an incompressible fluid

$$\frac{du}{dt} - fv + \frac{1}{\rho}\frac{\partial p'}{\partial x} - \nabla_h \cdot A_h \nabla_h u - \frac{\partial}{\partial z}\left(A_z \frac{\partial u}{\partial z}\right) = F_u$$

$$\frac{dv}{dt} + fu + \frac{1}{\rho}\frac{\partial p'}{\partial y} - \nabla_h \cdot A_h \nabla_h v - \frac{\partial}{\partial z}\left(A_z \frac{\partial v}{\partial z}\right) = F_v$$

$$\frac{dw}{dt} + g\frac{\rho'}{\rho} + \frac{1}{\rho}\frac{\partial p'}{\partial z} - \nabla_h \cdot A_h \nabla_h w - \frac{\partial}{\partial z}\left(A_z \frac{\partial w}{\partial z}\right) = F_w$$

2. Continuity

$$\frac{\partial u}{\partial x} + \frac{\partial v}{\partial y} + \frac{\partial w}{\partial z} = 0$$

3. Heat Balance

$$\frac{d\theta}{dt} - \nabla_h \cdot K_{hT} \nabla_h \theta - \frac{\partial}{\partial z}\left(K_{zT} \frac{\partial \theta}{\partial z}\right) = F_\theta$$

4. Salinity/Tracer Balance

$$\frac{dS}{dt} - \nabla_h \cdot K_{hS} \nabla_h S - \frac{\partial}{\partial z}\left(K_{zS} \frac{\partial S}{\partial z}\right) = F_S$$

5. Equation of state

$$\rho = \rho(S, \theta)$$

where x, y, z are the Cartesian coordinate system, $u, v, w,$ are the mean velocities components in x, y, z direction respectively, t is the time, p' is the water pressure, $K_{hT}, K_{zT}, K_{hS}, K_{zS}$ are the horizontal and vertical eddy diffusion coefficients for temperature and salinity respectively, A_h and A_z are the horizontal and vertical eddy viscosity coefficients, F_u, F_v and F_w are the momentum forcing terms in each direction, g is the acceleration due to gravity, ρ' is the water density, ρ is the reference water density, S is the salinity, θ is the temperature, and F_S and F_θ are the source and sink term for salinity and temperature respectively. The above equations, use the

Boussinesq approximation $\rho' = \rho + \rho''$, where ρ'' is small, and is ignored everywhere except in the gravitational forces. It means density variations are neglected in the momentum and mass conservation equation, except in buoyancy related terms.

3.5.2 Turbulence Model

A turbulent closure provides an expression for the eddy terms in the mass, heat, and momentum equations. In MITgcm, the turbulent transport terms of momentum are related to the gradient of the mean flow quantities (u, v, w) by the following closure:

$$\overline{u'v'} = A_h \left(\frac{\partial u}{\partial y} + \frac{\partial v}{\partial x} \right)$$

where A_h is the horizontal eddy viscosity coefficient. In this model, this coefficient can be given a value different from the vertical eddy viscosity coefficient, A_z. In MITgcm these two coefficients can be constant or variable.

Analogously, the turbulent transport terms of the concentration (governed by the salinity transport equation) are modeled as:

$$\overline{u'c'} = K_h \left(\frac{\partial c}{\partial x} \right)$$

where K_h is the horizontal eddy diffusion coefficient. MITgcm allows defining different coefficients for each direction (K_h and K_z). MITgcm uses different eddy diffusion coefficients for tracers and heat.

MITgcm allows using higher order viscosity and diffusion terms, but they were not used in this study, and are not included in the governing equations presented. It should be noted that the above formulas represent merely two terms of all the turbulent fluctuations terms involved in the Navier-Stokes and the transport equations. The remaining formulas for other turbulent terms can be extrapolated from these formulas.

3.5.3 Spatial Discretization

As shown in Figure 3.19, for Cartesian grids the model employs a conventional Arakawa C-grid and solves the governing equations by a finite volume approach. MITgcm treats the horizontal and vertical directions as separable, which is useful due to the importance of stratification in the vertical direction.

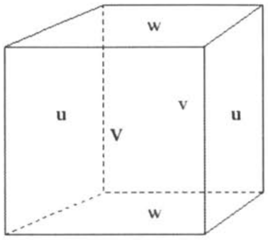

Figure 3.19 - Arakawa C-grid (Adcroft et al., 2005).

To compute the calculations, the domain is divided into tiles. These tiles are distributed over multiple processors. In this work, the MITgcm runs were performed on a 24-processor machine.

MITgcm allows uniform or variable grid size. For the simulations carried out a variable grid size was used. In order to assure numerical stability at the zone of OTEC discharge where the pumping flux is injected into the domain, a finer grid that coarsens further away from the mass source was used, as shown in Figure 3.20.

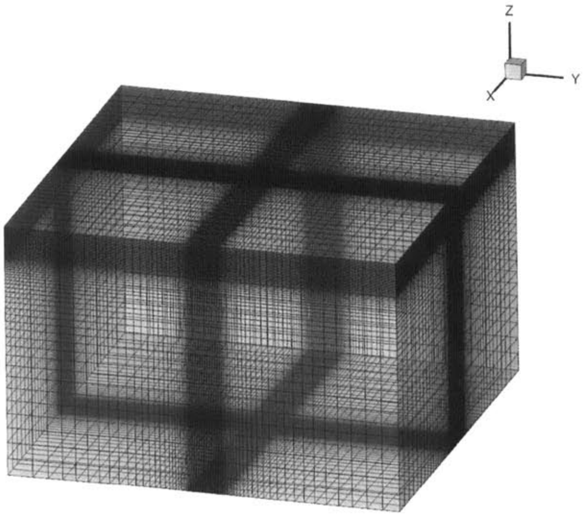

Figure 3.20 - Variable grid size mesh used in OTEC simulations.

3.5.4 Boundary Conditions

Different types of boundary conditions are available in MITgcm. For the free surface, the options are rigid lid or implicit free surface. An implicit free surface boundary condition was used in the simulations carried out. For solid boundaries, (bottom and walls), the conditions are either no slip or free slip. In the simulations carried out, periodic boundary conditions are used at the lateral boundaries of the domain, with a no slip condition at the ocean bottom.

3.5.5 Numerical Stability Criteria

MITgcm uses explicit and implicit methods to solve the model equations. For the explicit calculations it was necessary to use a time step that assures stability. The stability time conditions are based on the following dimensionless numbers:

1. Courant-Friedrichs-Lewy condition for advection

$$S_a = \frac{|\vec{u}|\delta t}{\Delta x}$$

2. Diffusion of momentum

$$S_l = 4\frac{A_z \delta t}{\Delta z^2}$$

$$S_l = 4\frac{A_h \delta t}{\Delta x^2}$$

3. Internal waves

$$S_c = \frac{c_g \delta t}{\Delta x}$$

$$c_g = NH$$

4. Inertial oscillations

$$S_i = f^2 \delta t^2$$

In general the above dimensionless numbers must remain smaller than order one to keep numerical stability.

Chapter 4 - Strategy of Coupling the Models

Since the grid sizes of the far field model are orders of magnitude larger than the characteristic length scales of the entrainment process of the near field, it is of interest to identify ways of coupling between the models.

In this thesis, two strategies are used to couple the models described in the previous chapter:

- *Brute Force Approach*
  In this approach a general circulation numerical model is used to compute the near, intermediate and far field mixing. This approach may require unrealistic adjustment of viscosity coefficients, diffusion coefficients, and grid size. This strategy is motivated by the work of Zhang and Adams (1999). They analyzed the prediction of near field plume characteristics using a far field circulation model ECOMsi (Blumberg and Mellor 1987) in application in Massachusetts Bay, and found that reasonable agreement could be obtained using judicious choice of grid size and model mixing (viscosity and diffusion) coefficients.

- *Distributed Sources and Sinks Approach*
  This approach is motivated by the work presented by Lee and Choi (2007) about the Distributed Entrainment Sink Approach for modeling mixing and transport in the intermediate field. This method proposes an integral model to solve the near and the intermediate field mixing, and uses a general circulation model to compute the far field dynamics. For this study it is concluded that this method is better than the first one.

4.1 "Brute Force" Approach

The objective of this section is to study and determine the accuracy and limitations of MITgcm to solve the process of plume entrainment in a stratified ambient. Mixing mechanisms involve highly complex turbulent structures, developed over milliseconds to hours and in millimeter to hundred meters length, difficult to model. Different numerical models are more accurate than others in simulating the entrainment into a plume. Studying the model sensitivity is an important initial step since it can save time in running demanding non-hydrostatic simulations. This section explores the dependence of plume entrainment and mixing with ambient fluid on model resolution and other model parameters. The model resolution requires a compromise between accuracy and fast computation. To model the plume entrainment processes with relative accuracy using MITgcm, it is necessary to employ a very small grid size, making this testing stage very expensive and time consuming. Of particular importance is the vertical discretization of the domain.

4.1.1 Setup

We studied the discharge of a negatively buoyant fluid into a quiescent and linearly stratified one. Salinity is kept uniform within the domain. Density stratification is due to temperature stratification. The discharged fluid has the same salinity as the environment. A linear equation of state for density is assumed and no earth rotation is considered. Figure 4.1 shows the modeled domain, the ambient stratification used, and the location of the fluid source.

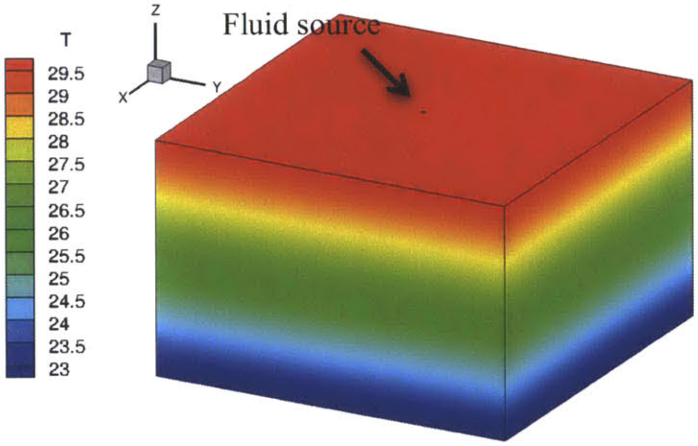

Figure 4.1 - Modeled domain showing the thermal stratification of the fluid and the source location.

For the adjustment of the model parameters, a mixed OTEC discharge is considered. Typical temperature differences between an OTEC discharge and the environment water at the discharge level are of the order of 4°C for the combined exhaust case. For the model calibration, we considered volume flux, Q_o, and buoyancy flux, B_o, within the range of the values corresponding to 10 MW-100 MW plants and configurations with one to four discharges. For a 10-MW plant, each of the four plumes has values of 0.14 m^4/s^3 and 18 m^3/s for buoyancy flux and volume flux respectively. For a 100-MW plant, considering one single discharge, the former is 5.8 m^4/s^3 and the latter is 720 m^3/s.

A passive tracer is used to distinguish the discharged water from the ambient fluid. Its concentration is defined as unity in the discharged water and zero in the ambient fluid. The tracer concentration allows us to illustrate the plume mixing with the ambient water and to identify the boundary of the plume, which we define by a surface of concentration 0.01, as shown in Figure 4.2.

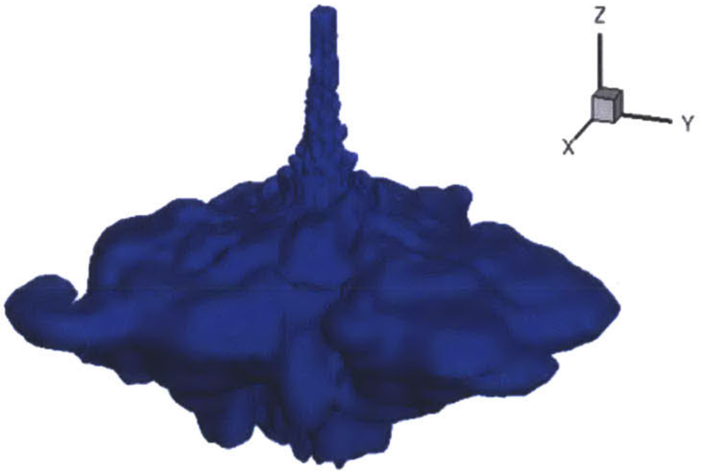

Figure 4.2 - Numerical modeled plume defined by a surface of tracer concentration 0.01.

In all the simulations, we observed that as the discharged fluid (denser) descends it entrains ambient fluid, diluting the tracer concentration, until the plume reaches the neutrally buoyant depth.

4.1.2 Plume Trapping

In a linear stratified ambient, Briggs (1969) predicts the trap depth h_t of a plume, indicated in Figure 4.3, in terms of the initial buoyancy flux at the source, B_o, and the stratification frequency of the ambient, N, as follows:

$$h_t = \frac{3.8B_o{}^{1/4}}{N^{3/4}}$$

where

$$B_o = \frac{Q_o g \Delta\rho_o}{\rho}$$

$$N^2 = \left|\frac{g}{\rho}\frac{\partial\rho}{\partial z}\right|$$

Assuming density depends only on temperature and varies linearly with it, the buoyancy flux and the stratification frequency can be expressed as:

$$B_o = Q_o g\alpha\Delta T_o$$

$$N^2 = g\alpha\frac{\partial T}{\partial z}$$

where α is the water thermal expansion coefficient, assumed $2\text{x}10^{-4}$°K^{-1}, and ΔT_o is the discharge excess temperature.

The minimum plume dilution at the trap depth is computed as (Fischer et al. 1979):

$$S_m = \frac{0.9B_o{}^{3/4}}{Q_o N^{5/4}}$$

We considered two volume fluxes with their corresponding initial buoyancy flux within the range of the OTEC sizes considered. Table 4.1 presents the value of trap depth, h_t, and the minimum plume dilution at the trap depth, S_m. In all the simulations the ambient stratification was kept constant with stratification frequency N=$4.8\text{x}10^{-3}$ s^{-1}. The initial temperature difference between the environment and the released fluid is 9˚C.

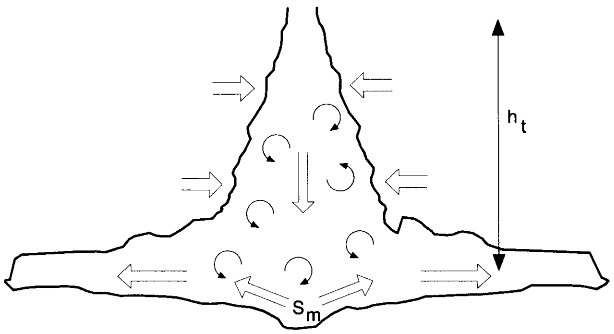

Figure 4.3 - Plume trap depth (h_t) definition.

Table 4.1 - Trap depth (h_t) and dilution (S_m) for the tested cases.

Q (m^3/s)	B (m^4/s^3)	h_t (m)	S_m
20	0.35	161.1	16.4
200	3.53	286.5	9.22

4.1.2.1 Model Parameters to Control the Trap Depth

The model parameters to control the trap depth are:

1. *Grid resolution*

2. *Eddy viscosity coefficient*

   This refers to the turbulent diffusion of momentum coefficient. Higher viscosity implies higher momentum diffusion.

3. *Eddy diffusion coefficient*

   MITgcm uses different coefficients for the tracer and for heat. For the temperature, in order to preserve the background stratification, we set the explicit diffusion coefficient to zero.

The model also requires defining an *Advection scheme* and a *Time step*. In all the simulations carried out, a non-linear advection scheme is used for temperature and tracer, which introduces some diffusion in the solution. For the volume rates considered, the plume length scale is estimated as a few hundred meters guiding the choice of grid resolution. This limits the time step that can be taken. The time step is chosen to make the model stable.

4.1.3 Computational Domain and Model Resolution

A square domain of horizontal length about $6.5h_t$, and depth about $4.5h_t$, is used to capture the sinking of the plume until it reaches its equilibrium level. The domain was discretized using orthogonal grids. Horizontal and vertical domain lengths are chosen to be long enough such that the boundaries do not interfere with the mixing. The plume mixing is mainly achieved within a volume whose depth is of order h_t. For this reason, and in order to reduce the computational cost as much as possible, we adopted uniform resolution within a central region of horizontal length of about $1.3h_t$, and a vertical depth of about $1.1h_t$. Outside this region, the grid size expands smoothly following a power law. The grid size expansion is chosen to make the code stable and to reduce significantly the computational cost of each simulation.

For each volume flux, simulations are carried out at three different resolutions, with the minimum grid size for each: 2, 6 and 12 meters for a volume flux of 20 m^3/s, and 6, 12 and 24 meters for a volume flux of 200 m^3/s. For each resolution, model parameters are adjusted so that the neutrally buoyant depth is in agreement with the analytical results. This matching between parameters and resolutions can be used for later simulations of OTEC external flows.

The grid size constitutes a critical parameter in numerical simulations. The model stability is very sensitive to the grid resolution particularly near the discharge zone, which is the zone featuring the largest velocities. Relatively large or intermediate grid sizes do not produce accurate numerical mixing and the numerical solution presents significant noise. In the scope of this work a large number of simulations had to be carried out in order to find a grid size yielding a stable solution within an affordable simulation time, which also results in accordance to analytical predictions.

This testing stage is computationally very demanding since the grid size and the time step required are very small. With the available computational resources it is extremely expensive to run non-hydrostatic simulations for a highly resolved model using uniform resolution in the vertical and horizontal direction for all the cases analyzed.

Table 4.2 shows the dimensions of the computational domain used in the simulations. For the volume rate of 20 m^3/s, a grid size of 2 m, and the largest eddy viscosity (10^{-1} m^2/s), the dimensions of the domain had to be increased (2000 m in height and in horizontal extent) so the boundaries do not interfere with the mixing.

Table 4.2 - Computational domain dimensions.

Q (m^3/s)	$L_x = L_y$ (m)	L_z (m)
20	1000	650
200	2028	1350

For numerical stability, larger source sizes are required for larger fluxes (more grids to distribute the flux). Table 4.3 shows the source dimension for each case analyzed.

Table 4.3 - Source lengths used.

Q (m^3/s)	Source length (m)
20	12
200	24

4.1.4 Numerical Trap Depth

The trap depth definition is somewhat arbitrary. We defined it as the middle depth between the location of the upper and bottom contours of concentration 0.01 along the centerline plane measured at 200 meters from the source. Figure 4.4 shows the plume boundary from which the trap depth can be computed.

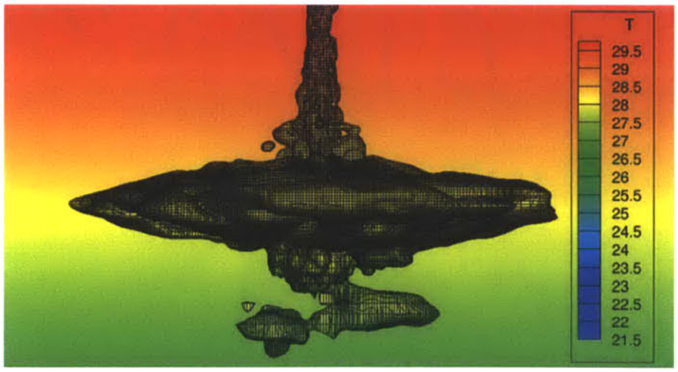

Figure 4.4 - Vertical view of the plume boundary from which the trap depth can be computed.

4.1.5 Effect of Eddy Viscosity on Trap Depth

Simulations are carried out using four different values of eddy viscosity, 10^{-1}, 10^{-2}, 10^{-3} and 10^{-4} m^2/s. Isotropic turbulent viscosity is assumed. For all the simulations carried out the explicit diffusion coefficients are set to zero. Figure 4.5 shows the dependence of trap depth on eddy viscosity for different grid sizes for two volume fluxes.

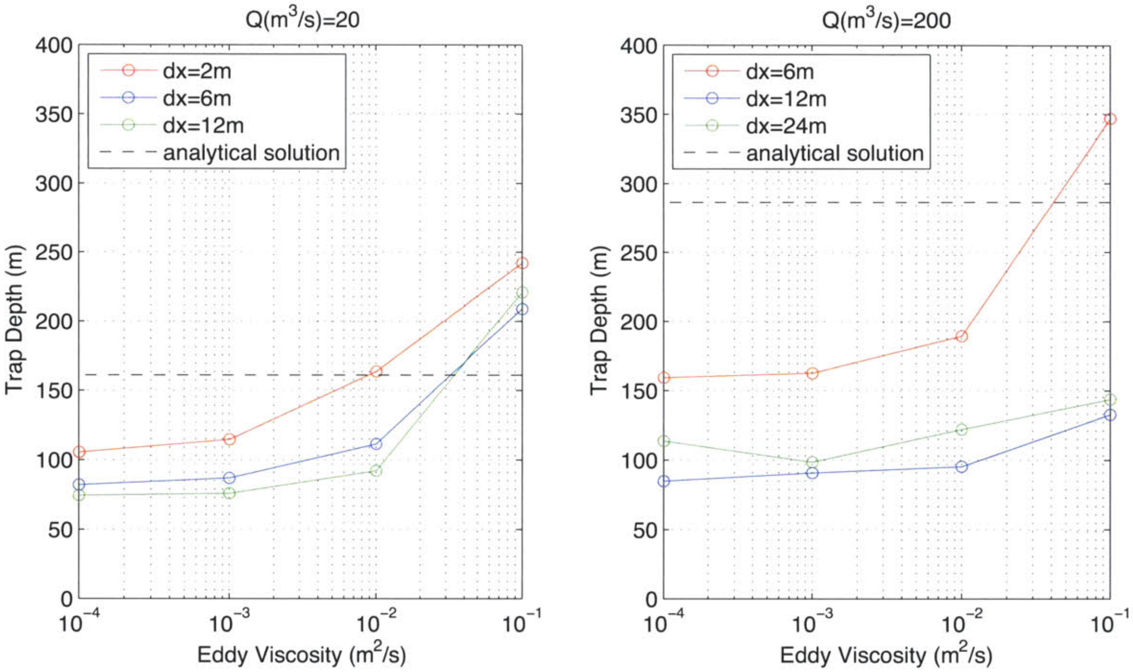

Figure 4.5 - Effect of eddy viscosity on plume trap depth for different model resolutions (dx indicates the grid size).

The eddy viscosity is model resolution dependent. For the two cases shown in Figure 4.5, for each resolution, trap depth increases when the eddy viscosity increases, with the exception of one data point. This exception is very small and can be attributed to a misshapen plume due to a large grid size.

In Figure 4.5, for the small volume flux case, there is a general trend that for a given viscosity, trap depth decreases as grid size increases. This behavior is not fully observed for the large flux case, where there is no monotonic trend. The trap depth obtained using a resolution of 12 m is smaller than that obtained using a resolution of 24 m. This might be explained by the arbitrary definition of the trap depth used and the unrealistic misshapen plume produced for large grid sizes. In the large flux case, coarser grids produce a plume with more fluid in the center, overshooting the level at which the plume spreads. The value of the trap depth is affected by this. As this occurs mainly at the center of the plume, for the coarser case, we measured the trap depth at 600 meters from the center of the discharge. Even then, the trap depth obtained using a grid size of 24 m is slightly larger than that obtained using a grid size of 12 m. For the range of viscosities considered, both grid sizes, 12 and 24 m, underpredict the trap depth. Clearly, coarse resolutions are inadequate when modeling large flux plumes.

For small fluxes, the model can reproduce the predicted trap depth (~161 m) by selecting an appropriate turbulent viscosity coefficient for all the grid sizes tested. For large volume fluxes, only the smallest grid size leads to a correct value of plume depth (~286 m) for the viscosity range considered. For the cases of grid sizes of 12 and 24 m with a flow rate of 200 m^3/s, the trend in the plot suggests that much larger viscosities are needed. However, viscosities larger than 10^{-1} m^2/s increase the computational time of the simulation beyond affordable limits, and represent unrealistic conditions. This renders this method unusable for OTEC sized plants, where the discharged volume fluxes are large.

Based on the results for small and large volume rates, we concluded that a grid size of 6 meters can be considered acceptable since it represents an effective tradeoff between accuracy, using the corresponding eddy viscosity, and computational cost. Grid sizes of 12 and 24 meters yield unrealistic results, particularly for the large volume rate, as the plume discretization is too coarse.

The results are very sensitive to the grid size and therefore have not converged to a consistent answer (the reality). This suggests that in order to model the plume entrainment process, - and hence, the plume trap depth - in accordance with the reality, very fine grid sizes are needed. However, this is only possible on a machine much more powerful than the one used in this thesis, and is in general a severe limitation of the *Brute Force* method.

4.1.6 Effect of Resolution and Eddy Viscosity on Plume Shape

Large grid sizes lead to unrealistic plume shapes. A model resolution of 2 meters or smaller is ideal. For a coarse case, the fluid discharge is distributed among fewer grid cells, or even into only one grid cell for the less resolved runs. Having a large volume flux located at one single grid cell might contribute to the unrealistic plume shape identified in the 24 m case. Thus it is recommended to spread the source over several grid cells. In addition, for large grid cells, the model does not resolve smaller eddy structures and the plume displays relatively large bumps in its surface. For finer grids, the plume shape displays ripples since smaller scale structures are better resolved.

For small eddy viscosities, the model tends to align the spreading of the fluid along the model x and y-axes, and this influences the resulting asymmetric shape of the plume. When examining the shape of the plume, we note that the tracer advection scheme employed introduces enough diffusion. Accordingly, setting the explicit coefficients to zero seems to be a reasonable assumption. In large viscosity simulations, the plume boundary does not exhibit eddy structures, since the shear that drives the mixing is limited. The highly viscous fluid sinks, remaining almost unmixed with the ambient fluid until reaching the depth where the ambient density is similar to the original fluid discharge density.

Figures 4.7 and 4.8 present the plumes for different eddy viscosities and grid sizes, for a small and large volume flux respectively, at the moment when the plume reaches its trap depth.

4.1.7 Effect of Eddy Diffusion on Plume Trap Depth and Plume Shape

We studied the effect of eddy diffusion on the plume trap depth by considering values of horizontal and vertical eddy diffusion ranging from zero up to the eddy viscosity coefficient. As both parameters are governed by turbulence, it is a reasonable assumption to set the maximum value of the eddy diffusion coefficient equal to the eddy viscosity coefficient.

The effect of increasing the diffusion coefficient is to wipe out any ripple or irregularity of the plume boundary. No significant changes in the plume trap depth can be observed. We performed several simulations increasing the diffusion coefficient five orders of magnitude (from 10^{-7} to 10^{-2} m^2/s) and the change in the magnitude of the trap depth is of the order of 1% (Figure 4.6).

For the largest viscosity cases, in which the eddy viscosity coefficients in vertical and horizontal directions are 10^{-1} m^2/s, setting the diffusion coefficient equal to the viscosity introduces excessive diffusion and the plume shape does not look real. The numerical solution resembles more a diffusive source than a sinking plume. This corroborates the assumption of setting the explicit diffusion coefficient to zero.

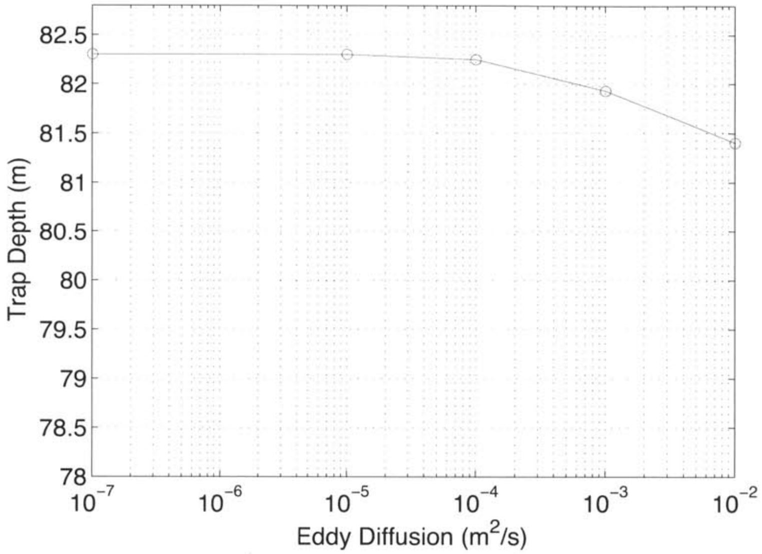

Figure 4.6 - Effect of eddy diffusion on trap depth, for Q=20 m^3/s, grid size 6 m, and eddy viscosity 10^{-2} m^2/s.

4.1.8 Conclusions

We concluded that it is not easy to satisfactorily reproduce numerically the correct entrainment. The results are very sensitive to the grid size. For very coarse grids, the model generates excessive mixing and the plume reaches smaller neutral buoyant depths. The plume is poorly resolved. In order to model the plume entrainment process, and therefore the plume trap depth, in agreement with reality, very fine grid meshes are needed. This represents a significant limitation of the application of the *Brute Force* method to OTEC discharges characterized by large volume rates.

In contrast to the conclusions of the work by Zhang and Adams (1999), who were able to artificially adjust far field model parameters to correctly predict near field plume characteristics for a marine waste water discharge, with MITgcm it was found that it is not always possible to adjust model parameters to obtain results in agreement with theoretical predictions when applied to OTEC discharges characterized by large volume flux.

Zhang and Adams performed their study for smaller volume fluxes (3 m^3/s to 9 m^3/s), and larger buoyancy fluxes (discharge density difference of about 3%), compared to the values used in this study (volume fluxes of 20 and 200 m^3/s and density difference of 0.18 %). Hence momentum was less important for them. Moreover, they were able to use much larger horizontal grid sizes, and therefore fewer grids. The difference in model response here, when compared to their study, can be explained by the fact that the relatively large fluid discharges, and yet moderate buoyancy fluxes, of an OTEC plant discharge are harder to model accurately than the smaller wastewater treatment of plant plumes.

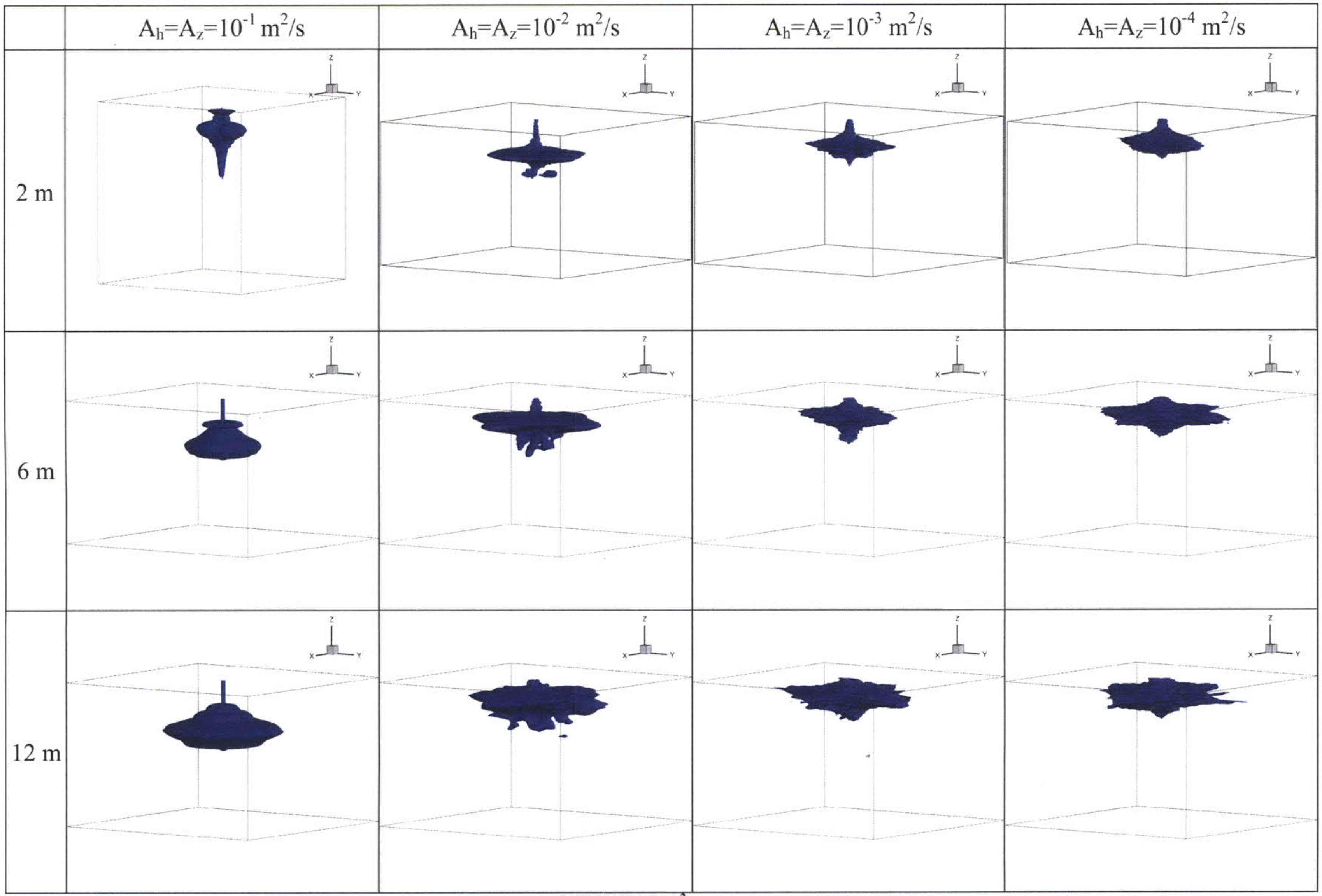

Figure 4.7 - Plumes for different grid sizes and eddy viscosities for Q=20 m^3/s (A_h and A_z are the horizontal and vertical eddy viscosity coefficients respectively).

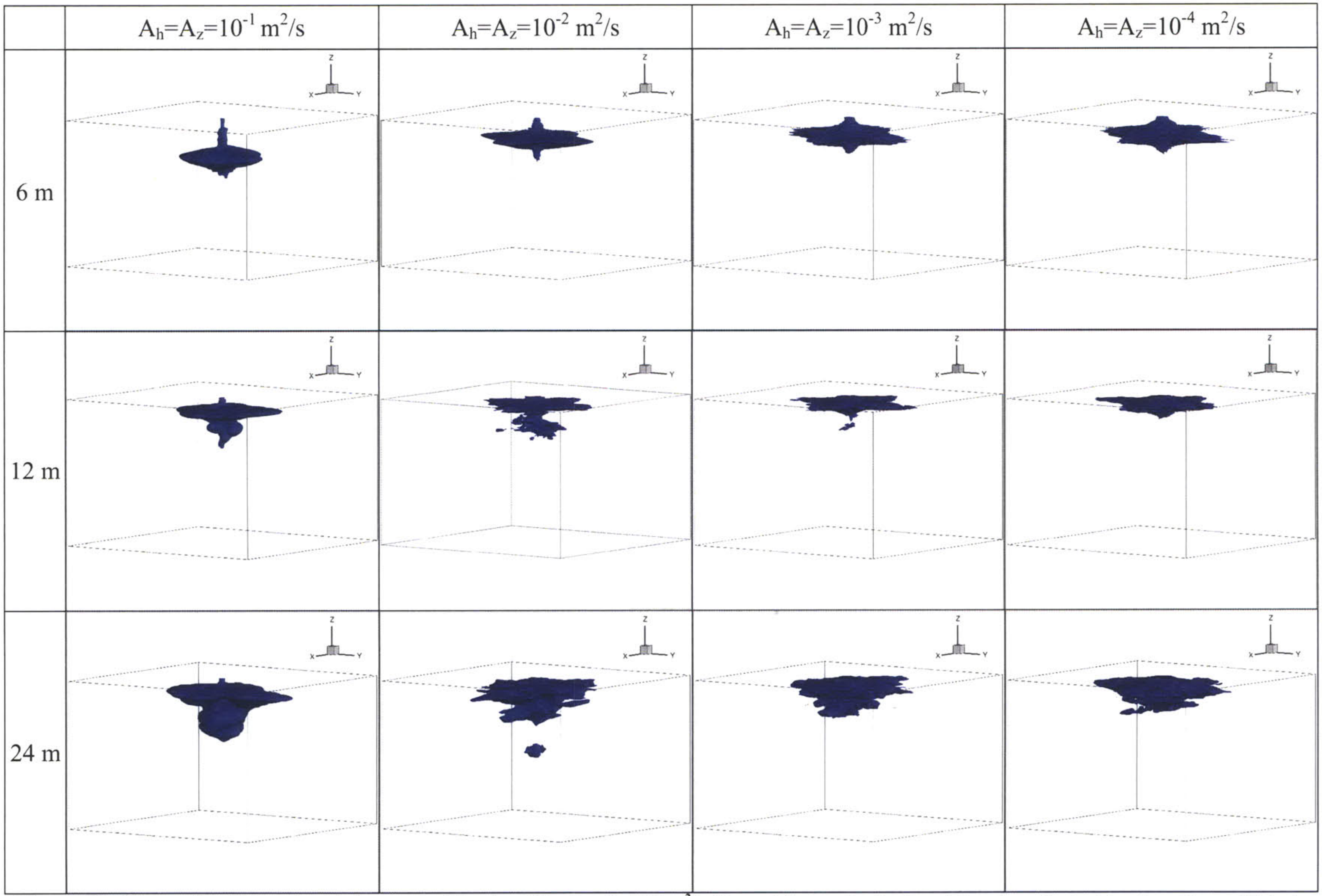

Figure 4.8 - Plumes for different grid sizes and eddy viscosities for Q=200 m^3/s (A_h and A_z are the horizontal and vertical eddy viscosity coefficients respectively).

4.1.9 Application to Real OTEC Scenarios

MITgcm is frequently applied to model ocean flows using the hydrostatic version since the horizontal scales involved are much larger than the vertical ones making the vertical acceleration terms negligible. The main difference between an OTEC model and other MITgcm applications is the need for inclusion of sources and sinks of mass into the fluid domain. The original MITgcm source code was modified to implement OTEC warm and cold water intakes and warm and cold water exhausts into the computational domain. OTEC intakes are represented by sinks, and OTEC discharges are represented by sources of mass. This way, water is added at the outflow depth and is removed from the intake depths as schematized in Figure 4.9.

MITgcm has a built in option, which allows including mass sources and mass sinks into the domain. In an input file created for the particular OTEC model, the locations and strengths of mass inflows and outflows are defined. The code modifications implemented account for the heat, salinity and momentum changes in the grid cells affected by OTEC outflows. New variables were defined for the temperature and concentration of the outflow. The modeled OTEC power plant draws in water from places where it has defined negative source mass, and expels water at places where source mass is positive, ensuring that heat and salt are conserved in the process. The code implemented assumes that the heat exchange in the condenser and evaporator is negligible and not considered in the outflow temperature.

For the OTEC plant size range studied, the source is distributed along several grids in a horizontal plane to keep numerical stability. As the fluid sinks or rises depending on the initial buoyancy, it was not necessary to extend the source or the sink in the vertical direction for numerical stability. It was necessary to use larger source lengths as the volume flux increase, to spread the flux over larger area.

The following sections present several tests that were performed to better understand how MITgcm represents an OTEC discharge.

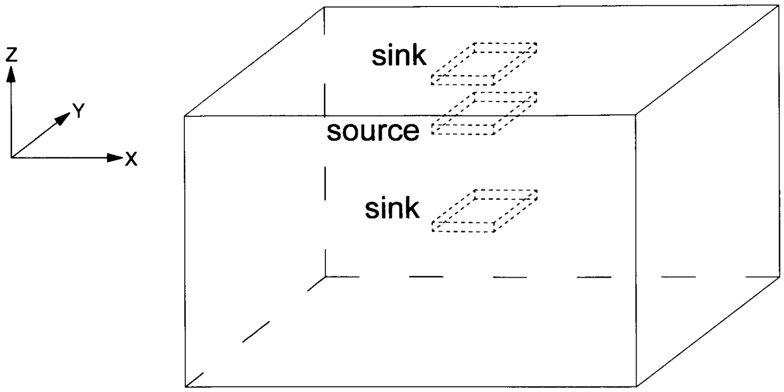

Figure 4.9 - OTEC plant representation into MITgcm for the combined exhaust discharge.

4.1.9.1 Comparison of MITgcm and Integral model

In this section we compared the plume trap depth predicted by an integral model, detailed in the near field section, and that computed by MITgcm. The aim of this comparison is to be able to assess weather MITgcm can predict similar results to the integral model.

For this comparison, in the integral model we considered a horizontal discharge and a discharge inclined 45° below the horizontal. For this model, the trap depth is defined in two different ways as the:

- First depth where the plume has the same density as the ambient (denoted “no overshoot”)
- Second depth where the plume shows no density difference with the ambient (denoted “with overshoot”)

For both MITgcm simulations and integral model calculations, we assumed a temperature profile shown in Figure 2.4, and a combined effluent discharge at a temperature 17.4 °C. Figure 4.10 shows the trap depth as a function of the volume flux for both the integral model and MITgcm. The MITgcm simulations carried out assume an eddy viscosity of 10^{-2} m^2/s and a grid size of 6 m.

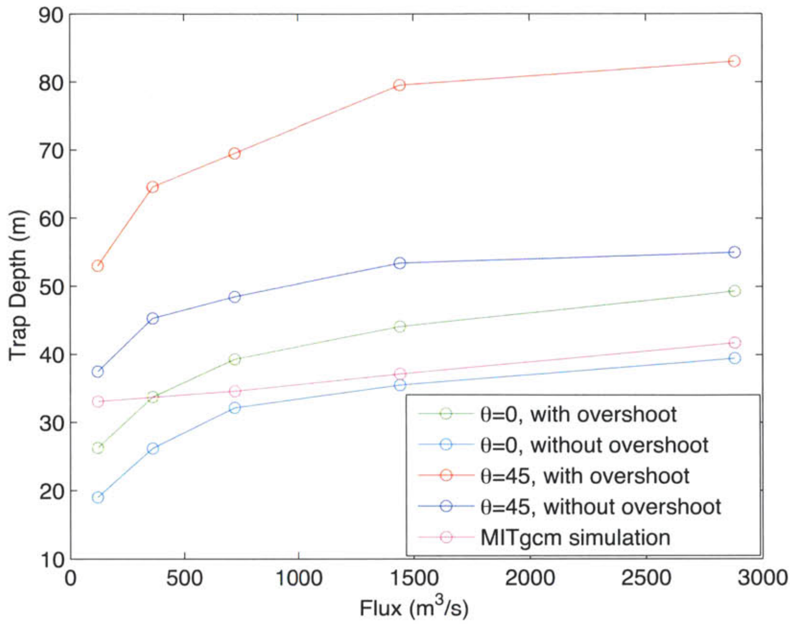

Figure 4.10 - Comparison of trap depth computed by the integral model and MITgcm for different OTEC plant sizes (θ is the angle measured from the horizontal).

The downward-inclined discharge reaches higher trap depth, showing that the initial momentum is of significant importance in the terminal trap depth. The final equilibrium depth is larger than the depth of the first point of no density difference between the plume and the ambient due to the vertical momentum that causes overshoot and leads to additional mixing.

As with the earlier analysis of a negatively buoyant source in a linear stratified ambient, MITgcm underpredicts the trap depth for the majority of the flux ranges considered. Only for small fluxes does the trap depth predicted by MITgcm fall between the ones predicted for horizontal and inclined discharges. The trapping depth predicted by MITgcm presents a nearly linear behavior with the volume flux discharged, which differs from the behavior observed with the integral model. This motivated the addition of momentum terms at the fluid source in the original MITgcm code in order to improve the accuracy in predicting the trap depth.

4.1.9.2 Length Scales

It is useful to define several length scales to analyze buoyant jets:

1. *Discharge Length Scale*

The discharge length, L_Q, compares the volume flux with the momentum flux.

$$L_Q = \frac{Q_o}{M_o^{1/2}}$$

where Q_o is the initial flow rate, and M_o is the initial momentum flux. In this study L_Q is important only for the comparison to the jet-to-plume length scale.

2. *Jet-to-Plume Length Scale*

   The jet-to-plume length scale, L_M, compares the initial momentum flux with initial buoyancy flux.

$$L_M = \frac{M_o^{3/4}}{B_o^{1/2}}$$

   This length separates the initial region where momentum dominates the jet behavior, and the region where buoyancy starts to control the dynamics of the jet.

From the ratio of both magnitudes, one can assess the relative importance of momentum and buoyancy. For OTEC discharges, considering the typical ambient temperature of 21.5°C and the effluent temperature discharge of 17.4°C (a temperature difference of 4.1°C), the magnitudes of these characteristic lengths scales are shown in Table 4.4.

Table 4.4 - Length scales comparison for different OTEC fluxes.

Power (MW)	Q_{total} (m^3/s)	u_o (m/s)	M_o (m^4/s)	B_o (m^4/s)	L_Q (m)	L_M (m)	L_M/L_Q
10	72	2	144	0.6	6.0	54.9	9.2
100	720	2	1440	5.7	19.0	97.7	5.1
400	2,880	2	5,760	22.9	37.9	138.1	3.6

By comparing the magnitudes of L_M to L_Q we note that the initial discharge momentum is of significant importance. MITgcm source code considers the sources of mass as buoyancy sources, and it does not account for momentum terms in the sources of mass. This characteristic of the numerical model is thus not ideally suitable to model OTEC discharges where it is expected that the momentum terms play a significant role in the plume dynamics. For this reason, including the momentum at the mass source into MITgcm calculations would represent a good improvement of OTEC plume modeling.

4.1.10 Momentum Implementation in MITgcm Source Code

To date, there is no record of the inclusion of momentum terms at the source of mass to have been implemented into MITgcm. The original Fortran codes were modified to include discharge momentum (and the following qualitative conclusions were made) for the calculations of:

1. *Horizontal Momentum*

   The code modifications implemented do not perfectly reproduce the physics of the discharge. The discharged fluid flows via the imposed momentum discharge, but some return near the source flow is observed at the initial times.

2. *Vertical Momentum*

   Contrary to what was anticipated, it was observed that the addition of the vertical momentum in the discharge reduces the plume trap level. This might be explained by the initial downward momentum enhancing the entrainment from the levels above the source; consequently, the relatively colder discharged fluid mixes with warmer fluid. The resulting plume reaches neutral buoyancy at shallower depth. By looking at the tracer concentrations, it can be seen that the plume is more diluted. This explains why the plume traps at a shallower level.

Unfortunately there are no other applications of sources of mass with momentum terms to compare results, so as to be able to evaluate if the code modifications were completely accurate. In further simulations, momentum terms are not included in the code.

4.1.11 Sensitivity of Trap Depth to Initial Buoyancy

We analyzed the dependency of the trap depth of the plume computed by MITgcm on the initial temperature difference between the ambient and the effluent in a typical stratified ambient. The flux, the discharge depth, and the source length are kept constant. Figure 4.11 shows the results computed for a 17-MW power plant, a discharge volume flux of 53.3 m^3/s, located at 99 m below the water surface, and a source length of 60 m. The behavior differs from the one observed in a linear stratified ambient where the relationship between the trap depth and the temperature difference follows a power law of coefficient 1/4. For the ambient temperature profile considered (Figure 2.4), MITgcm numerical results follow a power law of coefficient 0.57.

4.1.12 Temperature of the Source as Function of the Initial Buoyancy

For the same discharge characteristics, we analyzed the dependency of the temperature at a grid cell corresponding to the source with the initial temperature of the discharged fluid. The resulting temperature at the source grid differs from the temperature of the released fluid. For each model grid, MITgcm computes the mixing and the heat balance from all the inflows and outflows. The mixing of the injected fluid with the surrounding ambient at the cells corresponding to the source causes the temperature difference between the discharged fluid and the source. Figure 4.12 shows the resulting temperature at the source as a function of the temperature difference between the ambient and the discharge. The behavior is nearly linear.

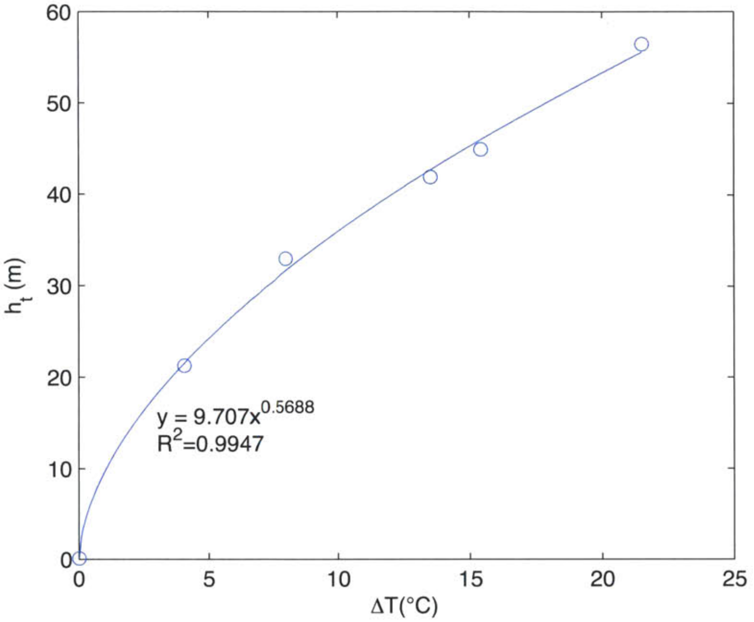

Figure 4.11 - Trap depth (h_t) as a function of the temperature difference between the ambient and the effluent (ΔT).

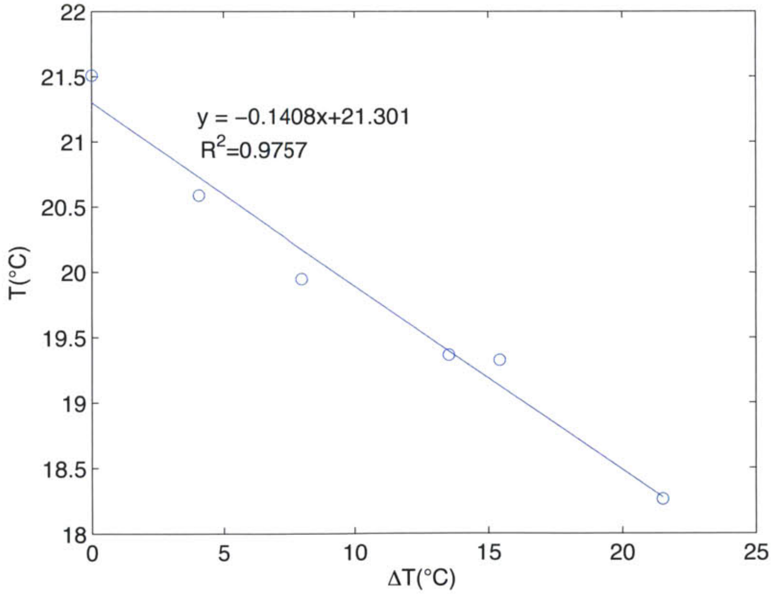

Figure 4.12 - Temperature at the source (T) as a function of the initial temperature difference between the ambient and the effluent (ΔT).

4.1.13 Full Scale OTEC Simulations

In this section we present different OTEC plant configurations simulated by MITgcm. With this analysis we aim to determine the effectiveness of the model in representing the operation of the OTEC plant. For the following simulations we used the MITgcm source code, with the modifications required to represent an OTEC plant, without including momentum terms at the discharge. The model domain has 3 km horizontal length and 2 km depth. We used a variable grid size, which is 6 m in both the vertical and the horizontal directions in the center of the domain, and it expands further from the source in both directions. Horizontal and vertical eddy viscosities of 10^{-2} m^2/s were used.

1. Combined exhaust, quiescent environment, no rotation effects

Plant characteristics:

- Plant power: 400 MW
- Depth warm intake: at the surface
- Depth cold intake: 1000 m
- Combined exhaust depth: 100 m
- Warm flux: 1600 m^3/s
- Cold flux: 1280 m^3/s

Figure 4.13 shows the plume for this OTEC plant configuration at three different times as indicated in each plot. This stagnant stratified test shows no recirculation of the effluent into the warm intake. The plume presents a preferential direction induced by the square shape of the source. Larger fluxes require larger source length for numerical stability, thus the plume presents less radial symmetry. The plume traps at a depth of 40.8 m below the source. None of the water intakes, even the near surface one that is closest to the effluent exhaust, affect the local velocity field in the discharge. The effect of the cold intake is negligible on the discharged plume.

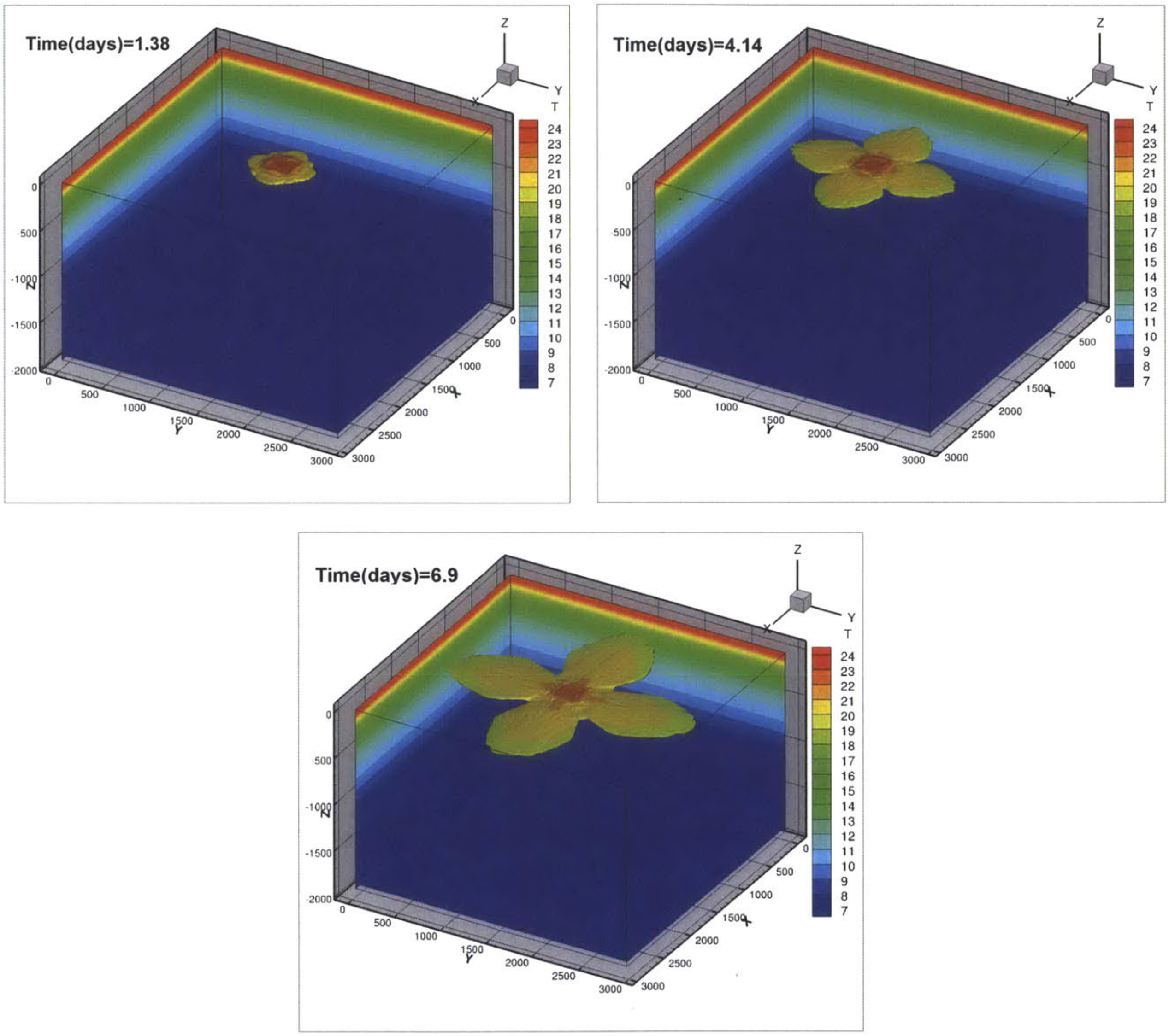

Figure 4.13 - OTEC effluent plume at three different times (combined exhaust, no rotating earth). Plot axes are in meters, T indicates temperature in Celsius.

2. Separate discharge, quiescent environment, no rotation

Plant characteristics:

- Plant power: 17 MW
- Depth warm intake: at the surface
- Depth cold intake: 1000 m
- Warm discharge depth: 50 m
- Cold discharge depth: 100 m
- Warm flux: 67 m^3/s
- Cold flux: 53 m^3/s

Figure 4.14 shows the plume for this OTEC plant configuration at three different times as indicated in each plot. The shapes of the plumes are affected by the square geometry of the sources. For this model configuration we observed recirculation of the warm effluent into the warm intake. However, there is no recirculation of cold effluent. The effect of the cold intake on the cold and the warm plumes is negligible. The cold plume traps at a depth of 42.5 m below the source, while the warm effluent is being pumped into the warm intake.

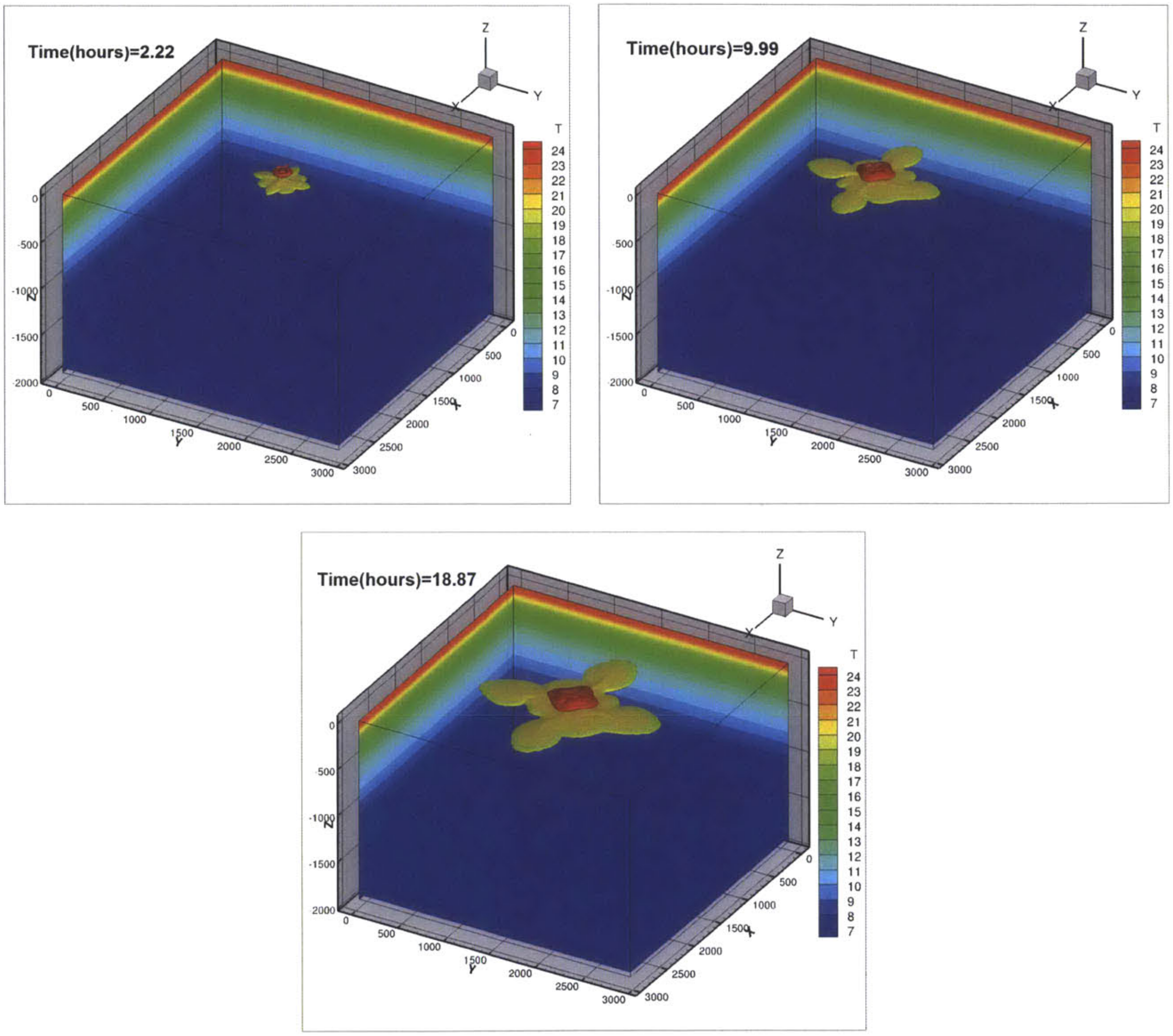

Figure 4.14 - OTEC effluent plume at three different times (separated exhaust, no rotating earth). Plot axes are in meters, T indicates Temperature in Celsius.

3. Combined discharge, quiescent environment, rotating frame northern hemisphere

Plant characteristics:

- Plant power: 200 MW
- Depth warm intake: at the surface
- Depth cold intake: 1000 m
- Mixed discharge depth: 100 m
- Warm flux: 800 m^3/s
- Cold flux: 640 m^3/s

Figure 4.15 shows the plume for this OTEC plant configuration at three different times as indicated in each plot. At the surface level we observe a cyclonic vortex flow due to the sink at the surface. There is a slight depression of the surface water of about 5 cm above the plant. There is no significant rise in isotherms due to the fluid intake. The diverging and spreading plume rotates clockwise forming an anticyclonic vortex, and it traps at a depth approximately of 48 m. The radius of the vortex is approximately 1.2 km at 7.2 hours after the beginning of OTEC pumping, and its maximum velocity is approximately 0.15 m/s. There are no significant differences in the plume trap depth when compared to scenarios without a Coriolis force on the plume. At the cold intake depth we observe a cyclonic vortex.

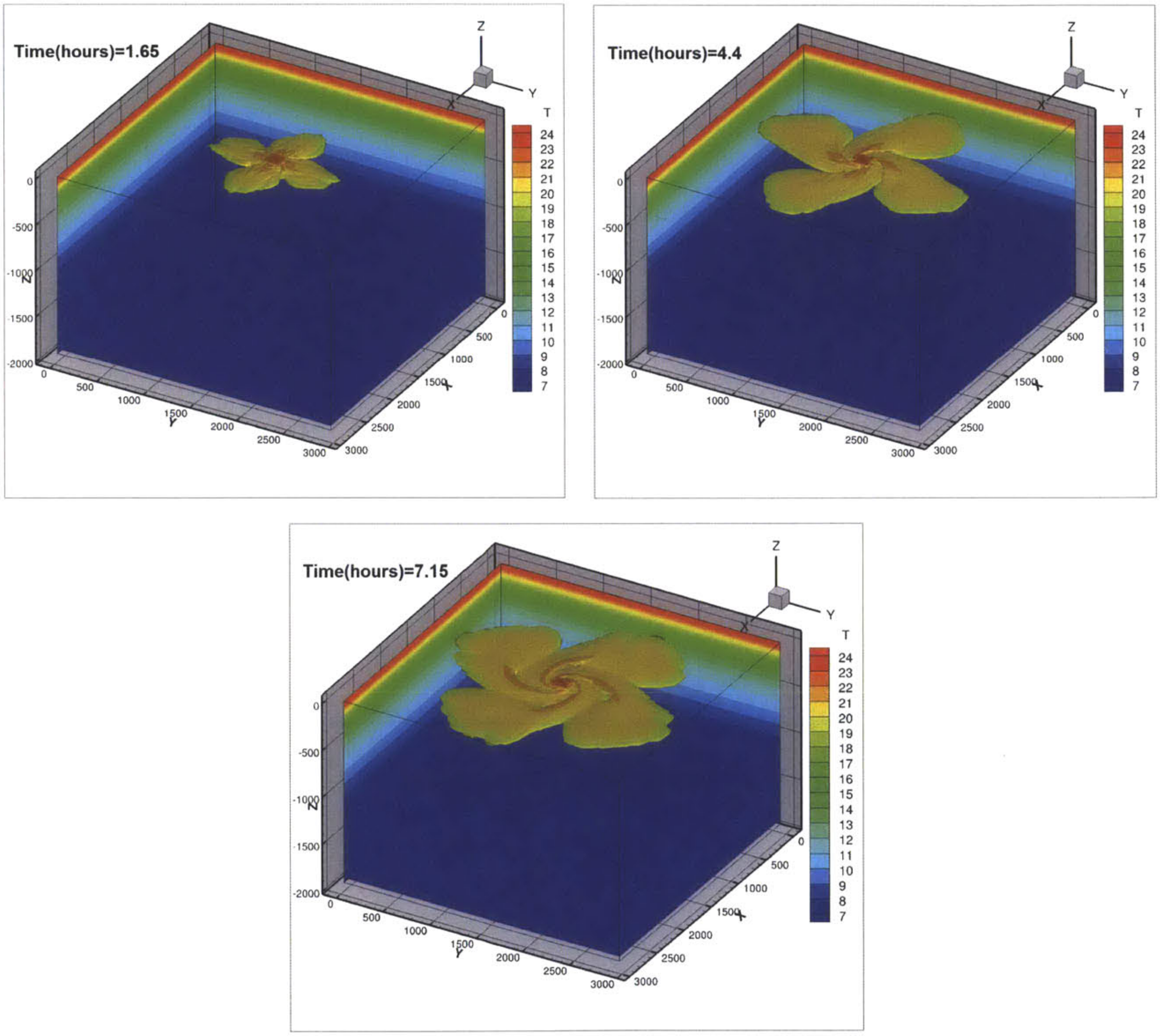

Figure 4.15 - OTEC effluent plume at three different times (combined exhaust, rotating earth). Plot axes are in meters, T indicates Temperature in Celsius.

4. Separate discharge, quiescent environment, rotating frame northern hemisphere

Plant characteristics:

- Plant power: 100 MW
- Depth warm intake: at the surface
- Depth cold intake: 1000 m
- Warm discharge depth: 50 m
- Cold discharge depth: 100 m
- Warm flux: 400 m^3/s
- Cold flux: 320 m^3/s

Figure 4.16 shows the plume for this OTEC plant configuration at three different times as indicated in each plot. Both warm and cold effluent plumes rotate clockwise. The warm effluent recirculates into the warm intake. The sinking cold effluent at the source drags fluid from the above layer, causing the warm effluent to be entrained into the cold source grid cells.

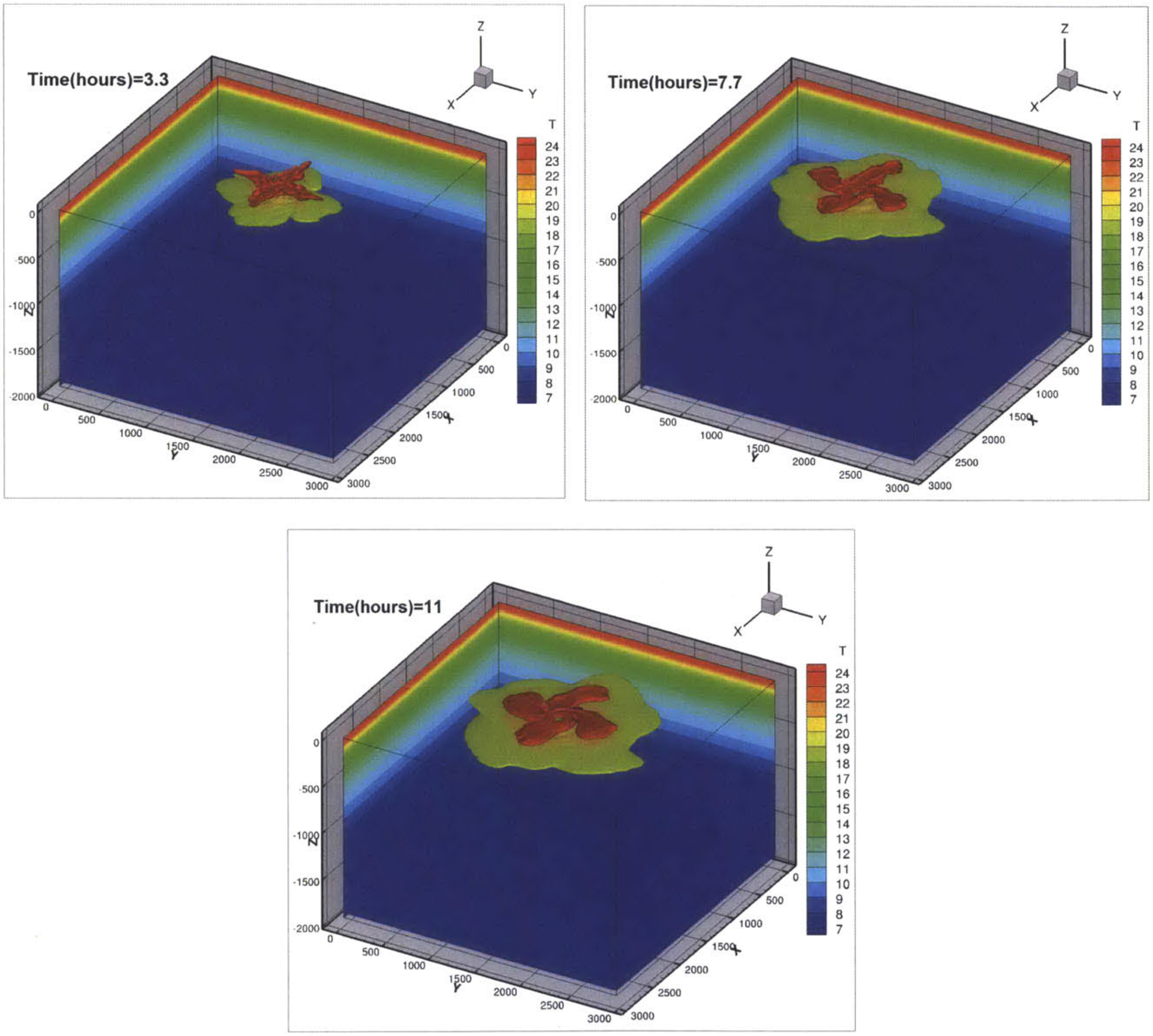

Figure 4.16 - OTEC effluent plume at three different times (separate exhaust, rotating earth). Plot axes are in meters, T indicates Temperature in Celsius.

5. Separate discharge, geostrophic currents of 10 cm/s

Plant characteristics:

- Plant power: 100 MW
- Depth warm intake: at the surface
- Depth cold intake: 1000 m
- Warm discharge depth: 50 m
- Cold discharge depth: 100 m
- Warm flux: 400 m^3/s
- Cold flux: 320 m^3/s

Background Flow

We considered a background steady flow of 0.1 m/s. The background flow is generated in MITgcm as a geostrophic flow. The flow is driven by a water surface slope that produces a pressure gradient to balance the Coriolis force.

The geostrophic flow u_o, along x-direction, is given by:

$$g\frac{\partial\eta}{\partial y} + f u_o = 0$$

where η represents the water surface elevation, and f represents the Coriolis parameter (assumed to be 10^{-4} s^{-1}). The required surface elevation to generate the geostrophic current is:

$$\Delta\eta = -\frac{f}{g}u_o\Delta y$$

The domain is closed in the y direction and periodic in the x direction; in this way no boundary effects are introduced in the x direction while still allowing flow.

In MITgcm, for simplicity, this flow was created by imposing an initial surface elevation with the slope required to generate a uniform current of 0.1 m/s. This geostrophic flow was imposed as an initial condition in the entire fluid domain. By eliminating friction in the bottom and walls of the domain, the generated flow approximates very well to a geostrophic flow for the simulation times used, without introducing significant errors.

Figure 4.17 shows the plume for this OTEC plant configuration for two times as indicated in each plot. There is strong initial mixing induced by the background currents. This enhanced mixing reduces the sinking of both plumes. We can see some recirculation of the warm effluent into the warm intake.

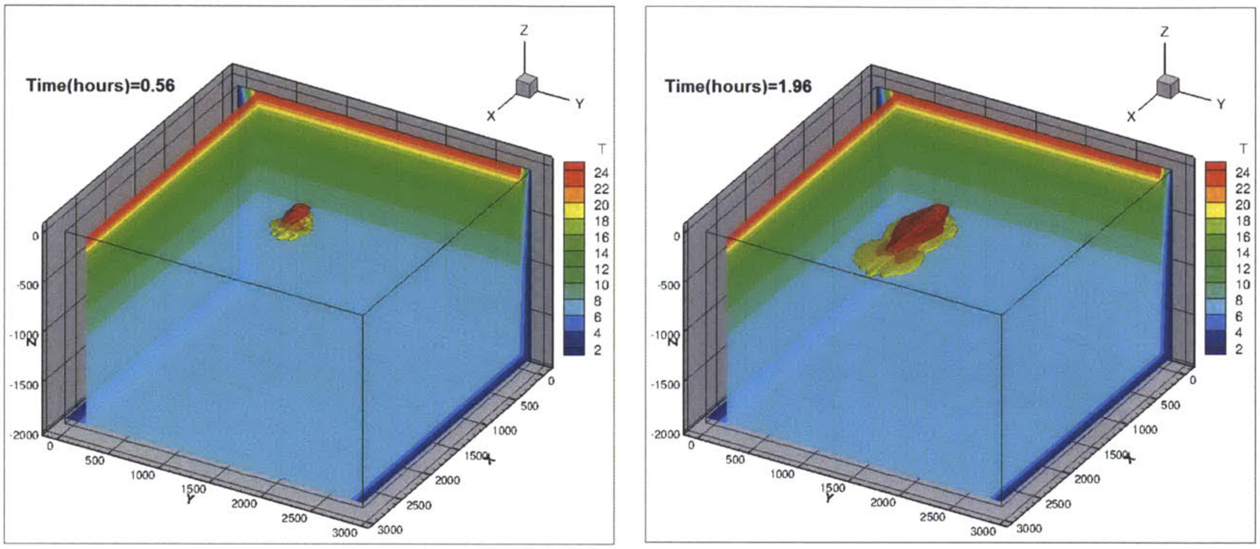

Figure 4.17 - OTEC effluent plume at two different times (separate exhaust, geostrophic currents of 0.1 m/s). Plot axes are in meters, T indicates Temperature in Celsius.

6. Combined discharge with geostrophic currents of 10 cm/s

Plant characteristics:

- Plant power: 100 Mw
- Depth warm intake: at the surface
- Depth cold intake: 1000 m
- Warm discharge depth: 50 m
- Cold discharge depth: 100 m
- Warm flux: 400 m^3/s
- Cold flux: 320 m^3/s

Figure 4.18 shows the plumes for this OTEC plant configuration for two times as indicated in each plot. Enhanced mixing due to currents produces little sinking of the combined exhaust plume as seen in the figure.

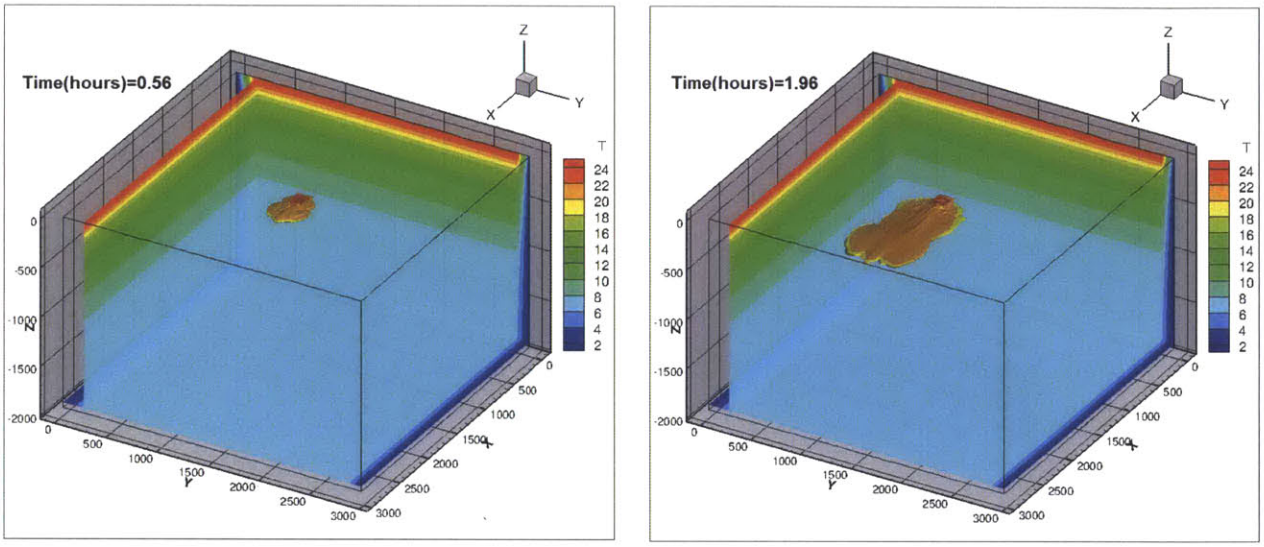

Figure 4.18 - OTEC effluent plume at two different times (combined exhaust, geostrophic currents of 0.1 m/s). Plot axes are in meters, T indicates Temperature in Celsius.

4.1.13.1 Modeling Conclusions

In all the simulations carried out, a combined OTEC discharge had no effluent recirculation into the warm intake. This can be explained by the negative buoyancy of the plume being strong enough compared to the sink intake effect. In all the simulations, effluent discharges at 100 m depth do not penetrate much below the releasing point due to the strong ambient stratification. However, the enhanced numerical mixing and dilution in MITgcm may overestimate the entrainment and therefore underpredict the right trap depth.

In all the simulations carried out, there is no interaction between the cold intake and the warm intake since they are very far apart. Ambient currents lengthen the trajectory of the discharge plume and increase plume dilution. In a current, the plume reaches its equilibrium shallower depths, which can be explained by the enhanced mixing.

4.2 Distributed Sources and Sinks Approach

The aim of this approach is to use analytically computed distributed sources and sinks as "internal boundary conditions" for the general circulation model. The effect of the near field mixing is represented by a distribution of mass sources and sinks. The plume mixing is represented by a diluted source flow and entrainment sinks along the jet trajectory. Choi and Lee (2007) applied this method to a number of environmental problems.

Figure 4.19 shows distributed sinks along the predicted plume trajectory representing the plume entrainment. Sources placed at the predicted neutral buoyant depth represent the diluted flow of the plume discharge. The integral model determines the sources' and sinks' strength and their respective positions in the fluid domain. The distributed sources and sinks are introduced into the MITgcm computational domain to solve numerically for the far field of the OTEC plume discharges.

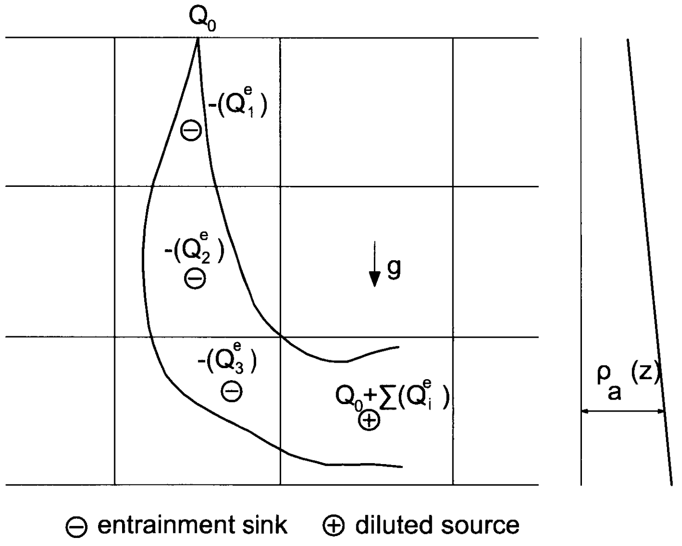

Figure 4.19 - Sources and sinks method schematization (Choi and Lee, 2007).

The coupling between the near and far field is achieved by the following steps:

1. Use near and intermediate field models to compute the entrainment and turbulent mixing

2. Use far field model, MITgcm, with near and intermediate field replaced by the distributed sources and sinks

This method enables the use of a much larger grid size. Consequently, the simulations are less computationally demanding, as larger time steps can be used. In this study, the far field grid size used is of the order of one kilometer, while the grid size required in the first approach, *"Brute Force"*, is on the order of a meter. Other OTEC studies on a global scale, such as Rajagopalan and Nihous (2013), employ a grid size of the order of 400 km.

In the following sections we present the study of OTEC plumes on a larger scale using the distributed entrainment sources and sinks method. Sources' and sinks' strength, location, and velocities are computed via the integral models for the near and intermediate field. The plume trajectory indicates where the entrainment sinks are placed. The source represents the diluted flow, and is located at its neutral buoyancy level.

4.2.1 Application to a Single OTEC Plant

Here we analyze how MITgcm represents one operating OTEC plant in a quiescent ambient and without considering earth's rotation, by using the distributed sources and sinks approach. The near and intermediate field mixing is represented in the far field model by a vertical distribution of sources and sinks of mass as shown in Figure 4.20. Sinks placed at the grid cells occupied by the plume represent the plume entrainment at that location. The diluted flow at the end of the plume is represented by a source term.

The far field model employs a grid size of 1065 m of horizontal length, which is the sum of the near and the intermediate field scales. The grid height is 10 m. The near and intermediate field plume characteristics are presented in Sections 3.3 and 3.4. In this simulation, no rotation effects are considered, since it is intended only to simulate the fluid dynamics generated by sources and sinks of mass within a stratified ambient.

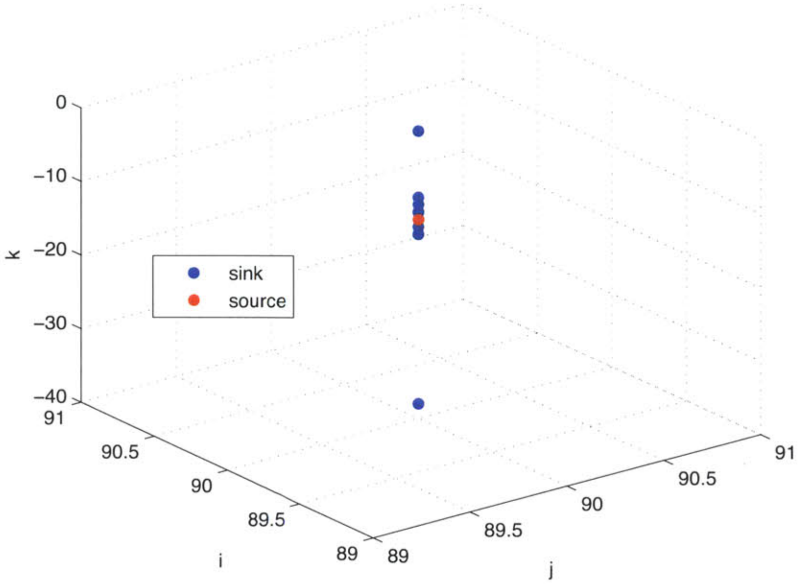

Figure 4.20 - Sources and sinks distribution in the mesh grid of the far field model. Plot axes (i,j,k) indicate the index of each grid cell of the model.

In the far field model, the released fluid is neutrally buoyant since the plume has already reached its neutrally buoyant depth. Figure 4.21 shows a horizontal plane at the source of mass, where the flow is radially outward. The neutrally buoyant fluid spreads horizontally at the released elevation like an intrusion layer, as shown in Figure 4.22. The discharged fluid entrains fluid from the layers above and below. As the top layer is less dense, the entrainment from it is stronger than the entrainment from the bottom layer. At 37 days from the beginning of the discharge, the plume has a diameter of 25.2 km. There is a strong vertical flow between the layers around the dipole (source and sinks next to each other). There is some recirculation from the source towards the sink due to their proximity. However, this effect is just limited to the region immediately surrounding the dipole.

The flow near the cold and warm intakes (the lowermost and uppermost sinks) is radially inward, as shown in Figure 4.23. The warm intake, located at the water surface, withdraws fluid from the layer beneath it. The effect of the cold intake is largely localized in the area surrounding this sink. It has no effect on the velocity field near the plume entrainment or warm intake because of the distance between them.

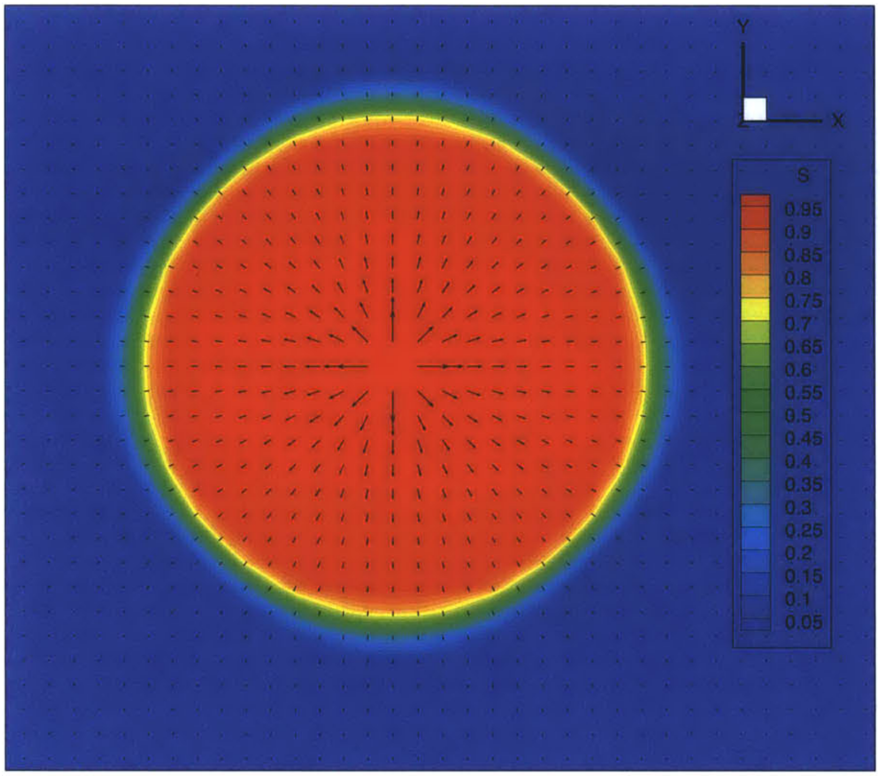

Figure 4.21 - Horizontal slice of the flow at the source level 37 days into OTEC operation. Color scale indicates the tracer concentration S, the released fluid has a concentration S=1. Arrows correspond to velocity vectors.

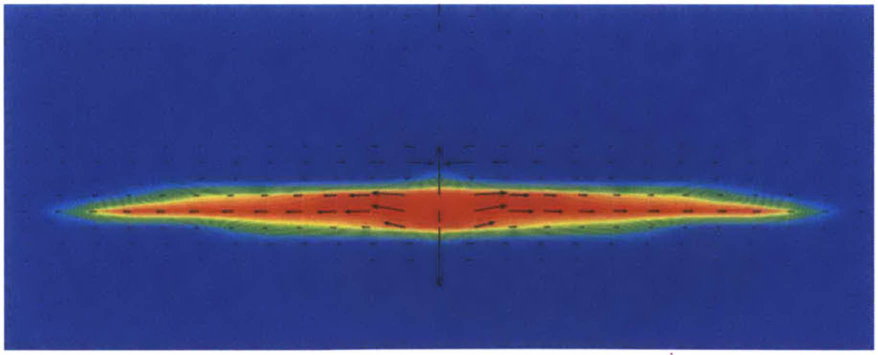

Figure 4.22 - Vertical slice of the flow across the distributed sources and sinks 37 days into OTEC operation. Arrows correspond to velocity vectors, color scale indicated in Figure 4.21.

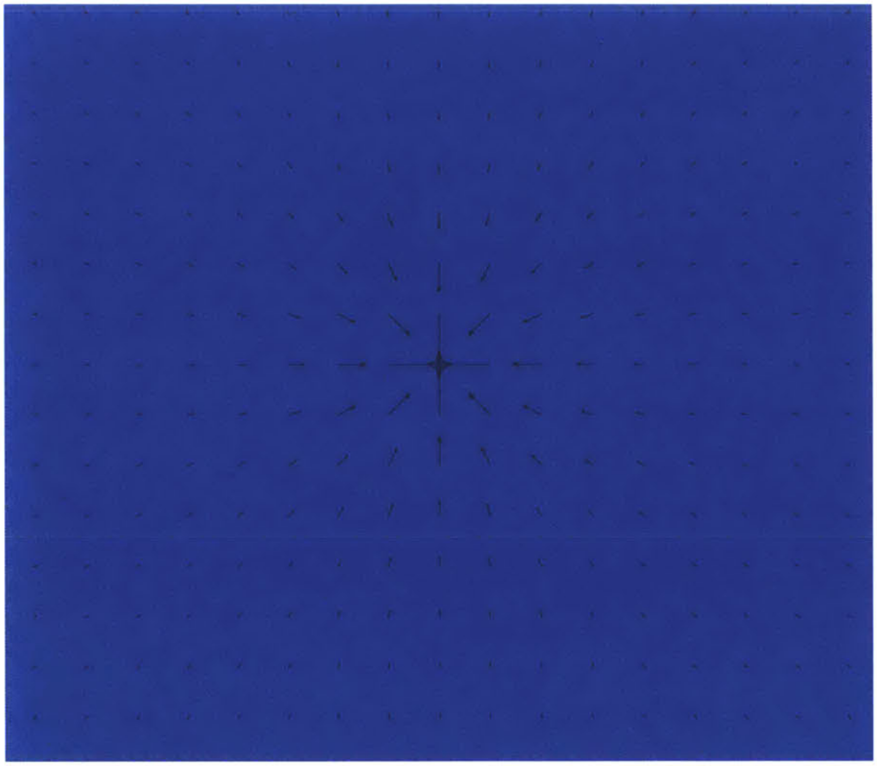

Figure 4.23 - Horizontal slice of the flow at a sink level. Arrows correspond to the velocity vectors.

4.2.2 Application to Group of OTEC Power Plants

As an application of the sources and sinks coupling approach, we analyzed the interaction between four operating OTEC plants, as illustrated in Figure 4.24. The preliminary plant spacing was determined from the recommended OTEC plant density of 190 kW/km^2 (Avery and Wu, 1994). Considering power plants of 100 MW output, the average plant spacing is 22.9 km.

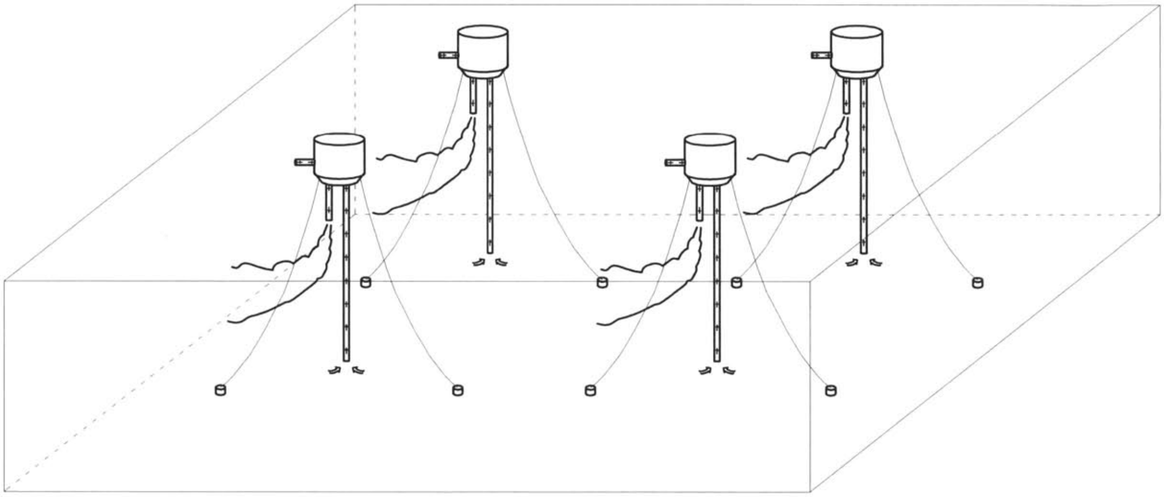

Figure 4.24 - OTEC group of plants.

When using the distributed sources and sinks approach, it is of interest to analyze:

1) Interaction of thermal plumes of adjacent plants
2) Redistribution of nutrients

This analysis considered a background current of 0.1 m/s. To produce that geostrophic current in the modeled domain, which has a width of 126 km, assuming a Coriolis parameter $f = 10^{-4}\ s^{-1}$, a water surface elevation difference of 12.8 cm was required.

We studied the interaction of four OTEC plants with different discharge depths ranging from 50 m up to 100 m. Figure 4.25 shows a top view of the configuration of the plants. Each plume has different horizontal and vertical extents, as each plume has different initial buoyancy.

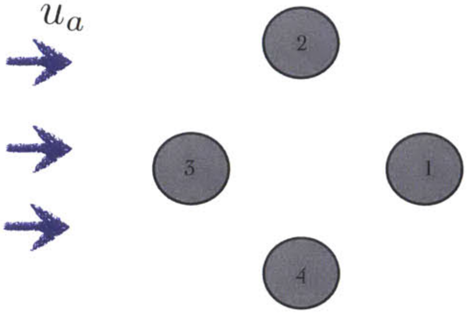

Figure 4.25 - Top view of OTEC group of plants.

The near and intermediate field models are used to predict each plume's characteristics and to determine the location and strength of each sink and source used. Figure 4.26 depicts their locations in the MITgcm grids. The far field model grid size is 700 m in horizontal length and 10 m in height. This grid size comprises the near and intermediate field scale for all the plumes.

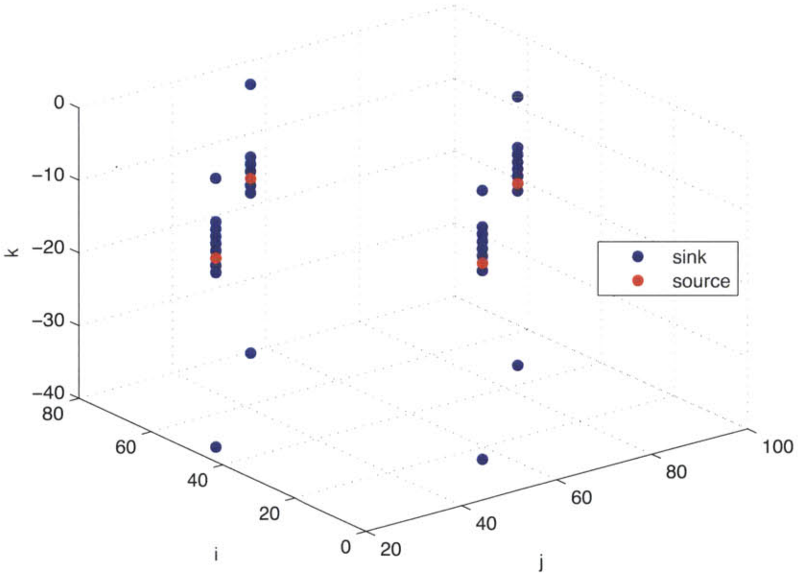

Figure 4.26 - Sources and sinks distribution in the mesh grid of the far field model for a group of OTEC plants. Plot axes (i,j,k) indicate the index of each grid cell of the model.

Table 4.5 shows the volumetric dilution achieved in the near and intermediate field for each plume. The mixing in the intermediate field is smaller than that of the near field region.

Table 4.5 - Dilutions.

OTEC Plant	Discharge depth (m)	Near field dilution	Intermediate field dilution	Total dilution
1	100	6.07	2.18	13.3
2	70	6.50	2.70	17.5
3	50	6.38	2.02	12.9
4	60	6.57	1.99	13.0

OTEC plants displace large volumes of deep ocean water to the surface layer. Deep-sea water is uniformly cold, and rich in nutrients. Figure 4.27 displays the vertical distribution of the concentration of nitrites and nitrates in a tropical ocean. OTEC plants bring nutrients to near surface depths. In Section 4.2.2.2 we present the effect of operating OTEC plants on nutrients redistribution in the far field using the distributed sources and sinks method. The nutrient upwelling effect of OTEC plants is further detailed in Chapter 5.

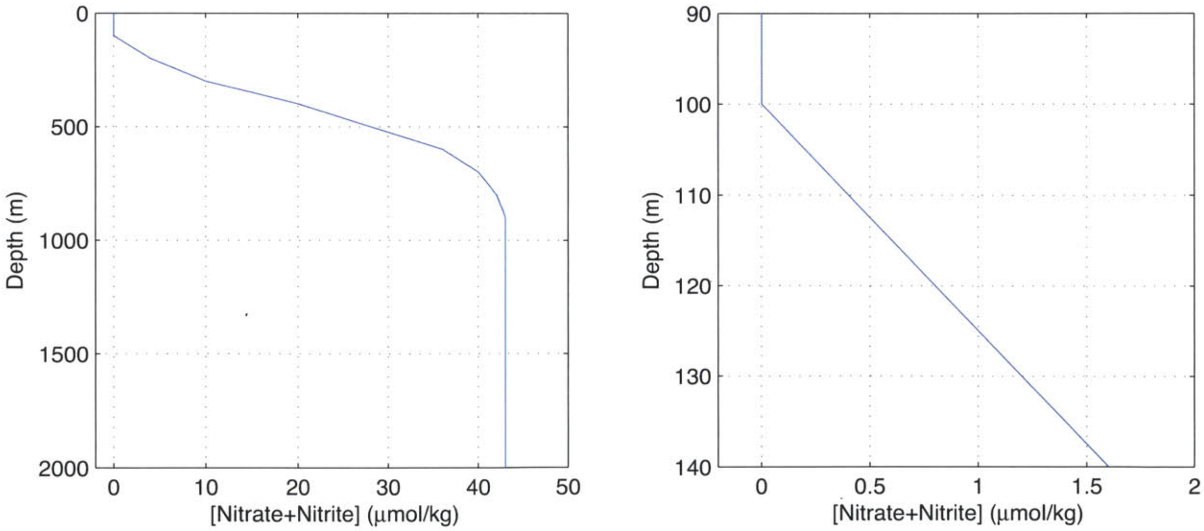

Figure 4.27 - Natural vertical distribution of nutrients (adapted from Makai Ocean Engineering "Otec Hydrodynamic Model", based on 8 years of data from HOTS Station ALOHA, courtesy of University of Hawaii SOEST).

Coupling

For each plume, the final nutrient concentration at the end of the intermediate field was computed accounting for the entrainment of nutrients into each plume in addition to the nutrient concentration in the intake flows. The resulting concentration in the diluted plume is used as input concentration in the far field model.

The nutrient concentration at the end of the intermediate field is computed as:

$$C_{out} = \frac{\sum_i C_i Q_i}{Q_{out}}$$

where C_i and Q_i are the nutrient concentration and entrainment flow at different depths along the plume trajectory respcctively. Plant numbering is indicated in Figure 4.25. Table 4.6 presents the effluent characteristics at the end of the intermediate field, which are the inputs to the MITgcm model. The resulting nutrient concentration at the end of the intermediate field for the four plumes is higher than the natural ambient concentration despite the dilution in the near and intermediate field.

Table 4.6 - OTEC discharge characteristics for each plant of the group.

OTEC Plant	OTEC Discharge Depth (m)	C_{out} (μmol/kg)	Plume Equilibrium Depth (m)	$C_{ambient}$ (μmol/kg)	$C_{out}/C_{ambient}$
1	100	2.63	137.9	1.52	1.7
2	70	2.22	121.0	0.84	2.6
3	50	1.68	103.3	0.13	12.7
4	60	1.95	112.8	0.51	3.8

4.2.2.1 Interaction in Temperature Field

Figure 4.28 shows the boundary of the four plumes defined by a surface of a tracer concentration 0.01. The tracer concentration is defined as unity at the fluid source. The temperature of the plume boundary is indicated by the color scale. Also in the plot, one horizontal and two vertical slices are shown to illustrate the vertical and horizontal distribution of temperature of the modeled domain.

The plumes are advected by the ambient currents. While the plumes move downstream, they grow in radius due to turbulent diffusion. They do not merge horizontally within the modeled domain, since they are very far apart. The plume released from Plant 3 merges with the downstream plant plume. In the simulations presented in this section, we used a horizontal tracer diffusion coefficient of 4×10^{-1} m^2/s and zero in the vertical direction (explicit coefficients). Other simulations with higher horizontal and vertical diffusion coefficients, show more plume spreading in each direction respectively.

As the released fluid in the far field is neutrally buoyant (the plume had reached its equilibrium depth at the end of the near field), the temperature of the plume is equal to that of the background ocean. With background flow, for the plant configuration analyzed in which a sink term is located downstream of a source term, the downstream plants withdraw water from the upstream incident plume. However, as the plume temperature is the same as the background ambient, there is no negative interaction between plants. No plant will affect the thermodynamic efficiency of adjacent plants. The plume flux is much larger than the intake sink flux, and hence the remaining fluid of the plume moves beyond the sink.

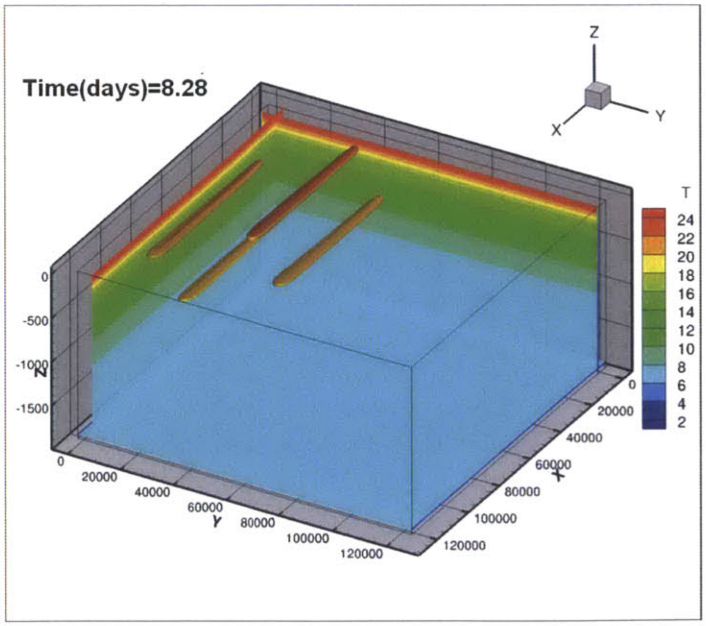

Figure 4.28 - OTEC effluent plumes. Plot axes are in meters, T indicates water temperature in Celsius. Two vertical slices and one horizontal slice are shown to indicate the T field.

Figure 4.29 shows four horizontal slices, one at each plume's equilibrium depth. Subplots a) to d) are ordered by increasing depth. In the first slice, Figure 4.29(a), only the plumes of Plant 3 and 4 are reached. In Figure 4.29(b) all plumes are reached except that corresponding to Plant 1. Figure 4.29(c) captures the intermediate depth plumes and Figure 4.29(d) only captures the deeper ones (plumes corresponding to Plants 1 and 2). In all cases, the plumes start with tracer concentrations near unity at the release point, and then disperse over time as the plumes are advected downstream.

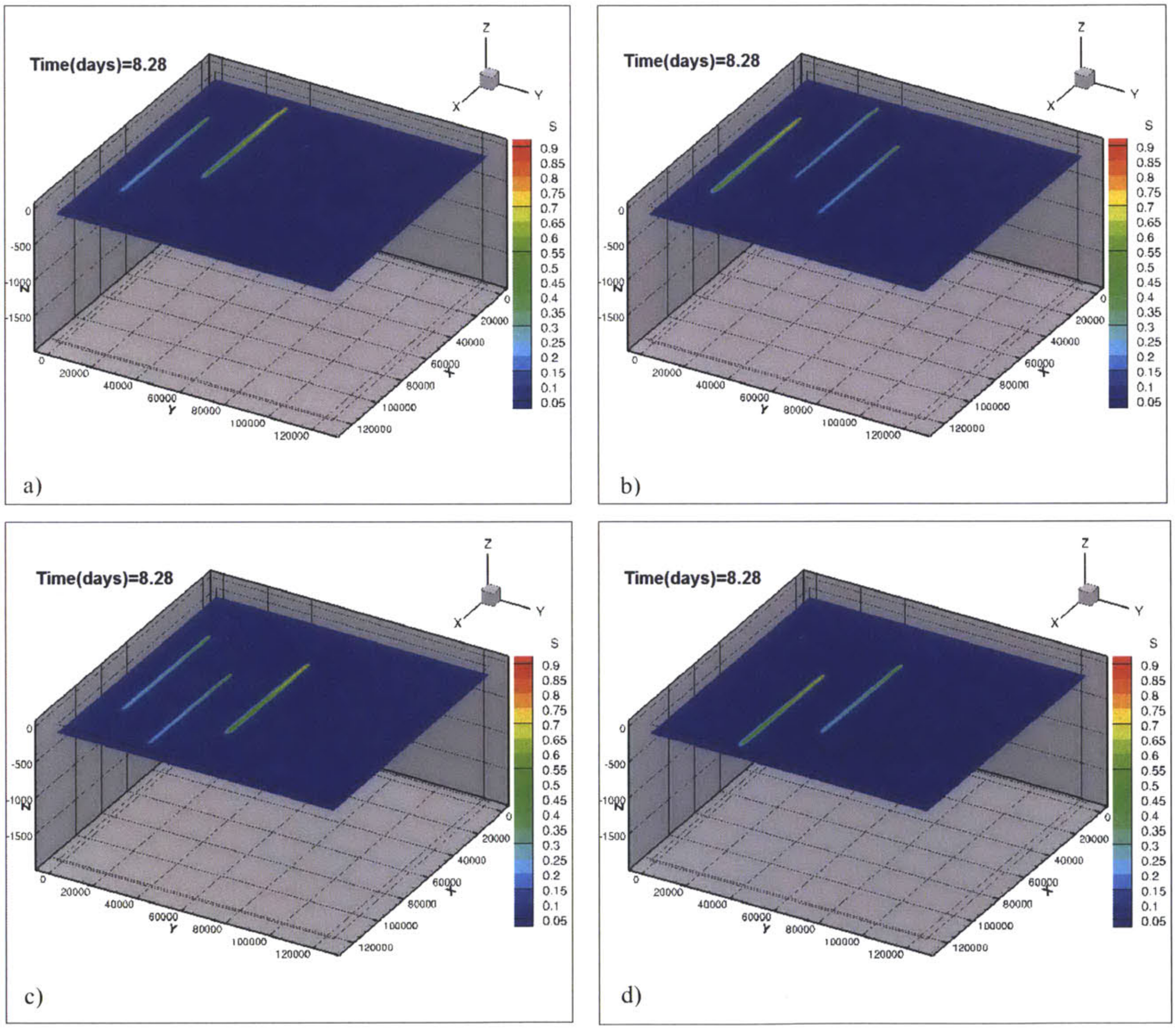

Figure 4.29 - Tracer concentration field (S) shown at four different depths. Plot axes are in meters.

4.2.2.2 Nutrient Redistribution

The plumes do not merge horizontally, which indicates that the plant spacing is large enough. At each level, each plume has a higher nutrient concentration than the environment for the four plants analyzed. Further downstream from the discharge, turbulent diffusion dilutes the plume and the concentration barely surpasses the background concentrations. Figures 4.30-4.33 show a horizontal slice at different times for the four different equilibrium elevations of the plumes.

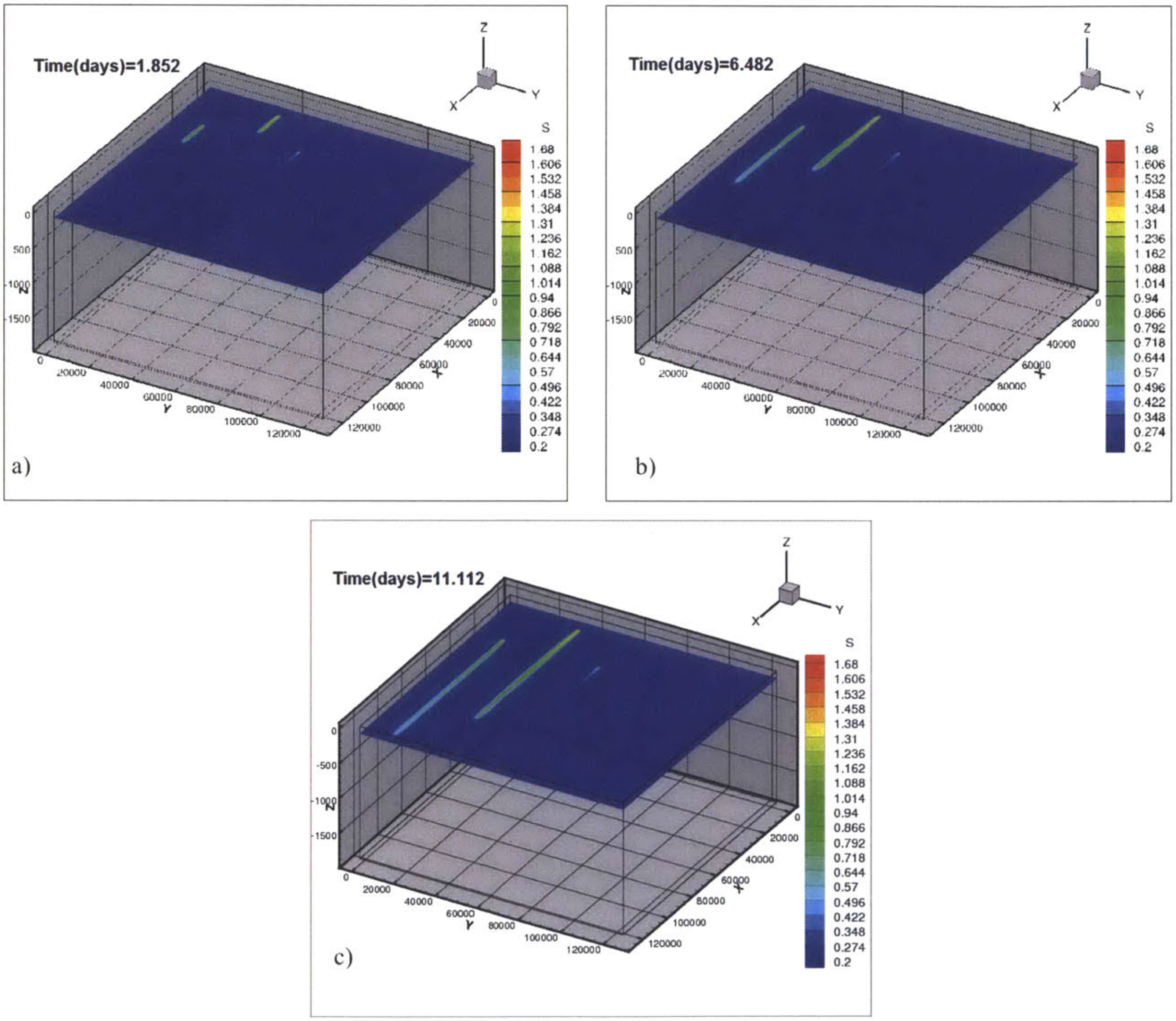

Figure 4.30 - Nutrient concentration at 105 m below the water surface (equilibrium depth of Plume 3) shown at three times. S indicates the nutrient concentration (nitrates and nitrites) expressed in μmol/kg. Plot axes are in meters.

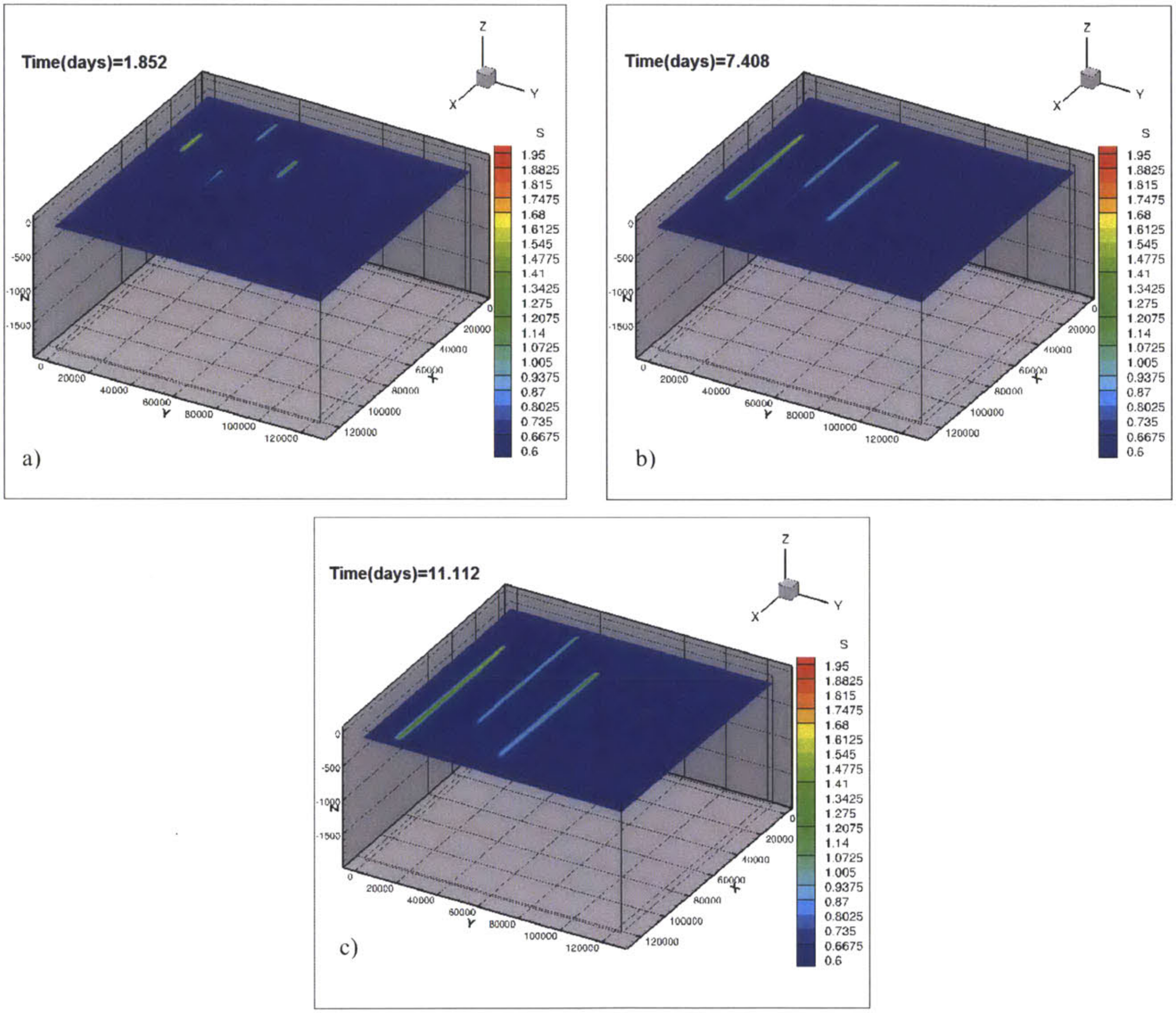

Figure 4.31 - Nutrient concentration at 115 m below the water surface (equilibrium depth of Plume 4) shown at three times. S indicates the nutrient concentration (nitrates and nitrites) expressed in μmol/kg. Plot axes are in meters.

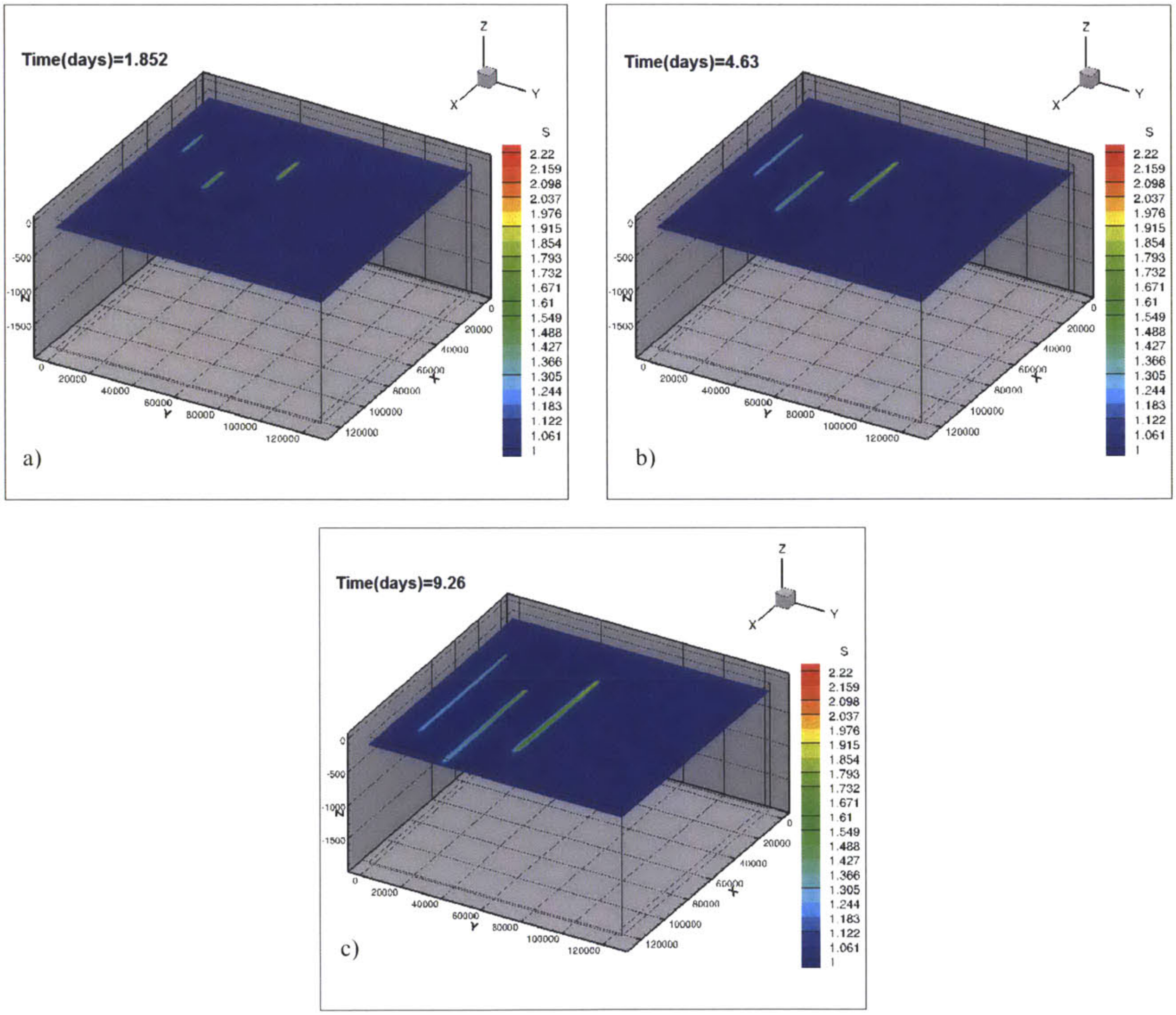

Figure 4.32 - Nutrient concentration at 125 m below the water surface (equilibrium depth of Plume 2) shown at three times. S indicates the nutrient concentration (nitrates and nitrites) expressed in μmol/kg. Plot axes are in meters.

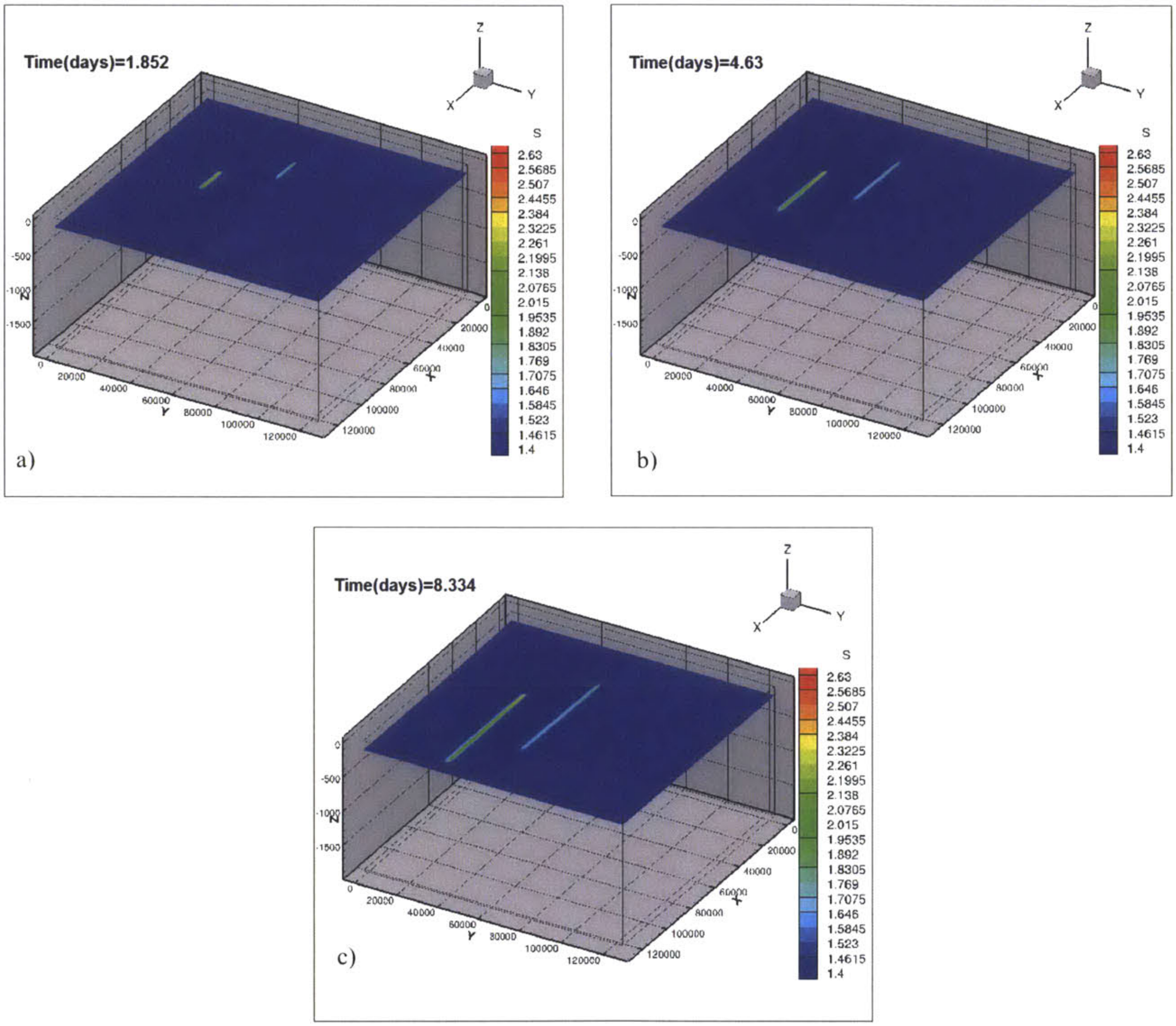

Figure 4.33 - Nutrient concentration at 135 m below the water surface (equilibrium depth of Plume 1) shown at three different times. S indicates the nutrient concentration expressed in μmol/kg. Plot axes are in meters.

Chapter 5 - Environmental Impact

OTEC plants do not produce many pollutants in their normal operation, nor do they consume any non-renewable natural resources. However, they are not entirely without environmental impact: they influence local temperatures and currents, affect fish attraction and production, create local nutrient enhancement, are susceptible to accidents, may occasionally leak some chemicals and corrosion products from metal parts, and require the use of chlorine to prevent biofouling in the heat exchangers.

5.1 Artificial Nutrient Upwelling

An OTEC plant has an upwelling effect, displacing large volumes of deep ocean water into near surface depths. The natural ocean temperature, salinity structure, and nutrient concentration are altered by this water displacement. These aspects have no counterparts in conventional power plants.

This displacement of deep ocean water to the surface layer brings with it nutrients such as nitrites, nitrates, phosphates, and silicates that enrich surface water and may lead to phytoplankton blooms. This is similar to natural upwelling, and the consequence may be enhanced fishery production. Micronutrients (iron, manganese, and copper) can also increase algae production. Heightened concentrations of metals such as copper, zinc, or cadmium could be toxic (Myers et al., 1986).

Here we present the upwelling effect of one OTEC plant in a quiescent stratified ambient. Figure 5.1 is a schematic representation of this artificial upwelling effect of an operating OTEC plant. The figure shows a high nutrient concentrated plume, enhancing phytoplankton production. Figure 5.2 shows a vertical slice of the resulting nutrient concentration distribution (nitrites and nitrates) in the ocean computed by MITgcm. The plant has a 100 MW capacity and has a combined discharge (400 m^3/s warm intake and 320 m^3/s cold intake) at 100 m below the water surface. As the initial condition, we assumed the profile of nutrients shown in Figure 4.27. Figure 5.3 shows the effect of deep seawater pumping on the vertical profile of nutrient concentration at 200 m from the OTEC discharge, 6.6 hours from the beginning of the plant's operation. The OTEC operation produces an excess concentration of nutrients (nitrates and nitrites) that reaches values of 7.9 μmol/kg. This peak of excess nutrient concentration at an intermediate depth is not insignificant, and may cause algal blooms and enhance fishing.

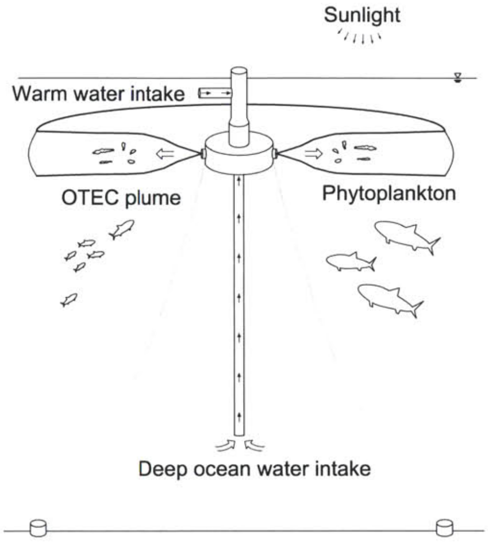

Figure 5.1 - OTEC artificial upwelling effect (adapted from Energinat).

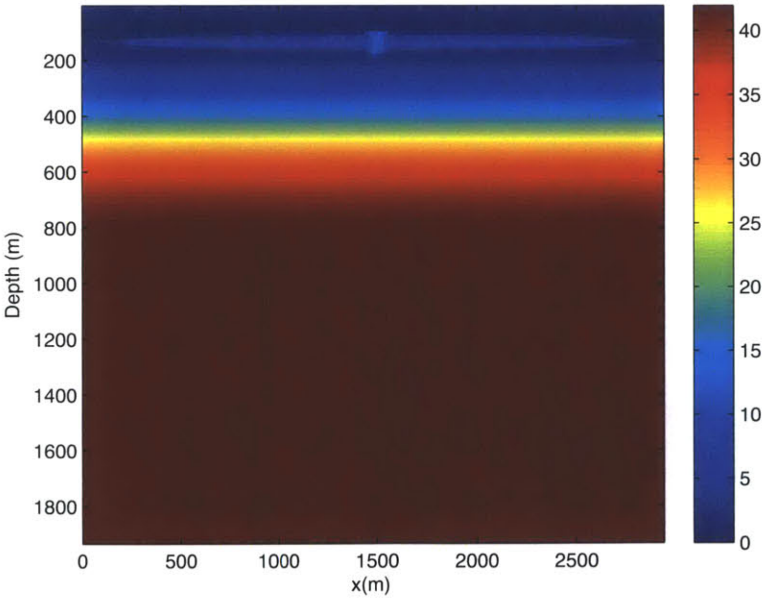

Figure 5.2 - Nutrient concentration (nitrates and nitrites) 6.6 hours into OTEC operation. Color scale: concentration in μmol/kg.

The upwelling effect of an OTEC plant is particularly significant in the near field where the nutrient concentration within the plume is higher than the background concentration. In the far field, the concentration of nutrients in the plume is not much higher than the background concentration due to the high dilution achieved in the near and intermediate field.

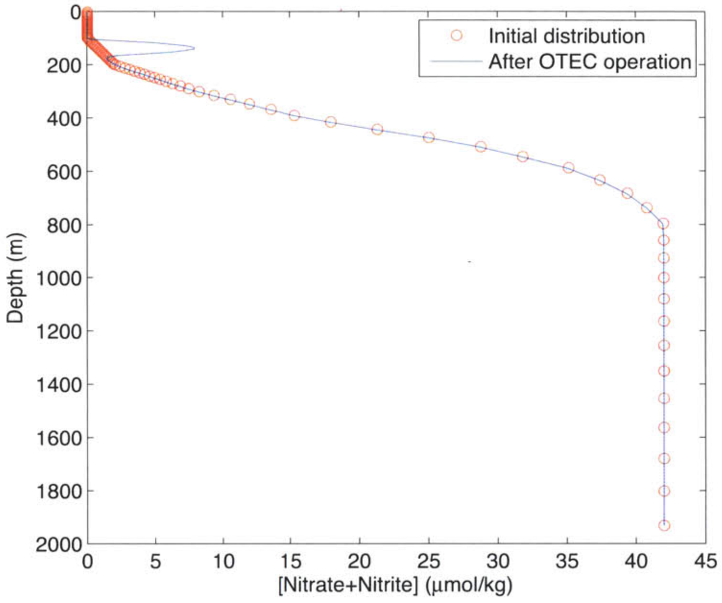

Figure 5.3 - Nutrient redistribution due to artificial upwelling.

Here we present the nutrient concentration computed numerically, by the *Brute Force* method (using a grid size of 6 m and eddy viscosity coefficients of 10^{-2} m^2/s), for a single OTEC plant in a quiescent ambient, in order to portray the nutrient pumping effect.

In Section 4.2.1 (Table 4.6) we present the nutrient concentration at the end of the intermediate field, accounting for the upwelled nutrients from the deep ocean via the cold water intake and for the nutrient entrainment that occurs when the plume sinks and entrains the ambient water, for a background flow of 0.1 m/s. We also analyzed how those nutrients behave in the far field using the sources and sinks method in MITgcm (Figures 4.30-4.33).

Both results (results presented in Section 4.2.1, and presented in this section) represent different ambient conditions, and are therefore complementary to understand the effect of OTEC plants in the environment.

The former analysis studies the nutrients distribution in large scale making assumptions about the nutrients distribution in the near and intermediate field (immediate region of the OTEC plant). The latter presents a numerically computed distribution of nutrients, which verifies the assumptions made in the near and intermediate field (Gaussian distribution of excess nutrients concentration).

In Section 4.2.1, using the integral models to calculate the entrainment fluxes, we determined that the concentration at the end of the intermediate field is 2.8 μmol/kg, noting that the plume dilution achieved at 200 m predicted by MITgcm is smaller. This difference in the exact value of concentration can be explained by several factors. Ambient currents increase the final dilution achieved at the end of the near and intermediate field, therefore the concentration computed in Section 4.2.1 is expected to be smaller than the concentration for a quiescent ambient. The length scale of development of the near and intermediate field for the discharge considered, about 700 meters, is larger than 200 m and therefore allows more entrainment, making the plume more diluted at the end of the intermediate field. In addition, as discussed in Section 4.1, MITgcm presents inaccuracies in predicting the right entrainment for large flux discharges. Moreover, as seen in the same section, there is not good agreement between the integral model and the MITgcm predictions, which contributes to this difference in the nutrient concentration, predicted by both models.

5.2 Upwelling Velocity

An OTEC plant operates as an ocean pump, displacing large volumes of water vertically. For the following analysis, we consider a typical 100-MW OTEC power plant, with 400 m^3/s of warm water intake and 320 m^3/s of cold water intake. The warm intake is located at the water surface, and the cold intake is located 1 km below. The OTEC combined discharge (at 17.4°C) is placed at 100 meters below the water surface. Figure 5.4 depicts the OTEC plant pumping effect for this combined discharge.

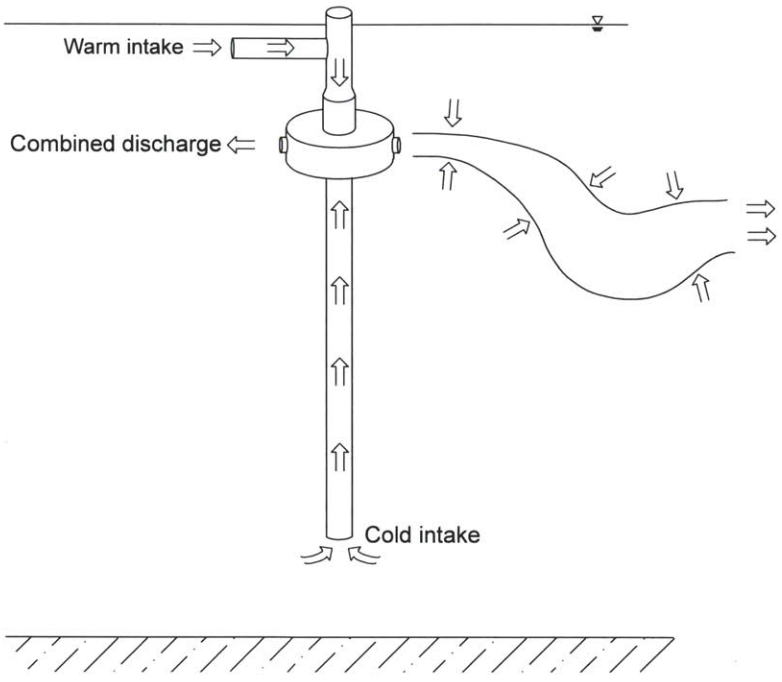

Figure 5.4 - Schematization of OTEC pumping effect for combined discharge.

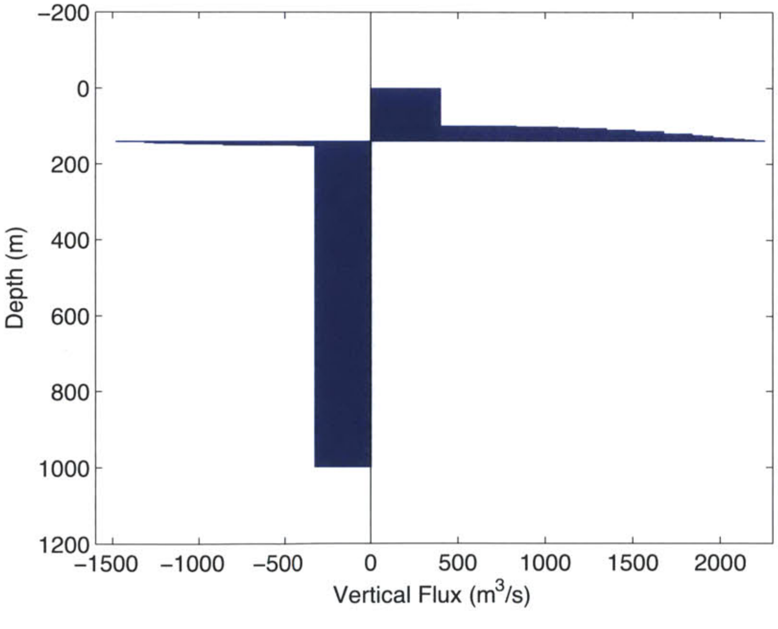

Figure 5.5 - Upwelling effect for a 100-MW OTEC plant with combined discharge.

Figure 5.5 shows a vertical distribution of the vertical flow rate induced by the OTEC pumping. These flow rates are due to the warm intake, the entrainment flux induced by the plume discharge in the near and intermediate fields, the outward flux at the end of the plume, and the cold intake. Their overall effect induces upwelling and downwelling velocities as shown in the figure (note that a positive flow rate implies a vertically upward flow rate). For this analysis, the outward flux at the end of the intermediate field is considered to be located at the center of the spreading layer cross-section.

To help interpret this figure, we will proceed from the water surface to the ocean bottom. In the top 100 meters of water, the warm intake induces an upwelling flux to supply the sink of mass. At 100 meters below the water surface, the discharged plume starts to develop downward since the discharged fluid is denser than the ambient. The plume entrainment demands more water that must be supplied from the layers below, and therefore it increases the upwelling flux, as can be noted in the figure.

Reaching the level of neutral buoyancy of the plume, there is an important outflow equivalent to the plume-diluted flux. This volume flux surpasses the volume demanded by the warm intake and the plume entrainment (this corresponds to the change of sign of the vertical flux seen in the figure). Therefore, below the equilibrium depth, there is a downward flux. Just below this point there is some vertical development of the plume, which entrains fluid. For this reason the downward vertical flux gradually decreases down to the maximum depth of the plume. Further down, this downwelling flux has a constant value (equal to the cold intake flow) until reaching the sink level. Below this level, all the fluxes are in balance, to supply the required volume of water of the sinks given by the sources, and therefore the resulting induced upwelling velocity is zero.

Assuming an OTEC plant density of 190 kW/m^2 and based on results presented in Figure 5.5, for the combined discharge of the 100-MW plant considered, the maximum induced downwelling velocity is 0.24 m/day and the maximum upwelling velocity is 0.37 m/day.

Figure 5.7 shows the vertical distribution of the vertical flow rate induced by the OTEC pumping for the same OTEC plant characteristics as described in the previous analysis, but considering separate discharges. The separate discharge configuration is depicted in Figure 5.6. The warm water discharge (at 24°C, since 1°C is assumed to be lost in the heat exchanger) and the cold water discharge (at 9°C, since 1°C is assumed to be gained in the condenser) are located 80 and 110 meters below the water surface respectively. For this case, the maximum induced downwelling velocity is 0.21 m/day and the maximum upwelling velocity is 0.24 m/day. This discharge scheme induces smaller upwelling and downwelling velocities than the combined scheme. For the analysis of the mean vertical induced flow a vertical resolution of 2 m is used in both cases presented (combined and separate discharge).

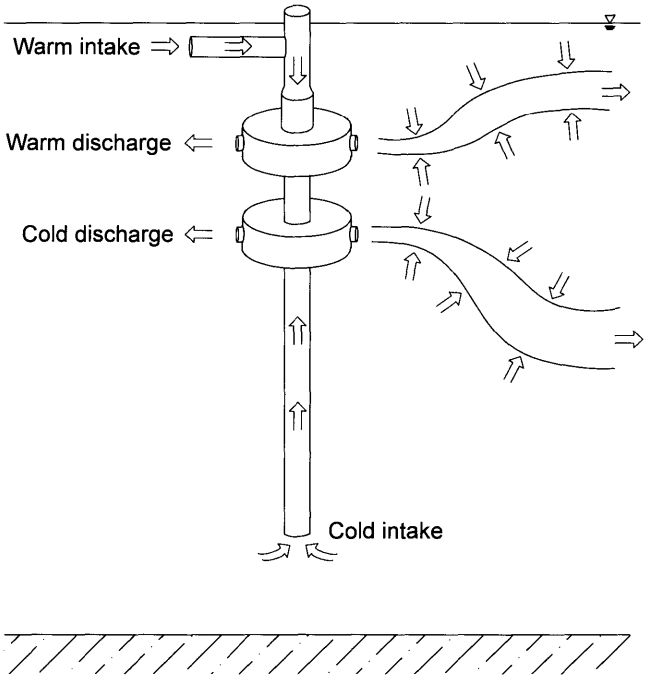

Figure 5.6 - Schematization of OTEC pumping effect for separate discharge.

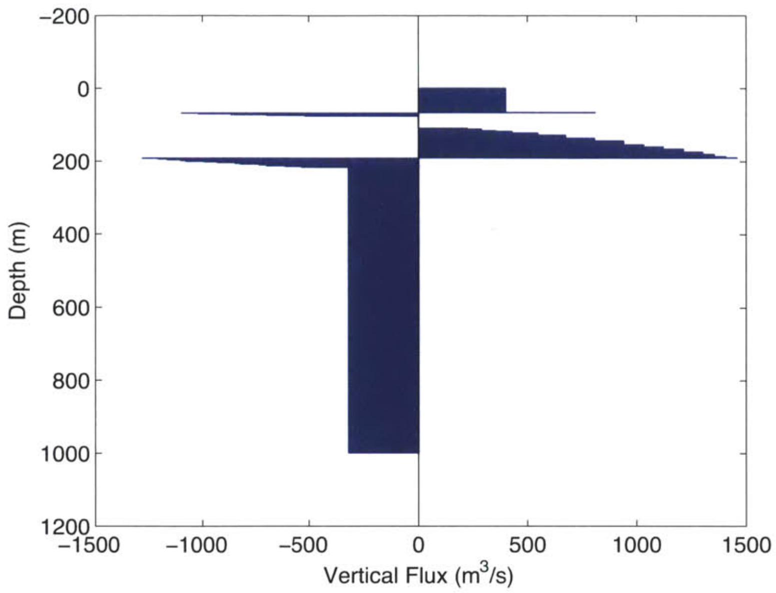

Figure 5.7 - Upwelling effect for a 100-MW OTEC plant with separate discharges.

In the zones where natural upwelling takes place, such as off the coast of Peru, the upwelling velocity can be estimated to be of the order 10 m/day (Avery and Wu, 1994). Assuming a typical natural upwelling of 3 m/day, we can conclude that the OTEC operation induces an upwelling velocity of about 8 to 12% of the natural one. This value is not negligible but not too large compared to natural upwelling velocities.

Chapter 6 - Summary and Conclusions

Ocean models involve a wide range of length scales. Since computer power is limited, no single model can resolve both the centimeter-scale turbulent mixing in an OTEC outflow and the kilometer-scale regional dynamics of the plumes. In this thesis, three models on different scales – near, intermediate, and far field – were developed. A method to couple these models is analyzed in order to study the dynamics of OTEC plumes.

To model OTEC plant discharges in the near and intermediate field of a stratified ocean, we developed steady-state integral models based on well-proven principles. These models predict the characteristics of the plume such as trajectory, volume flux, and excess density. Different discharge configurations (combined and separate discharge, different discharge depths, and different flow rates) and ambient conditions (background currents, several stratification profiles) can be analyzed with these models. A three-dimensional circulation model predicts the flow in the far field.

Two different approaches to coupling the models are analyzed. In the first approach, *Brute Force,* only the far field model, MITgcm, is used for all scales, thereby eliminating the need to couple the models. The plume entrainment computed by a numerical model is found to be highly sensitive to the grid size and eddy viscosity considered. Analytical expressions predict the trap depth and dilution for a simple case of a dense fluid released into a lighter linearly stratified background. Therefore, model parameters of this simple case are adjusted until the simulation matches the analytical prediction. After the model parameters are calibrated, more realistic cases can be modeled.

The second approach, *Distributed Sources and Sinks*, combines all three models. In this method, distributed entrainment sources and sinks are inserted into grid cells of the MITgcm domain. The source and sink locations and flow rates are computed using the near and intermediate field models. The sources and sinks replace the plume mixing effect in the far field model. The MITgcm grid size depends on near and intermediate length scales.

The *Brute Force* approach demands significantly more computational power than the *Distributed Sources and Sinks* approach, since the grid size and the time step required are considerably smaller in the former case than in the latter one. For example, for the highest resolution (grid size of 2 m), the largest domain, and the highest viscosity, one simulation took several days on a 24-processor machine. In some cases the *Brute Force* approach requires using unrealistic values of model parameters, and even with this adjustment, it does not always yield accurate plume simulations.

From the simulations carried out, it can be concluded that the OTEC effluent mixing can be modeled by the *Distributed Sources and Sinks* method of coupling reasonably well. Choi and Lee (2007) demonstrated the accuracy of this method for several complex flows, including ambient stratification, achieving numerical predictions in excellent agreement with laboratory data. This thesis analyzes more complex cases of OTEC plants in a typical tropical stratified ocean. Therefore the accuracy of this method cannot be quantitatively assessed, but is verified qualitatively. The resulting velocity field and the concentration of a tracer coincide qualitatively with the behavior expected for an OTEC discharge. This method also conserves mass and correctly reproduces the trap depth and dilution. However, while this method is good, it is not perfect. The full dynamic effects of the plume mixing on distances smaller than the far field grid size are inherently not represented in the far field model. Moreover, the model produces a dipole, which in fact is not realistic (and hence neither is the local induced flow).

This method of coupling allows us to study interaction among a group of OTEC plants, induced circulations, evolution of certain substances discharged by the plants, and redistribution of ocean nutrients. In the first application of this method, we found that with a current, when an upstream plume reaches a downstream plant, its temperature is the same as the environment. Therefore, the water intake temperature is not affected by the incident plume. Neither plant affects the other's thermodynamic efficiency. Regarding nutrients redistribution, there is a noticeable upwelling effect. Nutrient concentrations in the far field are higher than natural concentrations. This excess could induce phytoplankton blooms.

One big limitation of the study of nutrients redistribution in this research is the preservation of the ambient profile. MITgcm uses diffusivities to mix the fluid supplied by the source, but it also mixes the ambient, therefore eroding the background profile. The real world has sources and sinks of fresh water, nutrients, and heat that are not included in the model used in this thesis that can maintain the ambient profile. Since MITgcm allows using different diffusivities for heat than for tracers, we did not face that problem for the background temperature stratification.

These results were only obtained under geostrophic current conditions. However this approach is also applicable under other types of background conditions, such as non-uniform, non-steady flow.

Additionally, approximations made in the near and intermediate field models do not permit study of an OTEC plant's interaction with itself, which is still a major outstanding issue, particularly for the OTEC separate discharge scheme. It may be recalled that in Section 4.1.14, a simulation was run for a 100-MW plant, with 50 meters separation between the intake and the warm exhaust, and some recirculation of the warm discharge was observed. In order to more carefully study this issue, additional modeling efforts should be conducted.

As a future direction for further research, optimal OTEC plant spacing needs to be determined more accurately to ensure efficiency of energy production. Currently, other studies recommend only approximate values. This thesis considers steady currents to analyze adjacent OTEC plume interaction. Other types of background conditions need to be studied. As a next step in the analysis of plant interaction on a regional scale (of the order of 100 km), different OTEC plant scenarios should be analyzed. For example, a comparison of separate and combined plant discharges, or a comparison of the effect of several small plants with the effect of one fewer larger plants with the same nominal power output. For all these cases, the methodology of coupling of near, intermediate, and far fields used in this thesis can be applied.

More modeling must be done to study long-term scenarios under conditions other than the ones studied in this thesis. More research is needed to ensure that this process has no detrimental effect on fish, nutrients, and thermal stratification. This thesis takes a step towards determining whether the thermal energy stored in the ocean can be harnessed as an alternative source of energy.

References

Adams, E. E., Fry, D. J., Coxe, D. H. and Harleman D. R. F. (1979). *Research on the External Fluid Mechanics of Ocean Thermal Power Plants: Report Covering Experiments in Stagnant Water.* Tech. Report 250, R.M. Parsons Laboratory for Water Resources and Hydrodynamics, Massachusetts Institute of Technology, Cambridge, MA.

Adcroft, A., Campin, J.M., Dutkiewicz, S. et al. (2013). *MITgcm User Manual*, Department of Earth and Planetary Sciences, Massachusetts Institute of Technology, Cambridge, MA.

Akar, P.J. and Jirka, G.H. (1995). Buoyant spreading process in pollutant transport and mixing, Part 2: Upstream spreading in weak ambient current. *Journal of Hydraulic Research.* Vol. 33. No 1.

Avery, W., Wu, C. (1994). *Renewable energy from the Ocean- A guide to OTEC.* Oxford University Press, New York, New York.

Briggs, G.A. (1969). *Plume Rise*, US Atomic Energy Commission Critical Review, 81 pp.

Carmichael, A. D., Adams, E. E. and Glucksman, M. A. (1986). *Ocean Energy Technologies: The state of the Art.* EPRI AP-4921, 3-1 to 3-19, Massachusetts Institute of Technology, Cambridge, MA.

Choi, K. W., and Lee, J. H. (2007). Distributed Entrainment Sink Approach for Modeling Mixing and Transport in the Intermediate Field. *Journal of Hydraulic Engineering*, Vol. 133, No. 7, 804-815.

Coxe, D. H. (1980). *An experimental study of OTEC plant operation in a stratified flowing Ocean.* Master Thesis, Massachusetts Institute of Technology, Cambridge, MA.

Coxe, D. H., Fry D. J., and Adams, E. E. (1981). *Research on the External Fluid Mechanics of Ocean Thermal Energy Conversion Plants: Report Covering Experiments in a Current.*

Energy Laboratory and Ralph M. Parsons, Laboratory Report No. MIT-EL 81-049, Massachusetts Institute of Technology Energy Laboratory, Cambridge, MA.

Curtis, H. (2011). Life of the Land's, Energy Independence for Hawaii (2030), An Integrated Approach to Economic Revitalization in a Culturally and Environmentally Sensitive Way. Retrieved from http://www.lifeofthelandhawaii.org/Energy_Independence_for_Hawaii_2030.pdf, January 2013.

Fischer, H. B., List, E. G., Koh, R. C. Y., et al. (1979). *Mixing in Inland and Coastal Waters*. Academic Press, New York, NY.

Fry D. J., and Adams, E. E. (1983). Confined Radial Buoyant Jet. *Journal of Hydraulic Engineering Year*, 109(9), 1185-1202.

Gec Co. Ltd., http://www.otec.ws/otec_principle.html. Retrieved January 2013.

Jirka, G. H. (2004). Integral Model for Turbulent Buoyant Jets in Unbounded Stratified Flows. Part I: Single Round Jet. *Environmental Fluid Mechanics*, 4, 1–56.

Jones, G. R., Nash, J. D., and Jirka, G. H. (1996). *Cormix3: An expert system for mixing zone analysis and prediction of buoyant surface discharges.* DeFrees Hydraulics Laboratory, School of Civil and Environmental Engineering, Cornell University. Ithaca, NY.

Khaligh, A., and Onar, O. C. (2010). *Energy Harvesting: solar, wind and Ocean Conversion Systems,* 305-341. CRC Press, Boca Raton, FL.

Khondaker, A. N. (2000). Modeling the fate of drilling waste in marine environment – an overview. *Computers & Geosciences.* Vol. 26, issue 5, pp. 531-540.

Kobayashi, H., Sadayuki J. and Haruo U. *The present Status and Features of OTEC and Recent Aspects of Thermal Energy.* Proceedings of the 24th UJNR (US/Japan) Marine Facilities Panel Meeting in Hawaii, November 7–8, 2001

Lee, J. H. W., and Chu, V. H. (2003). *Turbulent Jets and Plumes: A Lagrangian Approach.* Kluwer Academic Publishers, Boston, MA.

Legg, S., Hallberg, R. W., Girton, J. B. (2006). Comparison of entrainment in overflows simulated by z-coordinate, isopycnal and non hydrostatic models. *Journal Ocean Modelling,* vol.11, pp. 69-97.

Lockheed Martin, http://www.lockheedmartin.com/us/products/otec.html, Retrieved January 2013.

Ma, T. G., and Quintiere, J. G. (2003). Numerical Simulation of axi-symetric fire plumes: accuracy and limitations. *Fire Safety Journal*, vol. 38, pp. 467-492.

Myers, E. P., Hoss, D. E., Matsumoto, W. M., Peters, D. S., Seki, M. P., Uchida, R. N., Ditmars, J. D., and Paddock, R. A. (1986). *The Potential Impact of Ocean Thermal Energy Conversion (OTEC) on Fisheries.* NOAA Technical Report NMFS 40.

Nihous, G. C. (2007). A Preliminary Assessment of Ocean Thermal Energy Conversion (OTEC) Resources, *Journal of Energy Resources Technology*, 129(1), 10-17.

Nihous, G. C., Brown M. G., Gauthier M., Levrat D. and Ruer J. (2008). Ocean Thermal Energy Conversion (OTEC): Principles, Problems and Prospects, *Proc. 2nd International Conf. on Ocean Energy*, 9 pp., Brest, France.

Nihous, G. C. (2008). *Ocean Thermal Energy Conversion (OTEC) and Derivative Technologies: Status of Development and Prospects.* Hawaii Natural Energy Institute, University of Hawaii, Annual report, 45.

Nihous, G. C. (2010). Mapping available Ocean Thermal Energy Conversion resources around the main Hawaiian Islands with state-of-the-art tools. *Journal of Renewable and Sustainable Energy*. 2(4).

Ocean Energy, by Polacheck L. and Daniels L., http://www.personal.psu.edu/users/l/e/lep5068/Ocean/Welcome.html. Retrieved January 2013.

Ocean Thermal Energy Corporation, http://www.otecorporation.com/news_reader/items/ocean-thermal-energy-corporation-reaches-understanding-toward-building-otec-plants.html?utm_source=theonproject&utm_medium=op-blog&utm_campaign=op-blog-mou-announcement#.UT5B4c1ExQo Retrieved January 2013.

Offshore Infrastructure Associates, Inc., http://www.offinf.com/history.htm. Retrieved January 2013.

Paddock, R. A. and Ditmars, J. D. (1983). *Initial Screening of License applications for ocean thermal energy conversion (OTEC) plants with regard to their interaction with the environment.* Argonne National Laboratory, Springfield, VA.

Pietrzak, J. (1998). The use of TVD Limiters for forward-in-time upstream-biased advection schemes in ocean modeling. Mon. Wea. Rev. 126, 812–830.

Rajagopalan, K. and Nihous, G. C. (2013). Estimates of global Ocean Thermal Energy Conversion (OTEC) resources using an ocean general circulation model. *Renewable Energy*, 50, 532-540.

Roberts, G. O. (1977). *Stratified Turbulence Model for the Near-Field External Flow of an Ocean Thermal. Proceedings: Fourth Annual Conference on Ocean Thermal Energy conversion: OTEC,* pp, IV-7 to IV-25 March 22-24, New Orleans, LA.

SEA 02 Sustainable Development. SEA 02 2004. 20 April 2008.

Sundram, T. R., Sambuco, E., Sinnarwalle, A. M. and Kapur, S. K. (1977). The external flow induced by an ocean thermal energy conversion (OTEC) power plant. *Proceedings of the Fourth Annual Conference on OTEC*, pp. 42-49, New Orleans, LA.

Stolzenbach, K. D. and Harleman D. R. F. (1973). Three-dimensional heated surface jets. *Water Resources Research,* 9(1), 129-137.

Survey Energy Resources*, 2007. World Energy Council.* http://www.worldenergy.org/documents/ser2007_final_online_version_1.pdf. Retrieved January 2013.

Turner, J. S. (1986). Turbulent entrainment: the development of the entrainment assumption, and its application to geophysical flows.*Journal of Fluid Mechanics,* 173, 431-471.

U.S. Department of Energy (1989). *Ocean Thermal Energy Conversion, An Overview*, SERI/SP-220-3024. Retrieved from http://www.nrel.gov/docs/legosti/old/3024.pdf, January 2013.

U.S. Energy Information Administration (2011). *International Energy Outlook 2011*, DOE/EIA 0484. Retrieved from http://www.eia.gov/forecasts/ieo/pdf/0484(2011).pdf, October 2011.

Vega, L. A. (Winter 2002/2003). Ocean Thermal Conversion Premier. *Marine Technology Society Journal,* 6 (4), 25-35.

Vega, L. A. (1992). "Economics of Ocean Thermal Energy Conversion" in *Ocean Energy Recovery: The State of the Art.* New York, New York, American Society of Civil Engineers.

Wang, D. P. (1983). *A Far-Field model of the Regional Influence of Effluent Plumes from Ocean Thermal Energy Conversion (OTEC) plants.* Progress Report, Argonne National Laboratory, ANL/EES-TM-244, 19 p, Springfield, VA.

Wang H. and Law A.W.K. (2002). Second-order integral model for a round buoyant jet. *Journal of Fluid Mechanics,* 459, 397-428.